STRESS ENGINEERING WITH SILICON NITRIDE STRESSORS FOR GE-ON-SI LASERS

by

Jiaxin Ke

B.A., The University of Science and Technology of China, 2015

A THESIS SUBMITTED IN PARTIAL FULFILLMENT OF

THE REQUIREMENTS FOR THE DEGREE OF

MASTER OF APPLIED SCIENCE

in

THE FACULTY OF GRADUATE AND POSTDOCTORAL STUDIES

(Material Engineering)

THE UNIVERSITY OF BRITISH COLUMBIA

(Vancouver)

June 2017

Abstract

Silicon compatible lasers are in great need for applications such as on-chip and short-reach optical interconnects. Although InAs/GaAs quantum dot lasers monolithically grown on Si have been realized and are well-performed, due to material contamination issues, it is time and cost intensive for those III-V materials to enter mainstream Si processing facilities. Germanium(Ge)-on-Silicon(Si) laser is promising as a solution to solve the Si-compatible laser problem as it is compatible with Si processing.

So far, the main problems in Ge lasers are that they have a high threshold current density and low efficiency. Laser structure designs with top and side silicon nitride stressors were proposed in this work and shown to be effective in reducing the threshold current (I_{th}) and improving the wall-plug efficiency (η_{wp}) of Ge-on-Si lasers. Side stressors turned out to be a more efficient way to increase η_{wp} than using the top and side stressors together. With the side stressors and geometry optimizations, a maximum η_{wp} of 34.8% and an I_{th} of 36 mA (J_{th} of 27 kA/cm^2) were achieved with a defect limited carrier lifetime ($\tau_{p,n}$) of 1 ns. With $\tau_{p,n}$ being $10\,ns$, an I_{th} of 4 mA (J_{th} of 3 kA/cm^2) and a η_{wp} of 43.8% were achieved.

These are tremendous improvements from cases without any stressors. Compared to other stress introduction methods, such design is much more suitable for Ge laser structure implementation. These results provide a strong support to the Ge-on-Si laser technology and create an effective way to improve the Ge laser performance.

Lay Summary

Laser is a device that can emit a single color of light and is suitable for communication applications. Germanium (Ge)-on-Silicon (Si) laser is a new type of laser that can be made with low cost and is promising in making our computer run faster and communicate faster with each other. However, the performance of Ge-on-Si lasers has so far been insufficient. To make it perform better, we designed a new structure and optimized it with stress engineering method to investigate the performance potential of Ge-on-Si lasers. Our computational simulations indicate that method is promising to improve Ge lasers' energy efficiency and reduce the current required for lasing.

Preface

The work in this thesis was funded by UBC. All of the work was done in the Department of Materials Engineering at UBC during the past two years, including the structure designs, stress simulation and the laser modeling and optimizations. All the theoretical modeling and simulations were conducted by the author.

In addition, one journal article and one conference paper, and one conference abstract have been published based on the work in Chapter 4 to 5:

Ke, Jiaxin, Lukas Chrostowski, and Guangrui Xia. "Stress engineering with silicon nitride stressors for Ge-on-Si lasers." *IEEE Photonics Journal* 9.2 (2017): 1-15.

J. Ke, G. M. Xia, and L. Chrostowski, "Structure and stress engineering for Ge-on-Si lasers using silicon nitride stressors," 2016 IEEE 13th International Conference on Group IV Photonics (GFP), Shanghai, 2016, pp. 28-29.

J. Ke, Z. Li, S. Li, and G. Xia, "Stress and structure optimizations with side silicon nitride stressors for Ge-on-Si lasers," in Advanced Photonics 2016 (IPR, NOMA, Sensors, Networks, SPPCom, SOF), OSA technical Digest (online) (Optical Society of America, 2016), paper IW1A.5.

A different topic of stress solver developing was done in Lumerical Solutions, Inc., which was not discussed in this thesis.

Table of Contents

Abstract ii

Lay Summary iii

Preface iv

Table of Contents v

List of Tables viii

List of Figures ix

List of Symbols xiii

List of Abbreviations xviii

Acknowledgements xix

Dedication xx

Chapter 1: Introduction 1

1.1 Moore's law and the interconnect bottleneck 1

1.2 Optical interconnects, Si photonics, and Si-compatible lasers 2

1.3 Types of Si-compatible lasers 4

1.4 Structure of this thesis 6

Chapter 2: Literature Review and Problem Definition 8

2.1 Band gap engineering methods 8

2.2 Doping technologies 11

2.3 Stress engineering techniques for Ge 13

2.4 Progress of Ge lasers 16

2.5 Thesis Objective 17

Chapter 3: General Laser Theories 19

3.1 Introduction of Fabry-Perot lasers and rate equation 19

3.2 Threshold condition 22

3.3 Optical loss mechanisms 23

3.4 Loss mechanism for carriers 25

3.4.1 Spontaneous radiative recombination 25

3.4.2 SRH recombination 26

3.4.3 Auger recombination 27

3.5 Gain 30

Chapter 4: Ge Laser Related Modeling and Parameters 33

4.1 Doping-induced Ge band gap changes 33

4.2 Stress effect and models 35

4.3 Effective mass of Γ conduction band 38

4.4 Figures of merits of lasers 41

4.4.1 Threshold current 41

4.4.2 Slope efficiency 41

4.4.3 Maximum wall-plug efficiency 42

4.5 Modeling with LASTIP^{TM} and model calibrations 43

4.6 Modeling of Ge laser with stressors 47

4.7 Limitations of our modeling 55

Chapter 5: Structure and Strain Optimizations 58

5.1 Optimizations of structure 1 without stressors 59

5.2 Optimizations of structure 2 with side stressors only 61

5.2.1 Polysilicon thickness (d_{poly}) optimization 61

5.2.2 Ge Width (W) optimizations 63

5.2.3 Ge thickness d_{Ge} optimization 66

5.2.4 Strain's Impact 69

5.3 Optimizations of structure 3 with top and side stressors 73

5.4 Comparisons of the structures 75

5.5 Effect of defect-limited minority carrier lifetime on the performance 78

Chapter 6: Thesis Summary and Suggestions for Future Work 81

Bibliography 83

List of Tables

Table 3-1 Threshold energy for different Auger recombinations. Table courtesy of Rodolfo E. Camacho-Aguilera at MIT [30]. 30

Table 4-1 Material parameters used in the modeling of Ge laser [26] 46

Table 4-2 Laser performances of the three structures in Figure 4-11. 55

Table 5-1 Laser performance of the 3 structures in Figure 5-16 after structure optimizations. ... 76

Table 5-2 Laser performance of the three structures in Figure 5-20. 80

List of Figures

Figure 1-1 RC delay time of metal wire and intrinsic gate delay vs. technology node [4]. 2

Figure 1-2 Key devices in silicon photonics [9]. 4

Figure 2-1 Band structures of Ge under different conditions. (a) bulk Ge without strain or doping; (b) tensile strained Ge without doping; (c) highly n-type doped Ge without strain. Figure courtesy of Donguk Nam at Stanford University [29]. 9

Figure 2-2 Calculation and experimental result of band crossing of GeSn alloy as a function of Sn concentration. Figure courtesy of Huo Yijie at Stanford University [3]. 11

Figure 2-3 Top SiN on Ge stripes for strain introduction [41]. Figure reproduced with the permission from Optical Society of America. 15

Figure 2-4 Suspended Ge microbridges with high tensile strain [44]. Figure reproduced with the permission from OSA Photonics Research. 16

Figure 2-5 Prototype of the electrically pumped Ge-on-Si laser device [23]. Figure reproduced with the permission from Optical Society of America. 17

Figure 3-1 Band diagram of a forward biased double-heterostructure laser diode [46]. 19

Figure 3-2 Diagram of CCCH (a) direct and (b) indirect Auger recombination. Figure courtesy of Rodolfo E. Camacho-Aguilera at MIT [30]. 28

Figure 3-3 Radiative carrier lifetime of n-type and p-type dopants in Ge. Figure courtesy of Rodolfo E. Camacho-Aguilera at MIT [59] [30]. 29

Figure 4-1 n-type band gap narrowing effect of different models at 300 K. 35

Figure 4-2 Direct and indirect band gap energies under different biaxial strain. 37

Figure 4-3 LASTIP^{TM}'s results of material gain at different m_{Γ}^{*} with 0.25% biaxial strain carrier concentration $n=p=4\times10^{19}cm^{-3}$. 39

Figure 4-4 Ge profiles measured by SIMS. The Ge profiles are shifted laterally for easy comparison. UGUS: undoped-Ge/undoped-Si; UGPS: undoped-Ge/ Phosphorus-doped-Si; PGUS: Phosphorus-doped-Ge/undoped- Si; PGPS: Phosphorus-doped-Ge/Phosphorus-doped-Si. The black dash line is the Ge profile of sample PGPS before annealing. Figure courtesy of Feiyang Cai at UBC [74]. 40

Figure 4-5 Cross-section of the Ge-on-Si heterojunction laser structure simulated. 47

Figure 4-6 L-I curves for the experimental result, calibration result, and sensitivity tests with a smaller FCA loss: $\alpha^i = 5.0 \times 10^{-19}\mathrm{N} + 0.923 \times 10^{-17}\mathrm{P}$, and a smaller effective mass $m_{eГ}$* = 0.0453 m_e. 47

Figure 4-7 Laser structure simulated (cavity width = 1 μm, thickness = 0.2 μm, length = 270 μm, cladding thickness = 0.18 μm). (a) Structure 2: with side nitride stressors; (b) Structure 3: with top & side nitride stressors. The width of the top nitride stressor is the same as that of the Ge cavity. The metal contacts are composed of Ti and Al same as those in Ref. [23], shown in Figure 4-6.48

Figure 4-8 Normalized light intensity of 1D cut in the centre line of (a) structure 2 (structure 1 have a similar distribution); (b) structure 3. 2D profile of (c) structure 1; (d) structure 2; (e) structure 3. 49

Figure 4-9 2D Strain map on the cross section: (a) ε_{eb} (b) ε_{zz} of structure 2 with side stressors only （cavity width = 1 μm, thickness = 0.2 μm, cladding thickness = 0.18 μm). 51

Figure 4-10 2D Strain map on the cross section: (a) ε_{eb} (b) ε_{zz} of structure 3 with side and top stressors (cavity width = 1 μm, thickness = 0.2 μm, cladding thickness = 0.18 μm). 52

Figure 4-11 L-I curve comparison for the three structures before the structure optimizations. ... 54

Figure 5-1 I_{th} and η_{wp} of Structure 1, d_{poly} dependence. 59

Figure 5-2 I_{th} and η_{wp} of Structure 1 (a) width dependence; (b) d_{Ge} dependence. 60

Figure 5-3 Polysilicon thickness d_{poly} dependence (W =1 μm, d_{Ge} = 0.2 μm) of (a) $<\alpha_i>$ and η_{ext} ,η_d (b) I_{th} and η_{wp}. 62

Figure 5-4 Ge width W dependence (d_{poly} =0.8 μm, d_{Ge} = 0.2 μm) of (a) strain ε_{eb} and Γ (b) $<\alpha_i>$ and Γ. 63

Figure 5-5 Ge width W dependence (d_{poly} =0.8 μm, d_{Ge} = 0.2 μm) of (a) η_d and η_{ext} (b) I_{th} and η_{wp}. 64

Figure 5-6 Impacts of Ge width (W) on other parameters. 65

Figure 5-7 Ge thickness d_{Ge} dependence (W =0.5 μm, d_{poly} = 0.8 μm) of I_{th} and η_{wp}. 66

Figure 5-8 Ge thickness d_{Ge} dependence (W =0.5 μm, d_{poly} = 0.8 μm) of (a) Strain ε_{eb} and Γ (b) $<\alpha_i>$ and Γ. 67

Figure 5-9 Ge thickness d_{Ge} dependence (W =0.5 μm, d_{poly} = 0.8 μm) of η_d and η_{ext}. 68

Figure 5-10 Impacts of Ge thickness d_{Ge} on other parameters. 68

Figure 5-11 (a) Strain ε_{eb} and λ with different d_{Ge} (W=0.5μm, d_{poly} = 0.8μm): (b) direct band alignment under different strain at thermal equilibrium (V=0, d_{Ge}=0.8 μm)..... 70

Figure 5-12 Strain impact with different d_{Ge} (W=0.5μm, d_{poly} = 0.8μm): (a) material gain at different strain with carrier concentration $n=p=4\times10^{19}cm^{-3}$, (b) I_{th}, and (f) η_d..... 71

Figure 5-13 Strain impact with different d_{Ge} (W=0.5μm, d_{poly} = 0.8μm): (a) η_{ext} (b) η_d. 72

Figure 5-14 I_{th} and η_{wp} of Structure 3 (a) width dependence (b) d_{Ge} dependence. 74

Figure 5-15 I_{th} and η_{wp} of Structure 3, d_{poly} dependence..... 75

Figure 5-16 L-I curve for three structures after optimization. 76

Figure 5-17 Current density field of structure 2 (a) in x direcdtion; (b) in y direction at 60 mA inject level. 77

Figure 5-18 Current density field of structure 3 (a) in x direcdtion; (b) in y direction at 60 mA inject level. 77

Figure 5-19 Defect limited carrier lifetime dependence of I_{th} and η_{wp}. 79

Figure 5-20 . L-I curve for three structures with $\tau_{p,n} = 10$ ns..... 80

List of Symbols

A	Free electron absorption coefficient.
a_Γ, a_L	Hydrostatic deformation potential at Γ and L valleys.
a_{eff}	Effective hydrostatic deformation potential.
B	Free hole absorption coefficient.
B_{21}, B_{12}	Einstein coefficients for stimulated emission and absorption.
b	Shear (uniaxial) deformation potential.
b_{eff}	Effective shear (uniaxial) deformation potential.
C_{11}, C_{12}	Elastic constants.
C_n, C_p	Electron and hole Auger recombination coefficient.
c_{nj}, c_{pj}	Electron and hole capture coefficients of the j^{th} deep trap.
d	Thickness of laser cavity.
d_{Ge}	Thickness of Ge.
d_{Poly}	Thickness of polysilicon.
E_{fc}, E_{fv}	Quasi-Fermi level of electrons in the conduction and valence band.
E_c, E_v	Energy levels in the conduction and valence band that associated with the photon transition and $E_c - E_v = \hbar\omega$.
E_g	Band gap energy.
E_{os}	Stored optical energy in the cavity.
$E_{\Gamma\text{-}hh}$, $E_{\Gamma\text{-}lh}$	Direct band gap energies between the Γ valley and the heavy hole, light hole valence band.
$E_{L\text{-}hh}$, $E_{L\text{-}lh}$	Indirect band gap energies between L valley and the heavy hole, light hole valence band.

$E_{C\text{-}hh}$, $E_{C\text{-}lh}$	Band gap energies between conduction band and the heavy hole, light hole valence band.
ΔE_g^L	Indirect band gap narrowing effect.
$\delta E_{hy}, \delta E_{sh}$	Hydrostatic and shear deformation energy.
f_{tj}	Occupancy possibility of the j^{th} deep trap level.
f_c, f_v	Electron's occupation probability in the conduction band and valence band.
G_{gen}	Electrons genertaion rate.
g	Material gain.
g_{th}	Threshold optical gain.
$h, \hbar$	Planck constant and reduced Planck constant.
I	Injection current.
I_{th}	Threshold current.
I_{op}	Operation current.
J_{th}	Threshold current density.
K	Wave vector.
k	Boltzmann constant.
L	Length of Ge cavity.
m_n, m_p	Bulk effective masses for electrons and holes.
m_r^*	Reduced effective mass.
m_c^*, m_v^*	Effective mass of direct conduction and valence band.
m_e	Free electron mass.
N	Electron density.
N_{th}	Threshold carrier concentration.

N_{tj}	Density of the j^{th} deep trap.
N_{1j}	Electron concentration when the electron quasi-Fermi level coincides with the energy level.
N_i	Intrinsic carrier density without doping.
N_D	n-type dopants' concentration.
n	Refractive index.
P	Hole density.
P_{1j}	Hole concentration when the electron quasi-Fermi level coincides with the energy level E_{tj} of the j^{th} trap.
P_{th}	Threshold hole density of hole.
P_{out}	The optical power output.
P_{elect}, P_{opt}	Electric and optical power.
$\|p_{cv}\|$	Transition matrix factor.
Q_ε	Shear deformation energy.
q	Electron charge.
R_{rec}	Electron recomination rate.
R_{sp}	Spontaneous recombination rate.
R_{SRH}	SRH absorption rate.
R_{Aug}	Auger recombination rate.
R_{st}	Stimulated emission rate.
Rec	Carrier desity ralated recombination.
R_1, R_2	Reflectivity of two end facets.
R_{21}	Stimulated emission rate from energy level 2 to 1.

R_{12}	Stimulated absorption of photons from energy level 1 to 2.
R_n^{tj}, R_p^{tj}	Electron and hole recombination rates through j^{th} deep trap level. E_{tj} of the j^{th} trap.
R	Series resistance.
S	Photon densitiy.
T	Temperature.
Vol, Vol_p	Active region volume for carriers and photons.
V_{op}	The operation voltage.
V_D	Diode voltage.
v_g	Group velocity.
W	Width of Ge cavity.
α_i, α_m	Internal loss and mirror loss coefficient.
$<\alpha_i>$	Weighted average of the internal loss.
β	Ratio of vertical strain and effective biaxial strain which is defined as $\beta=\varepsilon_{zz}/\varepsilon_{eb.}$
Δ	Spin-orbit splitting energy.
ε_{xx}, ε_{yy}, ε_{zz}	Strain in horizental, length and vertical direction.
ε_b, ε_{eb}	Biaxial strain and effective biaxial strain.
Γ	Confinement factor.
η_i, $\eta_{d,}$ η_{ext}	Internal efficiency, slope efficiency and extraction efficiency.
η_{wp},	Wall-plug efficiency.
λ	Light wavelength.
σ_{nj}, σ_{pj}	Electron and hole capture cross sections of the j^{th} deep trap.
ρ_r	Joint density of states of direct conduction band.
τ_{nj}, τ_{pj}	Electron and hole lifetime due to the j^{th} trap.

τ_{pho}	Photon lifetime.
$\tau_{p,n}$	Defect limited carrier lifetime for hole and electron.
$\bar{\upsilon}_n, \bar{\upsilon}_p$	Average thermal velocity of electrons and holes.
ω	Angular frequency.

List of Abbreviations

CMOS	Complementary metal-oxide-semiconductor filed effect transistor.
CMP	Chemical mechanical polishing.
ELOG	Epitaxial lateral overgrowth.
FCA	Free carrier absorption
fab	Fabrication facility.
GOI	Germanium on insulator.
IC	Integrated circuit.
MOSFET	Metal-oxide-field-effect transistor.
QW	Quantum well.
QD	Quantum dot.
RC	Resistance-capacitance.
SOI	Silicon on insulator.
SHR	Shockley-Read-Hall
TD	Threading dislocation.
TCAD	technology computer aided design
0D,1D,2D	Zero, one, and two-dimensional.

Acknowledgements

Firstly, I would like to express my sincere gratitude to my research supervisor Prof. Xia for the continuous support of my master study and related research. Her guidance has helped me in all the phases of research and writing of this thesis. I could not imagine having a better supervisor and mentor for my master study.

I would also like to thank Crosslight Software Inc. for supporting the work in this thesis.

I wish to express my sincere thanks to UBC Materials Engineering for providing me with all the necessary facilities for the research.

I appreciate the help from my friends and colleagues at UBC. Special thanks are given to Weijun Luo and Yiheng Lin, who taught me the operation of Raman measurements and X-ray diffraction and gave me useful suggestions on my project. Feiyang Cai, Guangnan Zhou and Yunlong Zhao were my group mates, and we had many interesting discussions during group meetings that greatly broadened my knowledge in microelectronics and photonics.

And finally, I wish to express my gratitude to my parents for their ever-lasting love and support, without which I cannot be here. I always owe them for their unconditional love.

Dedication

To my father and my mother.

Chapter 1: Introduction

1.1 Moore's law and the interconnect bottleneck

Silicon (Si)-based microelectronics has been the engine of modern information technology for the last five decades. From the observation of Gordon Moore, the number of transistors on an integrated circuit (IC) doubles every two years because of the scaling down of gate length, junction depth, and gate dielectric thickness of metal-oxide-field-effect transistors (MOSFETs). This is known as Moore's law [1]. As a result, the performance of electronic devices improved dramatically in the past decades.

However, such scaling has reached its physical limitation in recent years. From 2004 to 2010, the scaling factor of gate length is 0.9 per year [2], which is larger than the predicted scaling factor of 0.7 [1]. At the same time, the scaling down of the transistors does not always bring benefit. Observed from Figure 1-1, with the scaling of transistors, the delay of metal interconnect increases dramatically, but the intrinsic gate delay does not decrease that much. As a result, the RC delay caused by the metal interconnects becomes the bottleneck of computation speed and is known as the interconnect bottleneck. Although many new materials like low-K dielectric materials and new architectures have been applied to reduce the RC delay [3], they are not going to solve the problem in the long run. Moreover, the high power consumption caused by the metal interconnects is the main source of IC heating problems. The solution to these problems is to use optical interconnects to replace metal interconnect, especially for long distance communication.

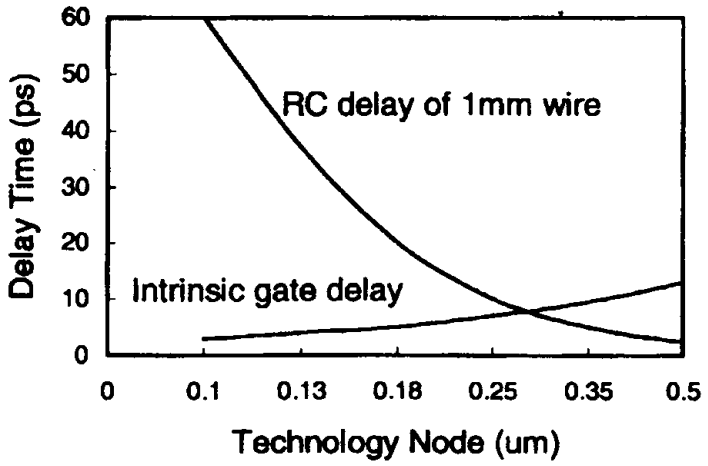

Figure 1-1 RC delay time of metal wire and intrinsic gate delay vs. technology node [4].

1.2 Optical interconnects, Si photonics, and Si-compatible lasers

Optical interconnects have been used in communications for decades especially in the long distance communication using optical fibers. There are several advantages of optical interconnects compared to metal interconnects. The first advantage lies in the low power consumption of optical interconnects. The main reason for the low power consumption is the zero rest energy of photons. As a result, it requires less energy to transmit photons [3]. Also, the attenuation of signals in the optical fibers is significantly lower than metal interconnects in long distance. The second advantage is the high speed and bandwidth. Since photons are immune to RC delay, the computation speed is not limited by the communication speed. Because photons at different wavelengths do not interact with each other, the wavelength-division multiplexing (WDM) technology can be applied in the multi-channel communication. Light signals at different wavelength can be transmitted simultaneously and thus increase bandwidth. Thirdly, the cost of silica fiber is lower than metal wire [3, 5].

With the successful application of optical interconnects in long distance, optical interconnects were gradually applied to a shorter distance like the rack-to-rack (1-100 m), board-to-board (0.5-1 m), chip-to-chip level (1-50 cm) or on-chip (< 1 cm) levels. Short-reach optical communications (< 100 m) are widely used in data centres and supercomputers. For short-reach optical interconnects, more and more Si photonic technologies have been used. An example is Intel's optical Thunderbolt^{TM} cables that allow the optical connection of external peripherals to a computer [6-8].

Si photonics is an emerging technology to leverage the silicon CMOS fabrication technology for the creation of photonic devices. It has been identified as a path toward addressing the challenges of increasing functionality and bandwidth requirement of cloud computing and data centres. The low cost and high performance of integrated photonics circuits may meet the need of the continuing expansion of the internet infrastructures with higher and higher performance requirement. Figure 1-2 shows the main photonic devices in Si photonics. Si photonic systems require light sources, modulators, waveguides, and photodetectors. A modulator transfers the electric signals into optical signals, then the optical signals transmit through a waveguide and are captured by the photodetector and then be transferred back to electric signals. These devices are often connected to Si-based electronic circuits such as laser driver circuits and photodetector amplification circuits. All components, except for the light source, have been developed on a Si platform with high bandwidth capacity.

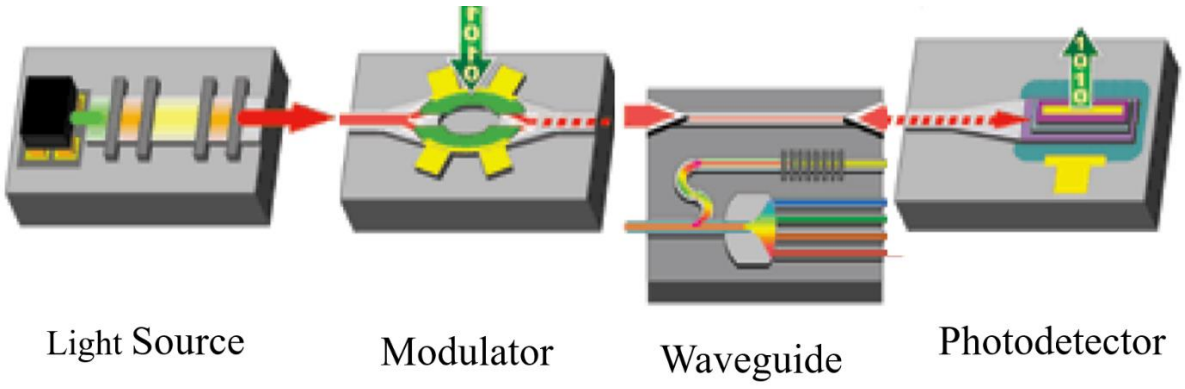

Figure 1-2 Key devices in silicon photonics [9].

There are two ways to implement the light source: one is to use external laser source and the other is to build an on-chip laser source. Although external laser sources with high emitting efficiency and good temperature stability can be used, they often suffer from problems like large coupling losses, design complexity, large footprint and high packaging expense [10]. In comparison, the on-chip laser sources have bigger potential to reach a higher integration density, better energy efficiency and better energy proportionality than external laser sources [10]. However, the development of on-chip laser sources has met great challenges. Due to the indirect band gap nature of Si, the Si-based laser sources have poor performance. Integrating traditional light emitting III-V semiconductors like GaAs or InP also encounter material compatibility issues like significant big mismatch in lattice constants and thermal expansion coefficients [11, 12]. Approaches to address these issues are discussed in Section 1.3.

1.3 Types of Si-compatible lasers

In the past few decades, researchers all over the world have invested extensive efforts in finding solutions to a Si-compatible laser system. Now, several approaches have been proposed. Silicon based lasers like Si Raman laser [13], porous Si laser [14], Si nanocrystals [15] and Er-doped silicon laser [16-19] suffer from problems like intrinsic optical pumping mechanism, low optical

gain or limitation of Er concentration etc., which prevent these lasers from useful applications as efficient light source [10].

Integrating III-V materials, e.g. GaAs and InP, with Si platform has attracted much attention. Three main integration approaches have been extensively explored: direct mounting integration, wafer bonding based heterogeneous integration and direct hetero-epitaxial growth [10]. The direct mounting approach integrates a laser diode die with a Si on insulator (SOI) wafer directly with solder bumps. This method retains the superior characteristic of III-V laser diodes but suffers from inefficient end coupling and poor alignment precision. A sub-micron precision is required, and the facet reflection causes troubles to the whole system [10]. As a result, direct mounting can only be used as a temporary solution to the integration problem. The second integration method is through wafer bonding. III-V material is vertically coupled to silicon chips by wafer bonding. This approach is not subject to lattice mismatch and can be aligned with high precision. However, the wafer bonding method has disadvantages of high cost, low yield, and low integration density, and suffers from the wafer size mismatch [10]. The final integration method is the direct hetero-epitaxial growth of III-V materials on Si. Resulting from the large lattice constant and thermal expansion coefficient mismatch between Si and III-V materials, high density of threading dislocations (TD) occurs during the growth, which fails the optical devices. TD reducing technologies such as epitaxial lateral overgrowth (ELOG) along with a thick buffer layer are required to lower the TD density. Quantum wells (QWs) have been successfully grown on the ELOG InP layers with good optical properties [20]. Another way to overcome the problems caused by TD is to use nanostructures like quantum dots (QDs). The discrete distribution of QDs improves the defect tolerance. The direct hetero-epitaxial growth of InAs/GaAs QDs on Si has been realized

in recent years [21]. However, due to contamination issues, there is still a long way for III-V semiconductors to be adopted in the mainstream Si fabrication facilities (fabs).

Until now, companies have put lots of efforts in integrating III-V lasers on silicon and great progress has been achieved. In 2016, Intel release the first commercial 100 Gbps optical transceiver that integrate III-V lasers on silicon chip by wafer bonding. A start up company Skorpios also achieved their CMOS tunable laser in a similar way. Another company Luxtera also achieved their 100 Gbps optical transceiver by direct mounting integration.

Ge-on-Si lasers are another competitive solution because they are fully compatible with the complementary metal-oxide-semiconductor field effect transistor (CMOS) technology, which will greatly reduce the process complexity, cost, and time to enter the fabs [10]. Optically pumped Ge laser was first realized in 2010 [22] and electrically pumped Ge lasers were demonstrated in 2012 [23] and 2015 [24] accordingly. However, the Ge lasers achieved have large threshold current and very low efficiencies. Debugging the poor performance and providing predictions of Ge laser potential are in great need. Although there are theoretical studies or calculations on Ge lasers, most of them are over simplified zero-dimensional (0D) or one-dimensional (1D) calculations and are not based on experimental data [25]. Experimental-data-based two-dimensional (2D) modeling and simulations were discussed only in one study with a fixed strain level [26]. As a result, it is important to come up with a new design and modeling to address the problem of low efficiency of Ge laser.

1.4 Structure of this thesis

In this work, we proposed new designs to improve the efficiency and lower the threshold current of Ge laser. 2D laser modeling was performed and calibrated with experimental results. Optimizations of Ge lasers were conducted to maximize the laser performance.

The thesis is organized as below:

In Chapter 2, we will review the progress and techniques in Ge lasers and define the problem.

In Chapter 3, we will introduce a general laser theory to better understand how Ge lasers are modeled.

In Chapter 4, we will discuss the Ge laser modeling, strain introduction and strain calculation.

In Chapter 5, we will discuss the optimization results of Ge lasers and propose ways to improve Ge laser performance.

Chapter 2: Literature Review and Problem Definition

2.1 Band gap engineering methods

Ge and Si are both Group IV semiconductors, and Ge is the most Si-compatible semiconductor. They have the same crystalline structure (diamond cubic structure), a similar lattice constant and physical properties such as self-diffusivity, Young's modulus, and Poisson ratio. Due to Ge's unique optical properties and compatibility with Si, it plays an important role in the light sensing and modulation in the silicon photonics [27, 28]. However, Ge is an indirect band gap semiconductor as Si, which is inferior in light emitting applications than direct band gap semiconductors, such as Gallium Arsenide (GaAs) and Indium Phosphide (InP). Figure 2-1 (a) illustrates the band structure of Ge [29]. The band structure of Ge is called indirect band gap because the minimum energy state of the conduction band does not align with the maximum energy state of the valence band in K (wave vector) space. When an electron in L valley wants to recombine with a hole in the valence band, a third particle, normally a phonon, is needed to maintain the conservation of momentum because photons carry 0 crystal momentum. The involvement of phonons makes this process much less likely to occur, which makes the indirect band gap transitions in Ge 4 to 5 orders of magnitude less effective than that of direct band gap transmissions [30].

Fortunately, the direct band gap at the Γ valley is only 136 meV higher than the indirect band gap at the L valley at room temperature. Therefore, by band gap engineering, it is possible to modify the band structure of Ge and turn Ge into a direct or pseudo-direct band gap material for efficient light emitting. Three methods have been proposed to modify the band structure of Ge.

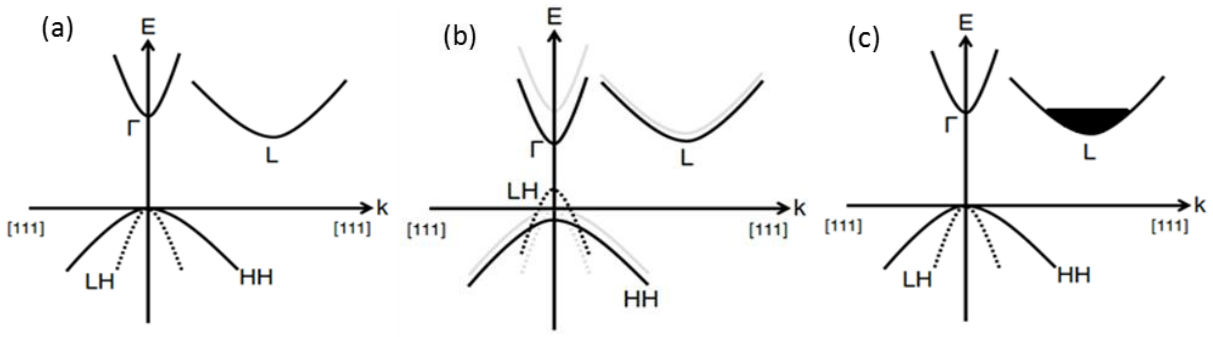

Figure 2-1 Band structures of Ge under different conditions. (a) bulk Ge without strain or doping; (b) tensile strained Ge without doping; (c) highly n-type doped Ge without strain. Figure courtesy of Donguk Nam at Stanford University [29].

The first method to engineer the band structure of Ge is by introducing tensile strain. In 1996, Fischetti and Laux from IBM first presented the theoretical work that under 1.75% biaxial strain, Ge turned into a direct band gap material [31]. As shown in Figure 2-1 (b), with tensile strain, the conduction band edge is lowered, and the valence band is lifted up. The Γ valley (direct) of conduction band approaches the light hole (lh) band top faster than the L valley (indirect), and under more than 1.75% biaxial or 4.6% uniaxial tensile strain, Ge becomes a direct band gap material [29]. It has been demonstrated that introducing small strain in Ge layer is beneficial for Ge-based optoelectronic devices like detectors and modulators. Moreover, tensile strains cause a light hole (lh) and heavy hole (hh) band splitting, which reduces the density of states near the band edge and provides an extra benefit of achieving a low threshold laser [10]. However, high strains also cause a redshift in the lasing wavelength from the technologically important 1550 nm wavelength range to longer wavelengths [10]. The redshift may be a problem for optical fiber communication since the 1550 nm L-band was selected according to the low loss windows of optical fibers. For on-chip interconnects, there are no such concerns. Due to the difficulties of introducing high-level tensile strains and constructing laser structures at the same time, no Ge

lasers have been built solely by strain engineering yet. Methods of obtaining high tensile strain will be discussed in Section 2.3.

The second method, n-type doping (usually with phosphorus), is used to help achieve pseudo-direct band gap Ge. The difference between direct band gap and the pseudo-direct band gap is that the latter still has an indirect band gap structure, but the indirect band gap is filled up by doping to an energy level that is equal to the energy level of the lowest energy level of the direct band. Therefore, extra electrons in the indirect band have higher possibility to jump into the direct band via intervalley scattering process [5]. Electrons in both bands can participate in recombinations, but the efficiency of recombinations from the direct band is much higher than that of the indirect band. In terms of recombination, the indirect band electron contribution can be safely ignored. However, the indirect band still has energy states that are in the same energy range as the direct band energy states as seen in Figure 2-1 (c). As a result, electrons still need to fill the energy states in the indirect band (L valley) and the electrons going to the direct band (Γ valley) are reduced. Although the pseudo-direct band gap is not ideal, it was shown to enhance the optical gain in Ge significantly, which made Ge lasers possible [32]. However, high doping also introduced a high free carrier absorption, and as a result, increased the threshold current greatly [5].

Tensile strain and high n-type doping are usually used together to achieve a pseudo-direct band gap condition. According to calculation results, an n-type doping concentration in the order of 10^{19} cm^{-3} with a 0.25% biaxial tensile strain can turn Ge into a pseudo-direct band gap material [32]. The first electrically pumped Ge laser was achieved by this method.

The third method to modify the band structure of Ge is to grow a GeSn alloy. It was predicted theoretically that when Sn reached a certain concentration, GeSn alloy became a direct band gap material [33]. However, such concentration is not well studied, and in different theoretical models,

the value varies from 6% to 20% [3]. The key in achieving direct band gap by GeSn alloying is to achieve high-quality GeSn alloy with sufficient Sn concentration. The main challenge is the low solubility of Sn in Ge (<1%), which is far away from the required concentration [10]. As a result, problems like Sn precipitation, amorphization occur. Despite these difficulties, high-quality GeSn alloy with Sn concentration of 12.6% was achieved using chemical vapor deposition (CVD), and lasing was observed [34]. However, the GeSn laser demonstrated were optically pumped instead of electronically pumped with a lasing wavelength of 2.3 μm, and could only operate below 90 K [34]. GeSn is an interesting material for future CMOS compatible mid-infrared laser applications, but more researches are still needed.

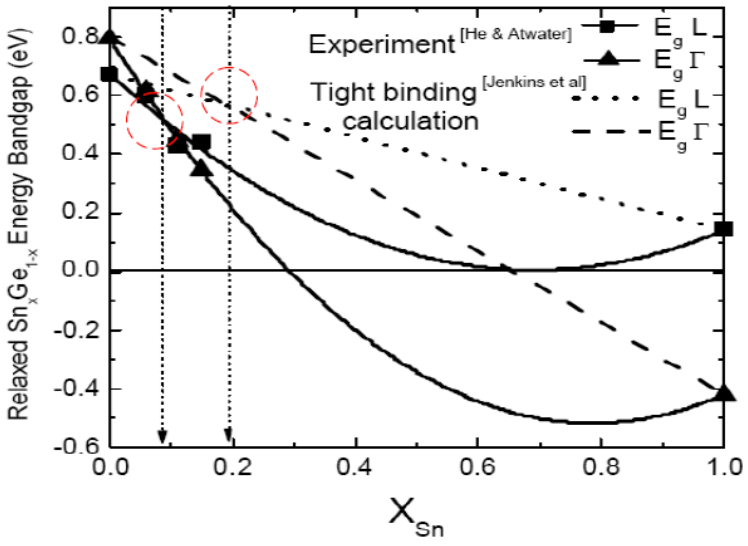

Figure 2-2 Calculation and experimental result of band crossing of GeSn alloy as a function of Sn concentration. Figure courtesy of Huo Yijie at Stanford University [3].

2.2 Doping technologies

A high doping in Ge is required in achieving pseudo-direct band gap structure. Ion implantation is the most common method to introduce dopants in semiconductors. By applying a high electric

field, ions are accelerated to obtain a high energy before shooting into the host semiconductors. The advantages of doping by ion implantation is its precision in controlling doping doses and its low processing temperature.

Although high n-type doping concentrations can be obtained by ion implantation, the implant damages, such as vacancy aggregation and material amorphization caused by the heavy ion collisions, are difficult to be resolved. These defects will become non-radiative recombination centres for carriers and reduce the direct band gap transition efficiency of the material. The results of the Kimerling's group showed that the photoluminescence intensities of the Ge samples doped with ion implantation were 5 times lower than those of Ge samples doped with in-situ methods [5]. Photoluminescence is an important measurement of the direct band gap transmission efficiency. In theory, n-type doping can fill the L-level, which helps to achieve direct band gap transitions in pseudo-direct or indirect band gap semiconductors to enhance photoluminescence intensity. However, ion implantation also results in greater implant damage, which can counteract the effect of n-type doping [36]. As a result, Kimerling's group and others research groups have argued that ion implantation may not be a good choice for n-type doping of Ge due to the fact that the damage caused by implantation is difficult to be completely removed.

In order to avoid implantation defects in materials, a variety of in-situ doping methods have attracted the attention of researchers. If gaseous phosphorus is used as the dopant source, and Reduced Pressure Chemical Vapor Deposition (RPCVD) and Ultra-High Vacuum Chemical Vapor Deposition (UHVCVD) are used for the doping, the maximum n-type doping concentration achievable is 1×19 cm^{-3} [37]. The reason why the doping concentration cannot increase lies under the contradiction between the phosphorus out-diffusion and low temperature requirement for high-quality materials growth [5]. To solve this problem, the Kimerling's group proposed multi-layer

delta-doping method [38]. Several mono-layers of phosphorus on Ge (delta layers) were grown on top of the active region as the dopant source. The dopants then diffused into Ge by a drive-in annealing. Using such multiple stacked germanium-phosphorus layers as a dopant source on a 600 - 800 nm thick Ge film, a uniform n-type doping concentration of 4.0×10^{19} cm^{-3} was reached, which is the highest doping level achieved using a CVD method [38].

Doping concentration currently used in Ge laser is quite high and almost reaching the solubility limit of dopants. Further increase in the n-doping concentration will meet difficulties in controlling the dopant out-diffusion and growing high-quality Ge films simultaneously [10]. Among the three band gap engineering methods discussed in Section 2.1, introducing tensile strain is a more promising solution to improve the efficiency of Ge laser.

2.3 Stress engineering techniques for Ge

As discussed, n-type doping is a double-bladed sword. It helps the band gap engineering, but at the same time increases the optical loss greatly. Stress engineering does not introduce the high optical loss. Several CMOS compatible methods have been applied to introduce strain in Ge. Thermal annealing is the most common and convenient strategy to do so. When Ge cools down from the growth temperature, typically 750 °C, the thermal expansion coefficient mismatch between Ge and Si causes Ge to shrink more than Si and thus results in a tensile strain in Ge. However, the tensile strain introduced by this method is limited to 0.20% because of the strain relaxation above 750°C [39]. By using backside silicidation of C54-$TiSi_2$, which is a relatively simple method, the tensile strain in the front side Ge epitaxial layer has been increased from 0.20% of the 800 °C as-grown sample to about 0.24% [39]. Other CMOS compatible approaches to achieve high strain levels in Ge include strain transfer from other intrinsic stressors and micromechanical engineering technology.

A common stress-introducting material in CMOS industry is silicon nitride (SiN). The stress level in SiN can be easily tuned to either compressive or tensile stress by changing the deposition conditions. The built-in stress in SiN has a wide range from -2 to +2 GPa [40]. When SiN is used as a compressive stressor, it releases stress by expanding and forcing the materials in contact to expand whereas a tensile stressor tends to cause a contraction in the adjacent areas. Therefore, In order to introduce a tensile strain, a compressive SiN stressor should be used as a top stressor to stretch the Ge layer, and a tensile SiN stressor should be used as a side stressor to pull the Ge layer from both sides. However, introducing strain merely using SiN is limited because of the low transfer efficiency resulting from the large thickness of the substrate [10]. Some micromechanical engineering methods are usually adopted. Capellini et al. used “I” and “H” shape structure and used silicon nitride layer as a top stressor to reach about 0.7% effective biaxial strain in Ge as shown in Figure 2-3 [41]. Jinendra et al. used SiN with intrinsic tensile stress of 1 GPa as the side stressors and etch away the buried oxide layer below the Ge layer to form a suspended platform and achieved 0.99% uniaxial strain and 0.82% biaxial strain experimentally [42].

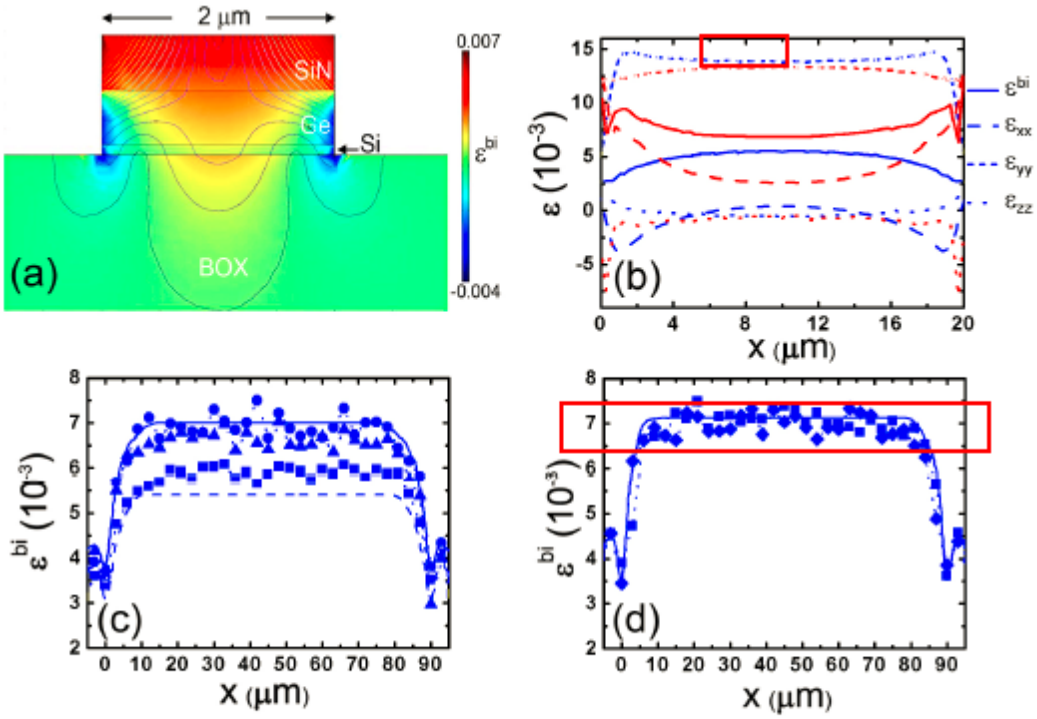

Figure 2-3 Top SiN on Ge stripes for strain introduction [41]. Figure reproduced with the permission from Optical Society of America.

Ge microbridges like those in Figure 2-4 were designed to obtain high tensile stain by reducing the contacting area and enhancing the strain transfer efficiency [10]. By etching the oxide below, Ge microbridges were suspended and pulled to reach a 3.1% uniaxial tensile strain [43]. By transforming the epitaxially grown Ge onto oxide through wafer bounding and then etching away the oxide, the uniaxial strain in the Ge microbridge was further increased to 5.7% and a direct band gap Ge was experimentally achieved [44].

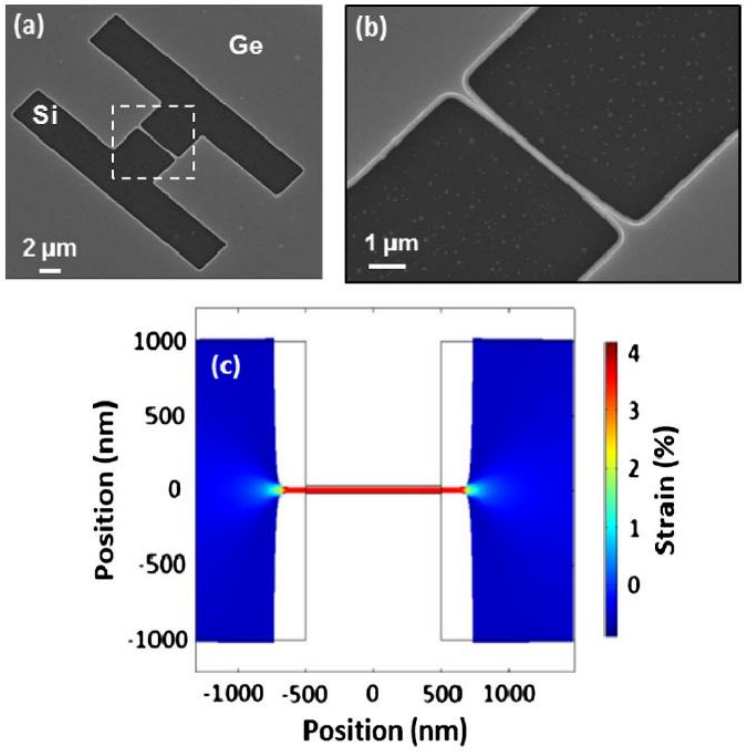

Figure 2-4 Suspended Ge microbridges with high tensile strain [44]. Figure reproduced with the permission from OSA Photonics Research.

2.4 Progress of Ge lasers

In 2007, Liu et al. from Prof. Kimerling's group at MIT proposed that Ge can become a pseudo-direct band gap material by adding tensile strain and doping [32]. In 2010, they successfully fabricated a tensile-strained, n-type doped optically pumped Fabry-Perot Ge laser, which was the first Ge laser in the world [22]. A 0.25% biaxial tensile strain resulted from the thermal expansion mismatch between Si and Ge was achieved, and the doping concentration was about 1.3×10^{19} to 2.5×10^{19} cm^{-3}. When the injected carrier concentration reached 5.0×10^{19} cm^{-3}, an optical gain of more than 60 cm^{-1} was observed, and the lasing wavelengths were between 1590 to 1610 nm.

In 2012, Camacho-Aguilera et al. demonstrated the first electrically pumped Ge-on-Si laser with 4×10^{19} cm^{-3} n-type doped Ge and 0.25% biaxial tensile strain, as shown in Figure 2-5. The lasing wavelengths were between 1520 nm and 1700 nm depending on the cavity thickness. A high

optical gain of over 400 cm^{-1} was observed in electrically pumped lasers to overcome the high loss resulted from the metal contacts and free carrier absorption in Ge and polysilicon. The threshold current density was 280 kA/cm^2 [23].

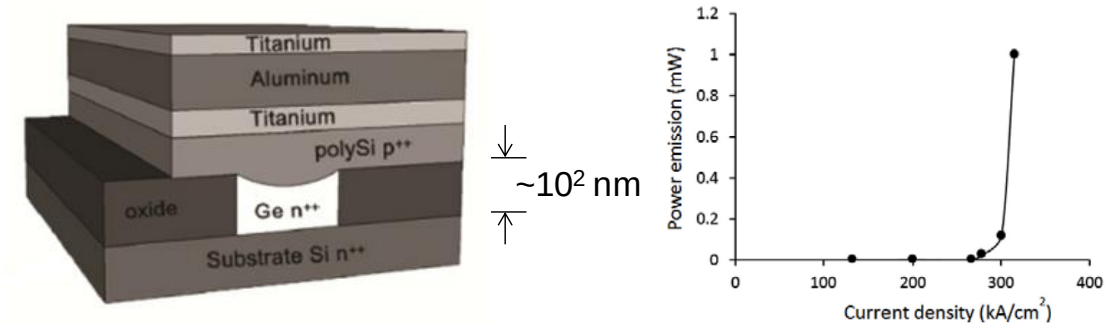

Figure 2-5 Prototype of the electrically pumped Ge-on-Si laser device [23]. Figure reproduced with the permission from Optical Society of America.

In 2015, Koerner et al. from the University of Stuttgart observed lasing from highly doped (3×10^{19} cm^{-1}) unstrained Ge [24]. However, the threshold current density of 510 kA/cm^2 is higher than what was achieved by Kimerling's group at MIT because there is no strain involved. Nevertheless, Kernerner et al.'s experimental results confirmed the reliability of the MIT findings.

Other types of Ge laser are also under development. Lasing from GeSn alloy grown on Si was observed in 2014 [34] by optical pumping. No electrically pumped GeSn lasers have been demonstrated due to the fabrication difficulties. Ge quantum dots (QDs) laser formed by partially amorphizing through Ge-ion bombardment [35] was demonstrated recently, which shows the potential of Ge as a lasing material on Si.

2.5 Thesis Objective

Although the strain introduction methods discussed above can generate high tensile strain inside Ge, they are not suitable for laser designs. The microstructures in [43, 44] are usually difficult to achieve, and it is very inconvenient to inject current and build a p-n junction on such structures.

For the SiN/Ge stripes studied in [41], the top nitride covers the entire Ge top surface, making it difficult to implement a cladding layer and a top contact. The first goal of this work is to design a much more practical stress introduction method and a Fabry-Perot laser structure using this method. Details of the design will be shown in Section 4.6. This design does not interfere with laser structure implementation as the previous work in [41, 43, 44].

A note needs to be added for choosing double-heterostructure Fabry-Perot laser structure here. Double-heterostructure Fabry-Perot lasers were widely used before the introduction of quantum well (QW) lasers. So far, forming QW Ge lasers has been difficult. Yan Cai et al. [45] performed a careful study on forming QW Ge lasers. As the intention of Ge lasers is to solve the material integration challenges between III-V semiconductors and Si, it is not reasonable to introduce III-V semiconductors such as InAs on GaSb to form QWs on Ge. The only two options are forming SiGe/Ge/SiGe or relaxed Ge/tensile Ge/relaxed Ge QWs. Cai et al.'s study showed that the former approach is not effective to reduce the threshold current (I_{th}) [45]. The latter approach, the relaxed Ge/tensile Ge/relaxed Ge structures are challenging to implement since achieving high strain in a thin layer is difficult, so there have not been any experimental efforts on that yet. Therefore, current Ge lasers are still double-heterostructure based.

The second goal of this work is to study whether the new design we proposed would be beneficial for Ge laser performance and to what extent we can optimize the structures to maximize the Ge laser performance. These two questions are important to address, as the available Ge stress engineering methods have major problems for laser structure designs and implementation. Since Ge lasers are still a new concept, it is important for the research community to know whether this topic has a potential with a practical design.

Chapter 3: General Laser Theories

3.1 Introduction of Fabry-Perot lasers and rate equation

Double heterostructure lasers have a three-layer-sandwich structure with wide band gap, low index materials as the outer layer and a narrow band gap, high index materials in the centre as the active region. In this way, both carriers and photons can be confined in the central active region as shown in Figure 3-1. The outer layers are p and n-type doped respectively for the purpose of carrier injection, and the active region is usually undoped to reduce the photon absorption caused by the dopants. However, for our structures, the active Ge region is n-type doped to enhance the emission efficiency. The following theories discussed are called rate equation theory for lasers. Quantum mechanical calculations using the perturbation theory were used to calculate the optical transmission. Due to the page limit, only rate equation theory is discussed here.

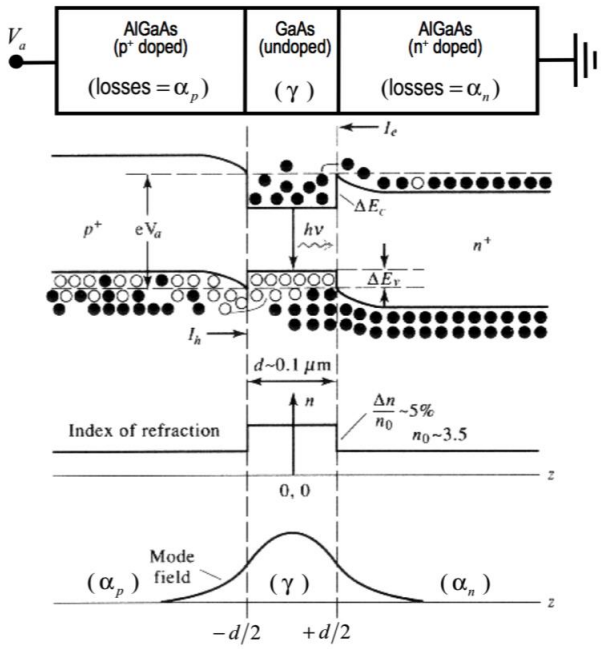

Figure 3-1 Band diagram of a forward biased double-heterostructure laser diode [46].

In undoped or slightly doped active regions, the electron density (N) approximately equals to the hole density (P) because of the charge neutrality. Thus we can simplify the analysis by

specifically tracking only electron density, N, and use it as the carrier density. The change in carrier density N equals to the generation of carriers by injection minus the recombination of carriers, which reads:

$$\frac{dN}{dt} = G_{gen} - R_{rec} \tag{3-1}$$

Here, G_{gen} is the carrier generation rate, and R_{rec} is the rate of carrier recombination rate per unit volume in the active region. G_{gen} is related to the carrier injection and is determined by the injection current I multiplied with an injection efficiency η_i and then divided by electron charge q and active region volume Vol as shown in Eq. (3-2). The injection efficiency or internal efficiency η_i is defined as the percentage of electrons and holes transporting into the active region after surviving the carrier losses due to recombination outside the active regions or carrier overflow into the other side of the p-n junction [47].

$$G_{gen} = \frac{\eta_i I}{qVol} \tag{3-2}$$

$$R_{rec} = R_{SRH} + R_{Aug} + R_{sp} + R_{st} = Rec(N) + R_{st} \tag{3-3}$$

The recombination rate R_{rec} is the combination of several effects: spontaneous recombination rate R_{sp}, SRH recombination rate R_{SRH}, Auger recombination $R_{Aug,}$ and stimulated recombination rate, R_{st} as shown in Eq (3-3). R_{sp}, R_{SRH}, R_{Aug} are all related to carrier density, so a carrier density related recombination term Rec(N) is used as shown in Eq. (3-3). Details of carrier loss are discussed in Section. 3.4. R_{st} is usually written as an individual term as $R_{st} = v_g g(N) S(t)$ because it is related to the photon density S(t). v_g is the group velocity, and g(N) is the gain coefficient. R_{st} represents the photon-stimulated net electron-hole recombination which generates more photons [48].

Taking Eq. (3-3) into Eq. (3-1), the rate equation for the carriers is re-expressed as:

$$\frac{dN(t)}{dt} = \frac{\eta_i I}{qVol} - Rec(N) - v_g g(N) S(t) \tag{3-4}$$

The rate equation for photons in Eq. (3-5) also consists of a loss and a generation term. Light oscillates in the laser structure by reflecting between two mirrors to trigger stimulated emissions. The light that travels inside the cavity can be either absorbed by the material or amplified by triggering the stimulated emission. The main photon generation term for the laser is the stimulated emission term R_{st} and the spontaneous emission term R_{sp} is ignorable. The gain that associates with R_{st} will be discussed in Section 3.5. As indicated in Figure 3-1, the cavity volume occupied by photons and carriers are different. As a result, the photon generation rate should be $\frac{Vol}{Vol_p} R_{st}$ not just R_{st} [48]. The overlap coefficient $\Gamma = \frac{Vol}{Vol_p}$ is called the confinement factor, where Vol is the effective active volume for carriers and Vol_p is the active region for photons. Γ is calculated as the ratio between the integration of light intensity in the active region and the integration of light intensity in all region [49].

$$\begin{aligned} \frac{dS(t)}{dt} &= \Gamma v_g g(N) S(t) - \frac{S(t)}{\tau_{pho}} \\ 1/\tau_{pho} &= (< \alpha_i > + \alpha_m) v_g \end{aligned} \tag{3-5}$$

The photons are lost through the absorption inside the cavity and the light emission at the mirror, which are represented by an internal loss coefficient α_i and a mirror loss coefficient α_m. The internal loss is usually expressed as $<\alpha_i>$, which is the weighted average of the internal loss over all region. We can also use a photon lifetime τ_{pho} to characterize the decay of photons as in Eq. (3-5). The loss mechanism of photons will be further discussed in Section 3.3.

3.2 Threshold condition

When the carrier density is below the lasing threshold condition, the optical loss in the laser exceeds the gain, and the laser does not lase. As the carrier density increases to the point where the gain equals to the optical loss, rate equations reach the threshold condition [11]:

$$\Gamma g(N_{th}) = < \alpha_i > + \alpha_m \tag{3-6}$$

When the threshold condition in Eq. (3-6) is met, the carrier concentration N clamps at a threshold carrier concentration N_{th}. The gain g also clamps at a threshold gain g_{th}. If the current injection increases, the carrier concentration in the cavity increases, and so does the gain g. As a result, more carriers are consumed through stimulated light emissions, which in return decrease the carrier density and gain. The excess carriers injected will recombine to generate photons by stimulated emissions [49]. Therefore, the carrier concentration and gain will clamp at the threshold values.

From the carrier aspect, the carrier absorption also equals to carrier generation since no stimulated emission happens yet. Therefore, threshold current I_{th} is calculated as in Eq. (3-7). It means that the carrier absorption (right-hand side) is equal to the carrier generation (left-hand side).

$$\eta_i \frac{I_{th}}{qdWL} = R_{srh}(N_{th}, P_{th}) + R_{sp}(N_{th}, P_{th}) + R_{Aug}(N_{th}, P_{th}) \tag{3-7}$$

The absorption terms on the right-hand side are electron and hole density dependent. Here d, W, L are the thickness, width, and length of the cavity. $R_{sp}(N_{th}, P_{th})$, $R_{srh}(N_{th}, P_{th})$, and $R_{Aug}(N_{th}, P_{th})$ depend on both threshold hole density P_{th} and threshold electron density N_{th}. This equation holds true for doped region.

After the threshold condition being met, the excess carriers contribute to the stimulated emission. Therfore, the photon density at steady states can be calculated by [48]:

$$S = \eta_i \frac{I - I_{th}}{q\, Vol\, v_g g_{th}} \tag{3-8}$$

The stored optical energy in the cavity can be calculated as: $E_{os} = S\hbar\omega Vol_p$ .The optical power output P_{out} is obtained by multiplying the E_{os} with the energy loss rate through the mirrors $v_g\alpha_m$ [48]:

$$P_{out} = v_g\alpha_m S\hbar\omega Vol_p = \eta_i \frac{\hbar\omega}{q} \frac{\alpha_m}{\alpha_i + \alpha_m} (I - I_{th}) \tag{3-9}$$

If we define slope efficiency or the differential quantum efficiency η_d as in Eq.(3-10), Eq.(3-9) can be simplified as Eq. (3-11). After the threshold, the output power increases linearly with the injection current.

$$\eta_d = \frac{\Delta P_{out}}{\Delta I} \Big/ \frac{\hbar\omega}{q} = \eta_i \frac{\alpha_m}{<\alpha_i> + \alpha_m} = \eta_i \eta_{ext} \tag{3-10}$$

$$P_{out} = \frac{\hbar\omega}{q} \eta_d (I - I_{th}) \tag{3-11}$$

3.3 Optical loss mechanisms

The optical loss mechanisms in lasers are categorized in two types: photons can either be absorbed or escape from the cavity through the end facets for external use. The loss resulted from the escape of photon at end facets is defined as the mirror loss α_m and is expressed as:

$$\alpha_m = \frac{1}{L} \ln\left(\frac{1}{\sqrt{R_1 R_2}}\right) \tag{3-12}$$

L is the length of the cavity, R_1, R_2 are the reflectivity of two end facets. The mirror is usually achieved by simple end clipping or Bragg Grating. At a constant temperature, the loss of the mirror remains constant since the end-mirror reflectivity of the device does not change.

The loss resulted from the absorption is defined as internal loss α_i. One source of the light absorption comes from the metal contact. Metal can absorb light greatly. As a result, when the metal contact is not well positioned, the metal contact can cause a serious light absorption, and cause high internal loss. Details will be discussed in Section 5.2.1. Another source of internal loss inside highly doped semiconductor is the free carrier absorption (FCA) [50]. Free carrier absorption occurs when the free electrons or holes absorb photons and are excited to another excited state. Unlike interband absorption, the free electrons and holes that absorb photons are already excited. Free carrier absorption consists of two parts, free electron absorption (caused by free electrons from the n-type dopants and injected electrons) and free hole absorption (caused by free holes from the p-type dopants and injected holes). The FCA loss of a semiconductor are usually described by the Drude model [51]:

$$\alpha = AN\lambda^2 + BP\lambda^2 \tag{3-13}$$

A and B are the free electron and free hole absorption coefficient, N and P are the electron and hole concentration in the unit of cm^{-3}, λ is the light wavelength in the unit of nm. It can be seen from the formula that the free carrier absorption is proportional to the free carrier concentration. However, when we use the classical Drude model to describe the free electron absorption of biaxially strained germanium, which is in proportion to the square of the wavelength, the Drude model was found to be consistent with the experimental data only in the wavelength range of $\lambda > 15$ μm [52]. At $\lambda < 15$ μm, the free carrier absorption decreases faster with wavelength than predicted by the Drude model [52]. Instead, the free electron absorption properties of Ge can be

described more accurately by using the first principle calculation of the intra-L-valley absorption [53] as compared to the Drude model. With a doping level of 4×10^{19} cm^{-3} and 0.25% tensile strain, the FCA loss is ~20 cm^{-1} in the wavelength range around 1550 nm, which is one order smaller than ~200 cm^{-1} calculated from the Drude model [52]. Compared with the 30 cm^{-1} FCA absorption in GaAs under 5.4×10^{18} n-type doping [54], Ge is slightly better in terms of optical loss.

3.4 Loss mechanism for carriers

Electrons in the conduction band can eventually lose their energy and jump back to the valence band to recombine with holes. This process is called recombination. The energy released from the recombination is transferred in the form of photons or phonons heat. The recombinations that cannot generate photons for lasing are considered as losses. There are three types of recombinations that are considered as loss terms:

1) Spontaneous radiative recombination;

2) Shockley-Read-Hall recombination;

3) Auger recombination.

3.4.1 Spontaneous radiative recombination

In radiative recombination, two forms of emission exist: stimulated emission and spontaneous emission. In spontaneous emission, electrons in the direct conduction band recombine with holes in the valence band and emit photons in random directions. Light emission in light emitting diode (LED) is a typical example of spontaneous emission in semiconductor devices. The recombination of electron-hole pairs can also be stimulated by incoming photons, which is called stimulated emission. The incoming photons interact with the electrons in the conduction band, causing it to

drop to valence band and emit photons with the same frequency, phase, direction and polarization as the incident photons. In a laser, photons emitted are created by the stimulated emission. The spontaneous emission is considered as a loss of carriers, but it can be ignored because most of the radiative emissions are consist of stimulated emissions.

3.4.2 SRH recombination

SRH (Shockley-Read-Hall) recombination is also called trap-assisted recombination. Electrons transit from the conduction band to valence band through defects. Two steps are involved in SRH recombination. In the first step, electrons are trapped by the defect states in the forbidden band. These defects can be either unintentionally introduced to the materials, such as dislocation during fabrication, or intentionally added, like the dopants in the materials. In the second step, if a hole is also trapped at the same energy state as the previous electron, they recombine [55].

The recombination rate depends on the energy levels in the forbidden band introduced by the defects. If the defects' energy level is close to either conduction or valence band, the carriers trapped have more possibility to be re-emitted to the conduction or valence band. Therefore, defects with mid-gap energy levels are very effective for SRH recombination. The SRH recombination rate is calculated by [56, 57]:

$$R_n^{tj} = c_{nj} N N_{tj}\left(1 - f_{tj}\right) - c_{nj} N_{1j} N_{tj} f_{tj} \tag{3-14}$$

$$R_p^{tj} = c_{pj} P N_{tj} f_{tj} - c_{pj} P_{1j} N_{tj}\left(1 - f_{tj}\right) \tag{3-15}$$

R_n^{tj},R_p^{tj} are the electron and hole recombination rates per unit volume through j^{th} deep trap level. N_{tj} is the density of the j^{th} deep trap. c_{nj}, c_{pj} are the electron and hole capture coefficients of the j^{th} deep trap. N is the electron density and P is the hole concentration. f_{tj} is the occupancy possibility of the j^{th} deep trap level, which is calculated from the Fermi distribution function. N_{1j} is the electron concentration when the electron quasi-Fermi level coincides with the energy level E_{tj} of the j^{th} trap.

A similar definition applies to P_{1j}. The first term of Eq. (3-14) (3-15) represents the capture of electrons/holes by a recombination centre, the second term represents the rate of emission of electrons/holes from centres back to conduction/valence band.

τ_{nj} and τ_{pj} are the electron and hole lifetime due to the j^{th} trap, which are the average time for the carriers to decay. They indicate the quality of the material. The better quality the material has, the smaller the lifetime is, the fewer carriers are lost through defects. The lifetime is expressed with capture coefficients by the following relationship [57]:

$$\frac{1}{\tau_{nj}} = c_{nj} N_{tj} \tag{3-16}$$

$$\frac{1}{\tau_{pj}} = c_{pj} N_{tj} \tag{3-17}$$

The capture coefficients c_{nj} and c_{pj} for electrons and holes due to the j^{th} recombination centre can be further expressed as [57]:

$$c_{nj} = \sigma_{nj} \bar{\upsilon}_n \tag{3-18}$$

$$\bar{\upsilon}_n = \sqrt{\frac{8kT}{\pi m_n}} \tag{3-19}$$

$$c_{pj} = \sigma_{nj} \bar{\upsilon}_p \tag{3-20}$$

$$\bar{\upsilon}_p = \sqrt{\frac{8kT}{\pi m_p}} \tag{3-21}$$

$\bar{\upsilon}_n$, $\bar{\upsilon}_p$ are the average thermal velocity of electrons and holes. σ_{nj}, σ_{pj} are the electron and hole capture cross sections of the j^{th} deep trap. m_n, m_p are the bulk effective masses for electrons and holes.

3.4.3 Auger recombination

Auger recombination is a three-particle interaction with 4 energy states. A typical type of Auger recombination, CCCH Auger recombination, is shown in Figure 3-2. In Figure 3-2, when an

electron from energy state 1 jumps to state 2 to recombine with a hole, instead of releasing energy by emitting a photon, the energy is given to another electron to jump from state 3 to 4. This electron in state 4 then thermalizes back down to the conduction band edge. The main type of Auger recombination in Ge can be classified as CCCH, CCHS, and CHHS, where C stands for conduction band, H for valence band and S for the split-off band. The second and third character represent the original states of the particle, those being CC, CH, and HH; the first and fourth character represent the final state after the interaction, those being CH and CS, being CH and CS [30].

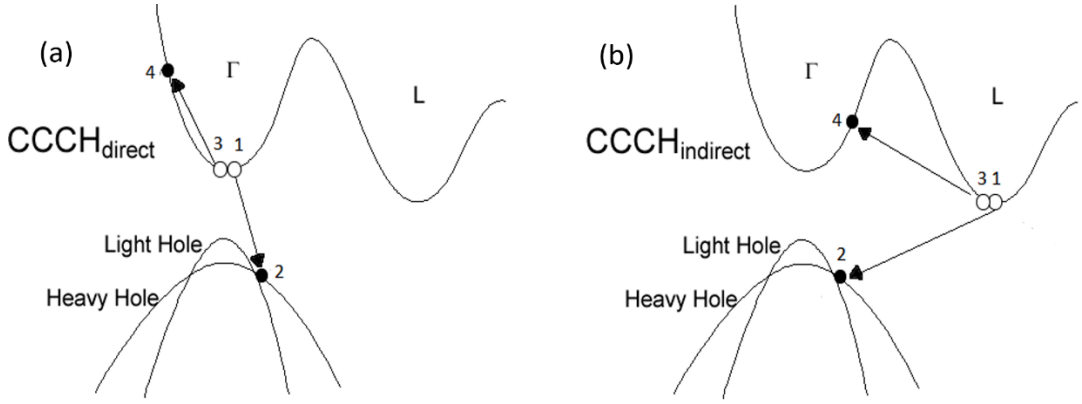

Figure 3-2 Diagram of CCCH (a) direct and (b) indirect Auger recombination. Figure courtesy of Rodolfo E. Camacho-Aguilera at MIT [30].

The Auger recombination rate is given by [47]:

$$\mathrm{R_{Aug}} = (C_n N + C_p P)(NP - N_i^2) \tag{3-22}$$

C_n and C_p are the electron and hole Auger recombination coefficient respectively. N and P are the electron and hole density while N_i is the intrinsic carrier density without doping. From the equation, we can see that the Auger recombination rate is proportional to the cube of carrier concentration under carrier injection condition. Therefore, under high carrier injection, Auger recombination becomes one of the main sources of non-radiative recombination.

The typical value of Auger coefficient for Ge is in the order of 10^{-31} cm^6s^{-1} [58]. However, from the research of Camacho-Aguilera [30], at high doping, the Auger coefficient should be in

the order of 10^{-32} cm^6s^{-1}, which is one order smaller than predicted by the established theory. This result is supported by the experimental results in [59] as shown in Figure 3-3. In the established theory, the radiative carrier lifetime τ in Ge should decrease linearly for both n-type and p-type dopants as illustrated in Figure 3-3 when doping concentration is smaller than 10^{18} cm^{-3}. The radiative carrier lifetime represents the decay of carriers through radiative recombination. Therfore, the reduction of the radiative carrier lifetime means that the radiative recombination is reduced. However, the decrease in the radiative carrier lifetime is reduced under high doping concentration (>10^{18} cm^{-3}). At a doping concentration around 10^{19} cm^{-3}, the radiative carrier lifetime is around $l0^{-6}$ s, which predicts an Auger coefficient in the order of 10^{-32} cm^6s^{-1}.

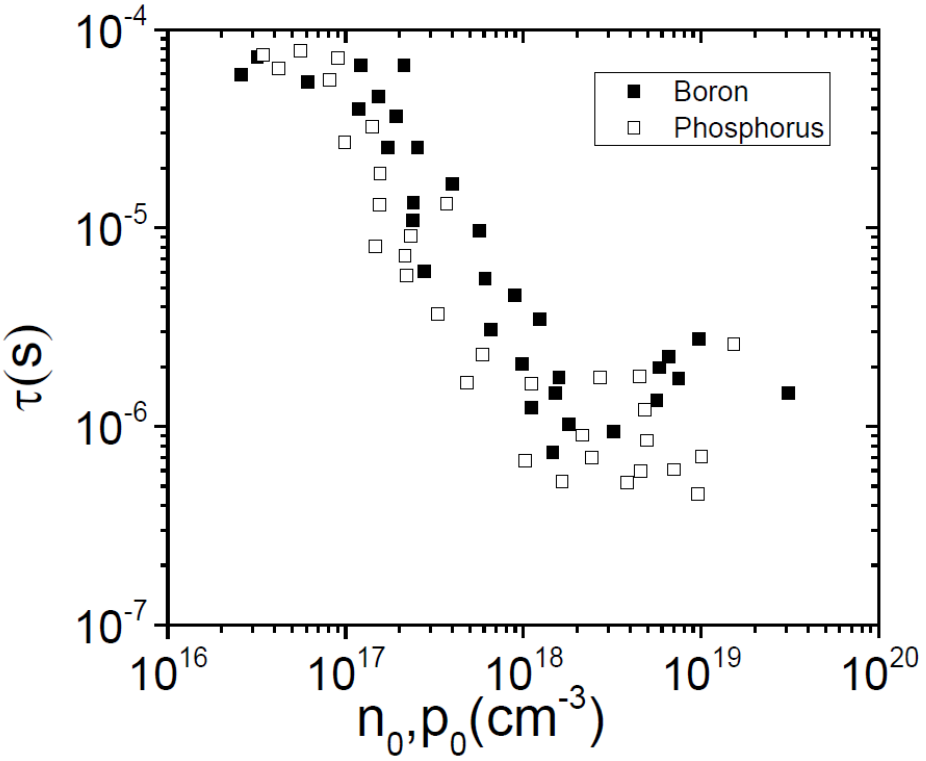

Figure 3-3 Radiative carrier lifetime of n-type and p-type dopants in Ge. Figure courtesy of Rodolfo E. Camacho-Aguilera at MIT [59] [30].

The smaller Auger coefficient can be explained by the indirect CCCH recombination. The threshold energies for different types of Auger recombination mechanisms in Ge were calculated

by Camacho-Aguilera [30] and are listed in Table 3-1. The indirect CCCH shown in Figure 3-2 (b) has the lowest threshold energy, which means a higher possibility of occurring. From Figure 3-2 (b), we can see that when CCCH indirect recombination happens, the carriers that originally stays in indirect L valley jump to direct Γ valley. As a result, CCCH indirect recombination contributes to a higher electron concentration in Γ valley and enhance the radiative emission instead of decreasing the radiative emission as predicted in established theory. Under high doping condition with doping level above 10^{18} cm^{-3}, the increase of carrier concentration in Γ band due to CCCH indirect recombination becomes prominent since Auger recombination increase proportional to the square of doping concentration. As a result, Auger recombination under high doping does not decrease the possibility of radiative recombination, and the Auger coefficient should be in the order of 10^{-32} cm^6s^{-1} [59]. Compared with the typical Auger recombination coefficients in the order of 10^{-31} cm^6s^{-1} for III-V materials [60], Ge is slightly better in terms of Auger recombination because of the CCCH indirect recombination.

Table 3-1 Threshold energy for different Auger recombinations. Table courtesy of Rodolfo E. Camacho-Aguilera at MIT [30].

	Heavy Hole interaction(eV)	Light Hole interaction(eV)
CCCH direct	0.87	1.12
CCCH L-indirect	0.2	0.03
CCCH Δ-indirect	0.24	0.036
CHHS	0.56	1.44
CHHL	0.82	0.82

3.5 Gain

Gain is used to describe the optical amplification in the semiconductor laser. The gain we talk about in the thesis is the material gain, which is only related to the band gap and carrier density

and is not related to the geometry of the laser. When we consider the stimulated emission between energy level 1 and 2, the gain is related to the net stimulated rate [48]:

$$R_{st} = R_{21} - R_{12} = \nu_g g S \tag{3-23}$$

R_{st} is the net stimulated rate, which is the difference between the stimulated emission rate from energy level 2 to 1, R_{21}, and the stimulated absorption of photons from energy level 1 to 2, R_{12}. ν_g is the group velocity, and S is the photon density. Writing out the Fermi factors explicitly, the two radiative transmissions R_{12} and R_{21} become:

$$R_{21} = B_{21} f_c (1 - f_v) S \tag{3-24}$$

$$R_{12} = B_{12} f_v (1 - f_c) S \tag{3-25}$$

The f_c and f_v are the electron's occupation probability at energy level 2 in the conduction band and level 1 in the valence band. B_{21} and B_{12} are the Einstein coefficients for stimulated emission and absorption. The physical meaning of $f_c(1-f_v)$ is the possibility of an electron in the conduction band to occupy the E_c level, and an absence occurs at the E_v level in the valence band. Similar meaning applies to $f_v(1-f_c)$.

Under carrier injection, the electrons in the conduction band and valence band satisfy the non-equilibrium Fermi-Dirac distribution, represented by equations [47]:

$$f_c = \frac{1}{1 + \exp(\frac{E_c - E_{fc}}{kT})} \tag{3-26}$$

$$f_v = \frac{1}{1 + \exp(\frac{E_v - E_{fv}}{kT})} \tag{3-27}$$

E_{fc} and E_{fv} are the quasi Fermi levels of electrons in the conduction and valence band, which are determined by the injection level and doping. E_v and E_c are the energy levels associated with the photon transition. The energy difference of E_v and E_c equals to the photon energy: $E_c - E_v = \hbar\omega$.

From detailed calculation, the B_{21} is equal to B_{12} [47]. Therefore, gain is proportional to the difference of the two Fermi function: $g \propto (f_c - f_v)$

From the theoretical calculations using Fermi's golden rule, optical gain is expressed as [5, 47]:

$$g(\hbar\omega) = C_0\, \rho_r\big(\hbar\omega - E_g\big)(f_c - f_v)$$

$$\rho_r\big(\hbar\omega - E_g\big) = \frac{1}{2\pi^2}\left(\frac{2m_r^*}{\hbar^2}\right)^{\frac{3}{2}}\sqrt{\hbar\omega - E_g} \tag{3-28}$$

$$C_0 = \frac{\pi e^2 |p_{cv}|}{c\varepsilon_0 m_0^2 n\omega}$$

Here, $|p_{cv}|$ is related to the transition matrix factor, n is the refractive index of the material, both of which are the physical properties of the semiconductor material. ρ_r is the joint density of states of direct conduction band (Γ valley) and valence band as a function of photon energy near the band edge. E_g is the band gap energy. m_r^* is the reduced effective mass defined by: $\frac{1}{m_r^*} = \frac{1}{m_c^*} + \frac{1}{m_v^*}$, where m_c^* and m_v^* are effective mass of direct conduction and valence band, respectively. The effective mass will be further discussed in Section 4.3. f_c-f_v is called the population inversion factor. Under thermal equilibrium state and low carrier injection condition, the population inversion factor is negative, thus the gain is negative, showing the property of light absorption. Under high carrier injection level, the population inversion factor is positive, which means that the number of electrons in the conduction band is larger than that in the valence band, and a positive gain will appear. To have a positive gain, we have f_c-f_v>0, which results in:

$$e^{(E_c - E_{fc})/kT} < e^{(E_v - E_{fv})/kT}$$

$$\text{or } E_{fc} - E_{fv} > E_c - E_v = \hbar\omega \tag{3-29}$$

This requirement is called Bernard-Duraffourg inversion condition. Therefore, a positive gain exist only at $E_g < \hbar\omega < E_{fc} - E_{fv}$.

Chapter 4: Ge Laser Related Modeling and Parameters

Developed by Crosslight Software, LASTIP^{TM} (LASer Technology Integrated Program) is a powerful two-dimensional(2D) device simulation program designed to simulate the semiconductor laser. With well-established physical models, it provides users with a quantitative insight into various aspects of a semiconductor laser. Given the structural and material properties, it simulates the laser characteristics. LASTIP^{TM} is one of the most widely used and well-recognized laser simulation tool in industry and academic since 1995. As a result, we use it as the tool of our laser simulation.

Apart from the general laser models, some specific considerations need to be taken into account for Ge laser modeling to include the doping, stress, and interdiffusion effects. The parameters for the models were also carefully selected or fitted to experimental data as discussed below.

4.1 Doping-induced Ge band gap changes

In addition to the tensile strain effect, doping is another factor that causes band gap narrowing. Band gap narrowing is a common phenomenon in n-type or p-type doped semiconductor materials such as silicon, germanium and gallium arsenide. However, few studies have been done on the band gap narrowing effect of Ge with n-type doping. Haas et al. observed the band gap narrowing of the direct and indirect band gap of Ge under N-doping conditions by measuring the infrared absorption and concluded that the direct and indirect band gap have almost the same change under the influence of doping [61]. Recently, researchers also observed a direct band gap narrowing effect with 38 meV reduction in Γ band in 10^{20} cm^{-3} n-type doped Ge LEDs [62]. Jain and Roulston described the indirect band gap narrowing effect of Ge under high doping conditions using the empirical formula Eq.(4-1) [63].

$$\Delta E_g^L = 8.67\left(\frac{N_D}{10^{18}}\right)^{\frac{1}{3}} + 8.14\left(\frac{N_D}{10^{18}}\right)^{\frac{1}{4}} + 4.31\left(\frac{N_D}{10^{18}}\right)^{\frac{1}{2}} \quad (4\text{-}1)$$

Here, N_D is the n-type dopants' concentration in the unit of cm^{-3}.

However, since the fitting parameters in Eq.(4-1) are mostly derived at T = 80 K, this model overestimates the indirect band gap narrowing effect at room temperature. Direct band gap narrowing effect of Ge with n-type doping is not theoretically analyzed in the literature. Therefore, in the modeling of this work, we used a linear relationship between the band gap change with the doping level to deduce an empirical expression for the direct band-gap narrowing effect as proposed in [64]:

$$\Delta E_g^L = 0.013eV + 10^{-21}eV/cm^{-3} \cdot N_D \quad (4\text{-}2)$$

As shown in Figure 4-1, the calculated results in Eq. (4-1) are not in agreement with the experimental data but results of Eq. (4-2) are in good agreement with the direct and indirect band gap narrowing observed experimentally by Haas [61]. Therefore, it is assumed that the direct and indirect band gap of Ge have the same change under the n-type doping [45]. When the n-type dopants' concentration was 4.0×10^{19} cm^{-3}, the direct and indirect band gap narrowing was 0.053 eV.

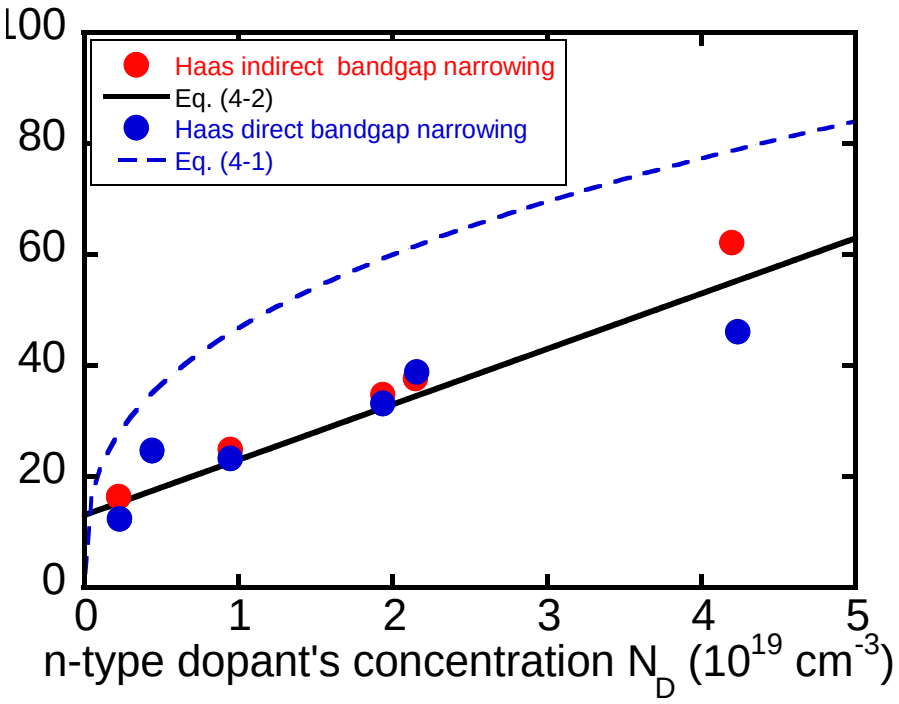

Figure 4-1 n-type band gap narrowing effect of different models at 300 K.

4.2 Stress effect and models

The band gap dependence of Ge on strain can be calculated by k • p theory, Pikus-Bir Hamiltonian and Luttinger-Kohn models [47, 65-67]. The band edge shift can be seen as a combined effect of a hydrostatic strain component ($\varepsilon_{xx}+\varepsilon_{yy}+\varepsilon_{zz}$) and a shear or uniaxial strain component ($\varepsilon_{xx}+\varepsilon_{yy}-2\varepsilon_{zz}$) as listed in Eq. (4-3) to (4-6) [68-70]:

$$E_{C-hh}(k=0) = E_g - \delta E_{hy} + \frac{1}{2}\delta E_{sh} \tag{4-3}$$

$$E_{C-lh}(k=0) = E_g - \delta E_{hy} - \frac{1}{2}\delta E_{sh} \tag{4-4}$$

$$\delta E_{hy} = -a\left(\varepsilon_{xx} + \varepsilon_{yy} + \varepsilon_{zz}\right) \tag{4-5}$$

$$\delta E_{sh} = -b(\varepsilon_{xx} + \varepsilon_{yy} - 2\varepsilon_{zz}) \tag{4-6}$$

The hydrostatic strain component results from a volume change and does not break the symmetry of the crystal. As a result, the hydrostatic strain component only shifts the band edge of the conduction and valence band with a hydrostatic deformation energy δE_{hy} without breaking any band degeneracy [70]. The uniaxial strain component breaks the symmetry of a crystal, and as a result, causes the split of the light hole valence band (lh) and heavy hole valence band (hh) with a shear deformation energy δE_{sh} [68, 69]. ε_{xx}, ε_{yy}, ε_{zz} are the normal strain in x, y, z direction, while x and y are in plain direction and z is the direction that is normal to the plane. a and b are the hydrostatic deformation potential and shear (uniaxial) deformation potential, respectively.

If we write band gap of different conduction band separately and take into account the spin-orbit coupling, the band gap energy values in strained Ge are calculated using the following equations [47]:

$$E_{\Gamma-hh} = E_g + a_\Gamma(\varepsilon_{xx} + \varepsilon_{yy} + \varepsilon_{zz}) + Q_\varepsilon \tag{4-7}$$

$$E_{\Gamma-lh} = E_g + a_\Gamma(\varepsilon_{xx} + \varepsilon_{yy} + \varepsilon_{zz}) - \frac{1}{2}(Q_\varepsilon - \Delta + \sqrt{\Delta^2 + 2\Delta Q_\varepsilon + 9Q_\varepsilon^2}) \tag{4-8}$$

$$E_{L-hh} = E_g + a_L(\varepsilon_{xx} + \varepsilon_{yy} + \varepsilon_{zz}) + Q_\varepsilon \tag{4-9}$$

$$E_{L-lh} = E_g + a_L(\varepsilon_{xx} + \varepsilon_{yy} + \varepsilon_{zz}) - \frac{1}{2}(Q_\varepsilon - \Delta + \sqrt{\Delta^2 + 2\Delta Q_\varepsilon + 9Q_\varepsilon^2}) \tag{4-10}$$

$$Q_\varepsilon = -\frac{b}{2}(\varepsilon_{xx} + \varepsilon_{yy} - 2\varepsilon_{zz}) \tag{4-11}$$

Here, Δ is the spin-orbit splitting energy; a_Γ and a_L are hydrostatic deformation potential at Γ and L valleys; Q_ε is the shear deformation energy. $E_{\Gamma\text{-}hh}$, $E_{\Gamma\text{-}lh}$ are the direct band gap energies between the Γ valley and the heavy hole and light hole band respectively. $E_{L\text{-}hh}$, $E_{L\text{-}lh}$ are the indirect band gap energies between L valley and the heavy hole, light hole valence band, respectively.

From these equations, we can see that heavy hole band is decoupled from the other bands, while light hole band is coupled with the split-off band [47]. Split-off hole (SOH) band is caused by the

spin-orbiting coupling with the band maximum point at K = 0 and is separated from lh and hh band with a spin-orbit splitting energy Δ. The SOH band is far away from the valence band top lh and hh bands. Therefore, it is usually ignored in the discussions of carrier recombination. However, the band shift of the lh band due to the coupling of lh and SOH band cannot be ignored because the resulted difference in lh energy is tens of meV, which is comparable to the lh and hh splitting [47].

The dependences of the band gap energies on biaxial strain are calculated according to Eq. (4-7) to Eq. (4-11) and shown in Figure 4-2 with the biaxial strain assumption that $\varepsilon_{xx} = \varepsilon_{yy}$, and $\varepsilon_{zz} = -2C_{12}/C_{11}\varepsilon_{xx}$. C_{11} and C_{12} are the elastic constants. The strain deformation potentials a_Γ, a_L, Δ and b are obtained from [5, 68, 69] with the values of a_Γ = -10.21 eV, a_L = -4.02 eV, Δ = 0.296 eV and b = -1.88 eV. As the biaxial strain increases, both the direct and indirect band gap decrease and the splitting of lh and hh band increases. The shrinkage of the direct band gap is more pronounced than that of the indirect band gap since the hydrostatic deformation potential for the indirect band a_Γ is larger than a_L. Ge turns into a direct band gap material at about 1.8% biaxial tensile strain, which is consistent with the literature work [71].

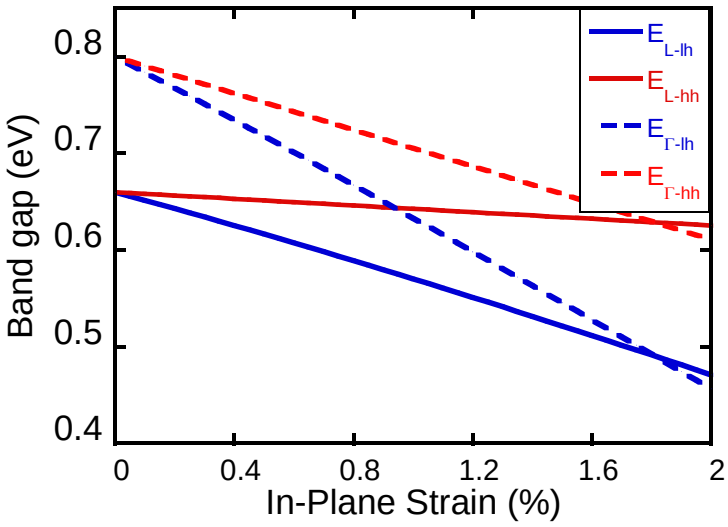

Figure 4-2 Direct and indirect band gap energies under different biaxial strain.

4.3 Effective mass of Γ conduction band

The E (energy)-K (wave vector) relationship of the free electron is $E(K) = \frac{\hbar^2 K^2}{2m_e}$, in which m_e is the free electron mass while $\hbar K$ is the momentum. In a semiconductor crystal, electrons move in a periodic potential field of nuclei and the band edge of conduction and valence band can be approximated by a quadratic equation if we replace the free electron mass with an effective mass m^*: $E(k) = \frac{\hbar^2 K^2}{2m^*}$ [56]. We can obtain the effective mass from the second derivative of E-K diagram. In general, the effective mass might be anisotropic and is a tensorial, which is defined as:

$$\frac{1}{m_{ij}^*} \equiv \frac{1}{\hbar^2}\frac{\partial^2 E(K)}{\partial K_i \partial K_j} \tag{4-12}$$

However, since the Γ conduction band is isotropic, we only have one value m_Γ^*.

A larger effective mass corresponds to a band with a smaller curvature in E-k relation. As a result, a larger effective mass can increase the density of states around the band edge as described in Eq. (3-28) in Section 3.5. Therefore, it can increase the material gain as shown in Figure 4-3, which is calculated from LASTIP™. A larger effective mass also causes the quasi-Fermi level E_{fc} to decrease because the conduction band is broader. The left intersection on the gain profile in Figure 4-3 represents the quasi Fermi level difference E_{fc}-E_{fv} as described in Eq. (3-28). We can see that the change of quasi Fermi level difference due to the change of effective mass is negligible. However, the density of states increases a lot. As a result, the gain increases.

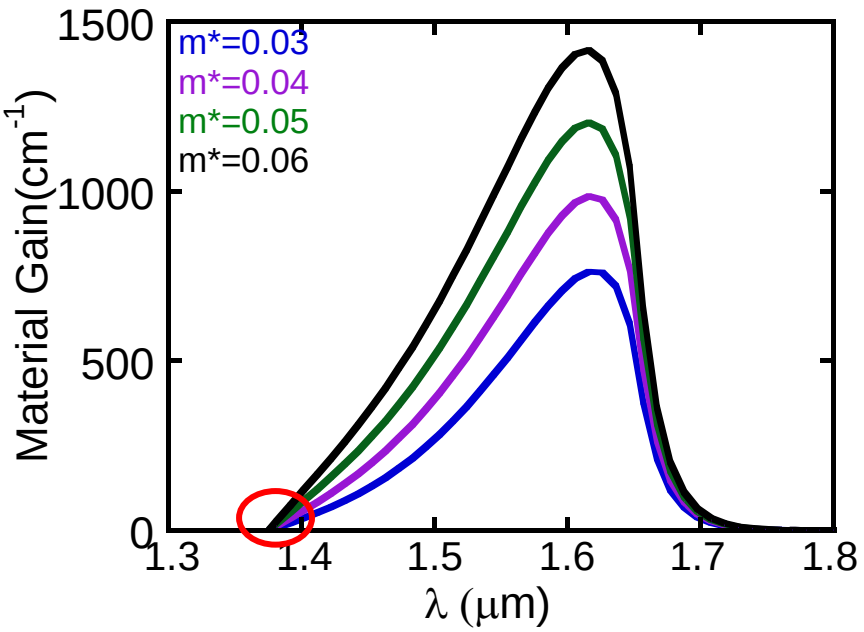

Figure 4-3 LASTIP™'s results of material gain at different m_{Γ}^{*} with 0.25% biaxial strain carrier concentration $n=p=4\times10^{19}cm^{-3}$.

Although in theory, the effective mass of Ge's gamma band should be a constant with a value of $0.041m_e$ [72], Si-Ge interdiffusion makes it a variable. Si-Ge interdiffusion is unavoidable during Ge layer growth, defect annealing and dopant activation annealing. Especially, such interdiffusion is much faster for n-type-doped Ge/Si. Figure 4-4 from [73] shows the Ge profile after defect annealing. More interdiffusion occurs in Phosphorus-doped-Ge/Phosphorus-doped-Si (PGPS) in comparison with undoped-Ge/undoped-Si (UGUS). The thermal budget was 725 ℃ for 64 mins, which is comparable to the condition used in Kimerling's group [23]. Interdiffusion changed part of Ge to a SiGe alloy region. If we define the interdiffusion region is where Si counts for 2% or more, then this region is 200 nm thick for a one-micron thick P-doped Ge/P-doped Si. For the Ge laser with 100 to 300 nm Ge layer thickness, we expect that the interdiffusion region counts for a large portion of the Ge active region, and cannot be ignored.

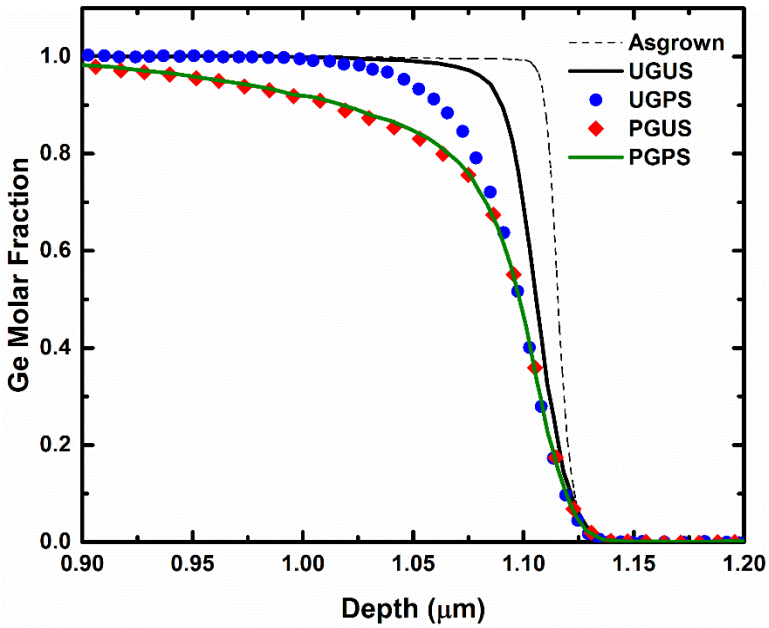

Figure 4-4 Ge profiles measured by SIMS. The Ge profiles are shifted laterally for easy comparison. UGUS: undoped-Ge/undoped-Si; UGPS: undoped-Ge/ Phosphorus-doped-Si; PGUS: Phosphorus-doped-Ge/undoped-Si; PGPS: Phosphorus-doped-Ge/Phosphorus-doped-Si. The black dash line is the Ge profile of sample PGPS before annealing. Figure courtesy of Feiyang Cai at UBC [74].

Due to the limitation of LASTIP^{TM} and the unavailability of the calibrated Ge profile data in the work of Kimerling's group, we were not able to include the full interdiffusion profile into the simulations. Considering the interdiffusion induced SiGe alloy region, it is reasonable to have a bigger effective mass than the Ge value of $0.041m_e$ because Si's effective mass at Γ band ($0.22m_e$) is much larger than that of Ge. Compared to other parameters such as band gap, $m_{e\Gamma}$* has a stronger dependence on the Si molar fraction in the intermixed region due to such a large effective mass difference between Si and Ge. Moreover, $m_{e\Gamma}$* also have a big impact on the L-I behavior as shown in Figure 4-6 on page 47. Therefore, we used the effective mass as a fitting parameter to take the Si-Ge interdiffusion into account.

4.4 Figures of merits of lasers

Several parameters are used for the characterization of laser's performance. These parameters include threshold current I_{th}, slope efficiency η_d, internal efficiency η_i, extraction efficiency η_{ext}, maximum wall-plug efficiency η_{wp}, confinement factor, internal loss, etc.

4.4.1 Threshold current

Threshold current I_{th} is an important parameter to evaluate semiconductor lasers' performance. The smaller the threshold current is, the easier it is for the laser to lase. The magnitude of I_{th} can be derived from the intersection of L-I curve on the I axis. We chose to use I_{th} instead of threshold current density J_{th} as the optimization criteria because I_{th} can reflect the actual laser performance. I_{th} relies heavily on the size of the cavity as described in Eq.(3-7). The longer or wider cavity requires more injection current than a smaller cavity. The structures we discuss have a similar cavity structure, the double-heterostructure Fabry-Perot laser, with changes only in geometry. As a result, using I_{th} for comparison can reflect the actual performance of the device. In the following discussion, we use I_{th} for comparison. Detailed discussions about I_{th} have been done in Section 3.2, and the expression of I_{th} is listed in Eq. (3-7).

4.4.2 Slope efficiency

Slope efficiency η_d is defined in Eq.(3-10). η_d is related to the slope of the L-I (Light-Current) curve ($\Delta P_{out}/\Delta I$) of the laser. It represents the efficiency of photon generation from injected electron-hole pairs. Similar to the desire to lower threshold current of the device, the slope efficiency should be as high as possible when designing the semiconductor laser. A higher η_d means that a laser can generate higher output power in a smaller increment in the current.

Under ideal conditions, the value of η_d is 100%. In a hypothetical ideal laser, over the threshold, an electron-hole pair injected recombines and emit one photon. The released photon resonates in

the optical cavity and is finally emitted from the laser. However, in practical circumstances, only part of the electron-hole pairs can be released through radiative recombination. Only a ratio of the total carriers injected can stay in the active region, which is represented by η_i. The rest of the electron-hole pairs might recombine outside the active layers, pass through the active region without recombination. The carriers inside the cavity still partly lost through non-emitting recombination, which is represented by the threshold current. Then, not all of the released photons can be successfully emitted from the cavity. Part of the photons generated gets absorbed by defects or in the optical cavity as discussed in Section 3.3. The ratio of photons coupling out of the cavity to the total photon density is defined as the extraction efficiency η_{ext}. It is calculated as the ratio of mirror loss to the total loss in the cavity as in Eq. (3-10). The internal loss always exists, which indicates that η_{ext} is smaller than 1 and not all photons can be emitted out. As a result, η_d is the product of internal efficiency η_i and extraction efficiency η_{ext} to represents the electron-to-photon conversion efficiency.

4.4.3 Maximum wall-plug efficiency

Wall-plug efficiency is the core parameter for the laser devices. It is defined as the ratio of optical power generated to the electrical power consumed and represents the overall energy conversion efficiency of the laser. The electrical power that is not converted to optical power is dissipated in the form of heat. Heat generation is one of the leading cause of laser degradation [75]. Therefore, a higher wall-plug efficiency does not only cut down the electric power needed for a certain optical output power but also lowers the power budget for the cooling system.

The voltage dependence of the current of the laser is similar to PN diode. When the current is above the threshold current, the diode is forward biased, and the laser can be seen as a resistor. The operation voltage V_{op} is operation current I_{op} multiplied by the series resistance R plus the

diode voltage V_D as described in Eq (4-13). Therefore, the final expression for wall-plug efficiency is shown in Eq (4-14). In the calculation of η_{wp}, 2D laser L-I and I-V simulations were performed up to about 10 mW optical output, above which, to save computation time, L-I and I-V curves were extrapolated linearly up to about 200 mW optical output according to Eq. (4-13), (4-14). From Eq. (4-14), we can observe that wall-plug efficiency peaks and then decrease. We define the maximum wall-plug efficiency as $\eta_{wp,}$ which is shown in Eq. (4-14), to evaluate the performance of laser because it represents the best energy conversion efficiency of the device.

$$P_{elect} = I_{op}V_{op} = I_{op}(V_D + R_s I_{op}) = V_D I_{op} + R_s I_{op}^2 \tag{4-13}$$

$$\eta_{wp} = Max[\frac{P_{opt}}{P_{elect}}] = Max[\frac{\frac{\hbar\omega}{q}\eta_d(I_{op}-I_{th})}{V_D I_{op}+R_s I_{op}^2}] \tag{4-14}$$

4.5 Modeling with LASTIP™ and model calibrations

We first simulated the experimental laser structure from Kimerling's group [23] to calibrate our model. The cross section is illustrated in Figure 4-5. The Ge cavity was 1 μm wide, and 270 μm long, and the thickness of Ge active layer was set to be 200 nm, which was the average value of the 100~300 nm thickness in the experiments due to the process non-uniformity [23, 30]. On both left and right side of the Ge cavity, a 0.5 μm wide oxide was used for optical confinement, and 180 nm thick polysilicon was deposited on top of Ge as the cladding layer. The metal layers contained two layers of 0.1 μm thick Titanium (Ti) and 1 μm thick Aluminum (Al) layers as illustrated in Figure 4-5. 2 μm Si substrate was used in the simulations. Virtual contacts were defined underneath the bottom of the Si substrate and on the top of metal layers for the biasing purpose, and they do not have interactions with light. This simplification is valid because the light field only penetrates Si to a depth much less than 2 μm as shown in Figure 4-8 (c)-(e). The doping and the strain are the same as the experiments reported: Si substrate was 5×10^{19} cm^{-3} n-type doped.

Ge was 4×10^{19} cm^{-3} n-type doped with 0.25% biaxial tensile strain resulted from the thermal mismatch. Polysilicon is 5×10^{20} cm^{-3} p-type doped.

The strain-dependent Ge energy band gap model in Section 4.2 and the doping induced band gap narrowing effect in Section 4.1 were implemented in LASTIP™. The metal-semiconductor heterojunctions were aligned by electron affinity as described in [47]. The reflectivity values of two facet are $R_1 = 23\%$ and $R_2 = 38\%$, which correspond to a mirror loss α_m of 45 cm^{-1} [45]. Auger coefficients used were $C_n = 3.0 \times 10^{-32}$ cm^6/s and $C_p = 7.0 \times 10^{-32}$ cm^6/s [30, 32]. The index of refraction values of all materials were wavelength dependent. Since the surface is correctly passivated in the experiment, surface recombination can be ignored [30]. 1 ns of defect limited carrier lifetime ($\tau_{p,n} = 1\ ns$) was used as a conservative estimation [76]. This is a conservative assumption compared with the measurement of Ge's carrier lifetime of 5.3 and 3.12 ns in recent studies [77, 78]. For simplicity, a default setting in the software with a uniform distribution of donor mid-gap traps with a density of 10^{10} m^{-3} was used. LASTIP™ takes $\tau_{p,n}$ as an input to calculate the capture coefficients c_{nj}, c_{pj} according to Eq. (3-16)(3-17) and then SRH recombination rates R_n^{tj}, R_p^{tj} are calculated accordingly by Eq. (3-14)(3-15).

For the optical loss, we assumed that the internal loss and the mirror loss are the primary sources of the loss and internal loss is dominated by the free carrier absorption [50]. In LASTIP™, the free carrier absorption in a narrow wavelength range was simplified as α=AN+BP. We used the maximum value of the first principle calculations results of free carrier absorption in n-type doped Ge for n-loss coefficient: $A = 5.0 \times 10^{-19}$ [52] , and the experimental measurement results in p-type doped Ge [79] and the modeling results in [26] were used as a starting point to obtain the best fitting to the L-I curve in [23]. The effective mass of gamma conduction band ($m_{e\Gamma}$*) was assumed to be equal everywhere in the Ge cavity and was used as the first fitting parameter of L-

I curve. The p-loss coefficient B was used as the second fitting parameter. The best fitting was obtain when $m_{e\Gamma}$* = 0.0457 m_e and the best fitting free carrier loss relation was $\alpha_i = 5.0 \times 10^{-19}N + 1.023 \times 10^{-17}P$.

The free carrier absorption properties of the silicon substrate and the polysilicon covering layer can be obtained from the conclusions in [80] and [81] as shown by equations (4-15) and (4-16). Free carrier absorption of the silicon substrate can be described as:

$$\alpha = 1.8 \times 10^{-18}N + 2.7 \times 10^{-18}P \quad (4\text{-}15)$$

Free carrier absorption of polycrystalline silicon cladding layer is:

$$\alpha = 1.079 \times 10^{-17}N + 7.47 \times 10^{-18}P \quad (4\text{-}16)$$

We can observe that under high doping condition of our structure, polysilicon and silicon have higher loss than the Ge cavity. As a result, light that travels outside of Ge cavity experiences higher optical loss.

The parameters used for simulation are summarized in Table 4-1. Using these parameters, our model produced a J_{th} of 300 kA/cm^2 or I_{th} of 800 mA at 15 ℃ with the transverse electric (TE) mode lasing at λ = 1676 nm. These results were very close to the experimental values of J_{th} = 280 kA/cm^2 and the lasing wavelength of 1650 nm [23]. As seen in Figure 4-6, the model can match the experimental L-I curve quite well. Sensitivity test results are shown in Figure 4-6, which shows how a smaller FCA parameter or a smaller $m_{e\Gamma}$* are not fitting the experimental data. We can observe that the simulation results are quite sensitive to the change of $m_{e\Gamma}$*. A 1% change in $m_{e\Gamma}$* will result in a 10% change in I_{th}.

Table 4-1 Material parameters used in the modeling of Ge laser [26]

Material parameters	Value	Material parameters	Value
Cavity thickness	0.2 μm	Ge refractive index at 1550nm	4.18
Cavity width	1 μm	Si refractive index at 1550nm	3.46
Cavity length	270 μm	Max mobility for electrons	3900 $cm^2V^{-1}s^{-1}$
Biaxial strain	0.25%	Max mobility for holes	1900 $cm^2V^{-1}s^{-1}$
Temperature	288 K	Gamma band effective	$0.0457m_e$
Facet reflectivity R_1,R_2	23%, 38%	L band effective mass	$0.22m_e$
Electron Auger coefficient	3.0×10^{-32} cm^6s^{-1}	Heavy hole effective mass	$0.284m_e$
Hole Auger coefficient C_p	7.0×10^{-32} cm^6s^{-1}	Light hole effective mass	$0.043m_e$

It should be noted that although Xiyue Li et al.'s models [26] also fit the same experimental data, they used the FCA (free carrier absorption) coefficients as the fitting parameters and did not consider Si-Ge interdiffusion. In our modeling, we chose to use $m_{e\Gamma}$* as the fitting parameters to include the effect of interdiffusion. One should notice that fitting $m_{e\Gamma}$* to the experimental data is a rough estimation to take the interdiffusion into account and further study is required. The limitation of this method will be discussed in Section 4.7.

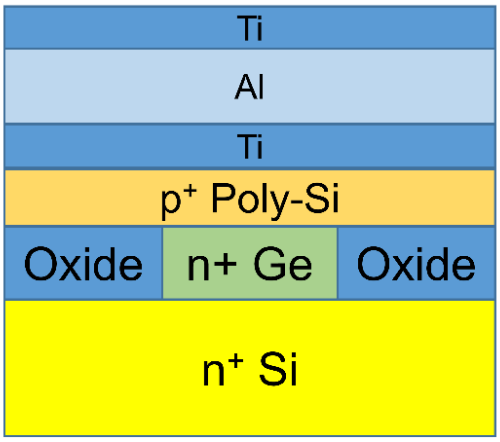

Figure 4-5 Cross-section of the Ge-on-Si heterojunction laser structure simulated.

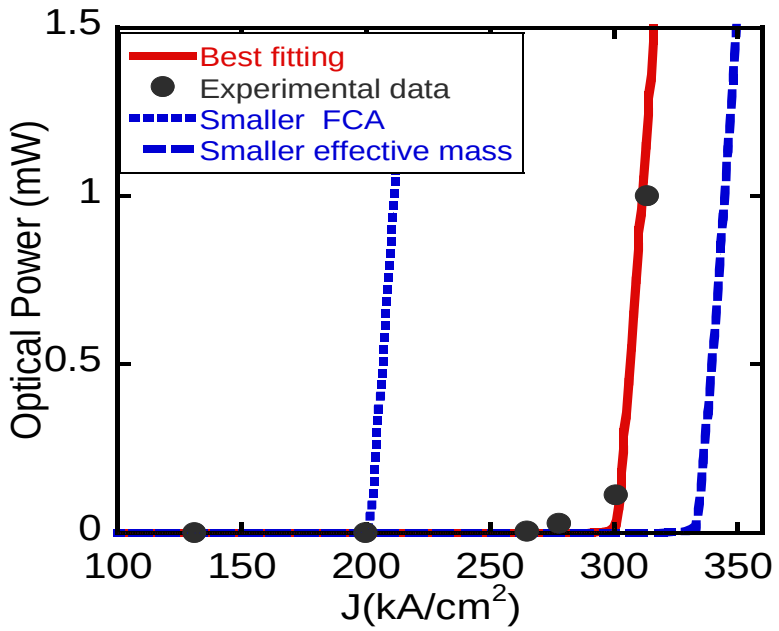

Figure 4-6 L-I curves for the experimental result, calibration result, and sensitivity tests with a smaller FCA loss: $\alpha_i = 5.0 \times 10^{-19} N + 0.923 \times 10^{-17} P$, and a smaller effective mass $m_{e\Gamma}^* = 0.0453\ m_e$.

4.6 Modeling of Ge laser with stressors

We studied two structures with silicon nitride stressors as illustrated in Figure 4-7: structure 2 with side stressors only and structure 3 with top and side stressors together. The structure without stressors in Figure 4-6 (a) has the same structure as the electrically pumped Ge laser in [23] and

is named as structure 1 for comparison. In structure 2, we replace the oxide in structure 1 with side SiN stressors to introduce strain in Ge cavity. In structure 3, a top stressor was added along with the side stressors. The top stressor was put on top of the polysilicon layer to leave room for current injection. The top stressor has the same width as the Ge cavity and is 0.3 μm thick. The consideration is that a wide c-SiN blocks current flow from the top contact to the substrate, which means an increase in series resistance. If the top stressor is too narrow, then the stress effect will not be as big.

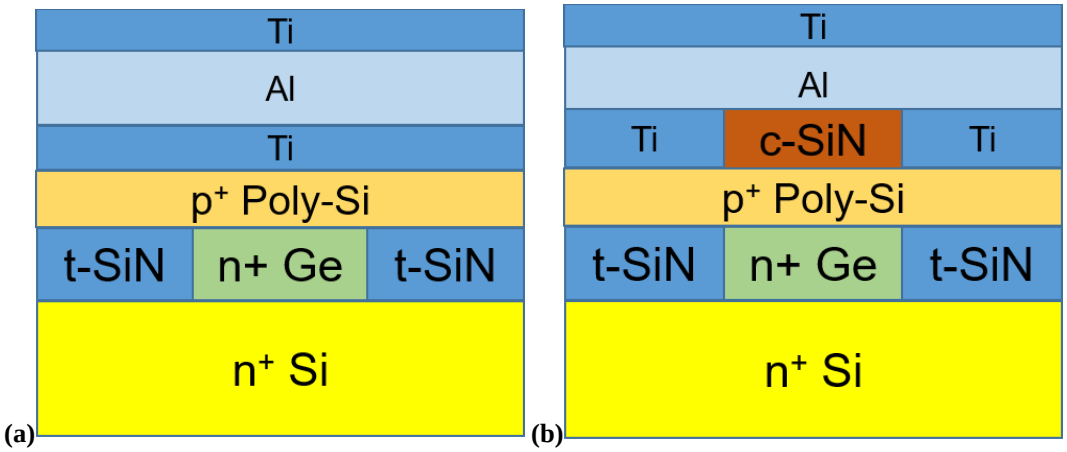

Figure 4-7 Laser structure simulated (cavity width = 1 μm, thickness = 0.2 μm, length = 270 μm, cladding thickness = 0.18 μm). (a) Structure 2: with side nitride stressors; (b) Structure 3: with top & side nitride stressors. The width of the top nitride stressor is the same as that of the Ge cavity. The metal contacts are composed of Ti and Al same as those in Ref. [23], shown in Figure 4-6.

The refractive index of SiN is around 1.9 and is set to be wavelength dependent according to [82]. Therefore, it is suitable for optical confinement. The 2D optical field of 3 structures are shown in Figure 4-8 (c)-(e). We can observe that the SiN stressors can confine the light as good as the oxide. From the 1D cut profile in Figure 4-8 (a), we can observe that the light at the top is absorbed by the top metal contact in structure 1 and 2 and this absorption causes high optical loss. In structure 3, the absorption caused by the metal contact is diminished because of the existence of SiN top stressor as shown in Figure 4-8 (b).

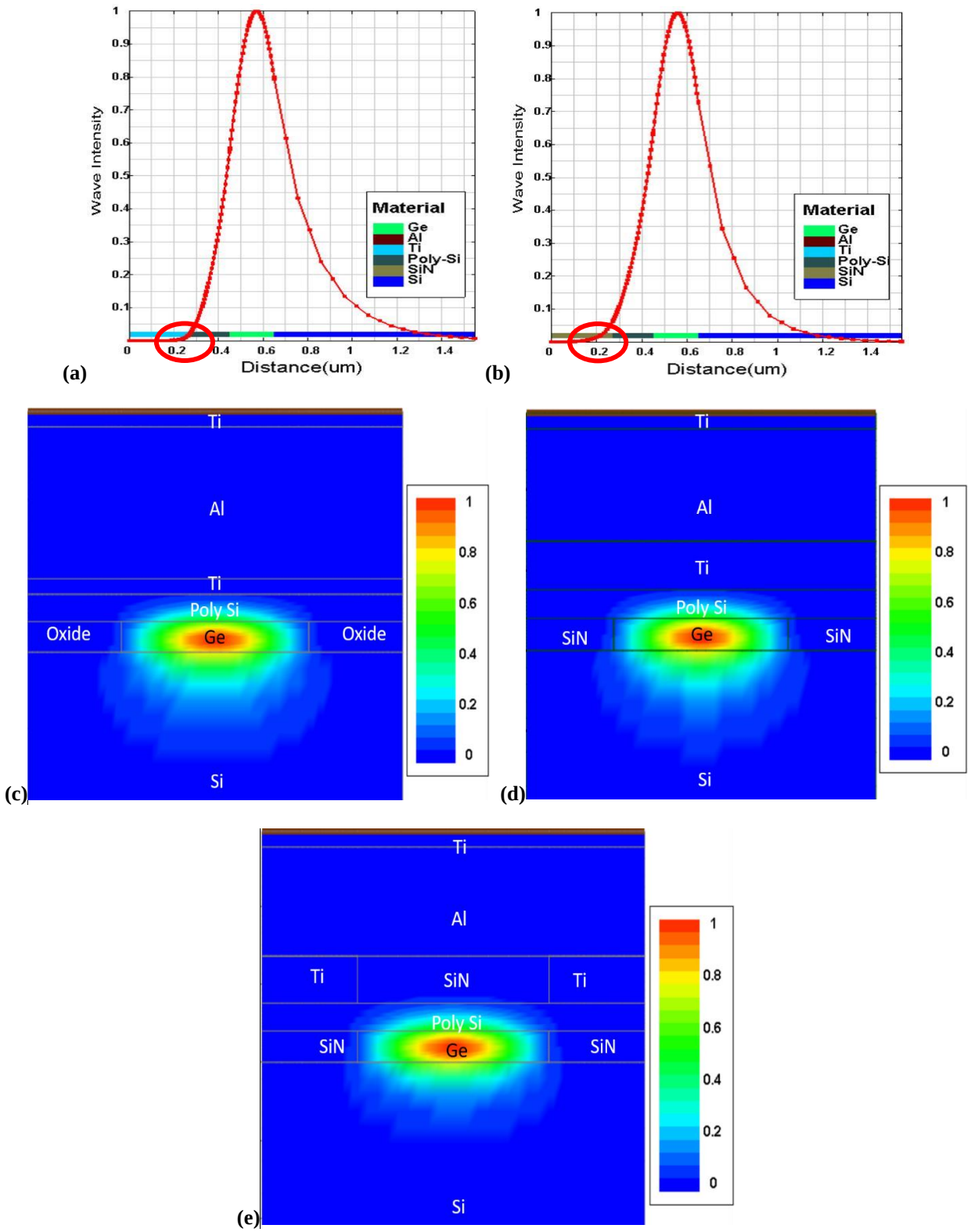

Figure 4-8 Normalized light intensity of 1D cut in the centre line of (a) structure 2 (structure 1 have a similar distribution); (b) structure 3. 2D profile of (c) structure 1; (d) structure 2; (e) structure 3.

We used the software TSUPREM-4^{TM} for the modeling of strain field in structure 2 and 3. TSUPREM-4^{TM} is a standard and extensively used two-dimensional (2D) technology computer aided design (TCAD) tool for process simulation in the semiconductor industry. The advantage of TSUPREM-4^{TM} is that it contains well-calibrated models based on decades of industry practice and includes several mechanisms for stress/strain introduction. These mechanisms include volume changes during oxidation, thermal mismatch between materials, intrinsic strain in deposited layers, and surface tension.

For strain introduced by SiN stressors, a plane strain assumption (strain in length direction $\varepsilon_{yy} = 0$) is suitable since the length dimension is much longer than the width and thickness dimensions. A tensile strain value of 0.25% in Ge resulted from the thermal expansion mismatch between Ge and Si in ε_{xx} and ε_{yy} was added on top of the strain introduced by stressors as the two types of strain comes from two independent sources. Ge's Young's modulus and Poisson ratio used were 102 GPa and 0.28 respectively. Silicon nitride has a Young's modulus value ranging from 100 GPa to 350 GPa depending on the deposition method and recipe. For simplicity, a medium Young's modulus value of 200 GPa in [83] was used for silicon nitride and the Poisson ratio used was 0.24. The intrinsic stress values used for tensile silicon nitride (t-SiN) and compressive silicon nitride (c-SiN) were +2 and -2 GPa respectively, both of which were common values already achieved in CMOS processing. After every deposition and etch step, a stress relaxation step was used in the software to calculate the stress change.

Since ε_{xx} and ε_{yy} appear in the form of $\varepsilon_{xx}+\varepsilon_{yy}$ in the strain-dependent band gap models in Eq.(4-7) to (4-11) as discussed in Section 4.2, it is reasonable to use effective biaxial strain $\varepsilon_{eb} = \frac{(\varepsilon_{xx}+\varepsilon_{yy})}{2}$ to represent the in-plane strain magnitude for the following discussions. The strain maps of ε_{eb} and ε_{zz} of structure 2 and 3 are illustrated in Figure 4-9 and Figure 4-10.

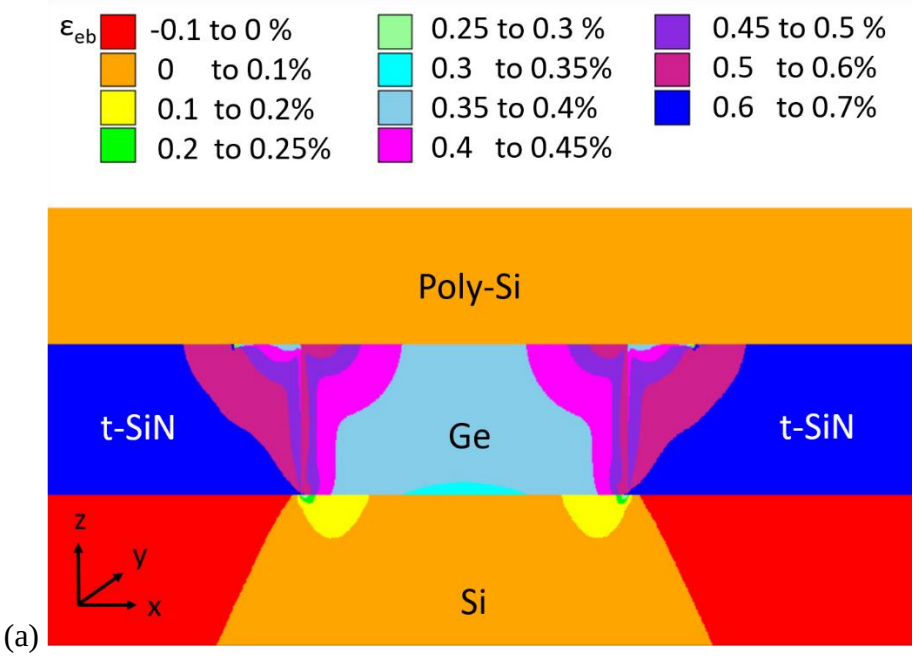

(a)

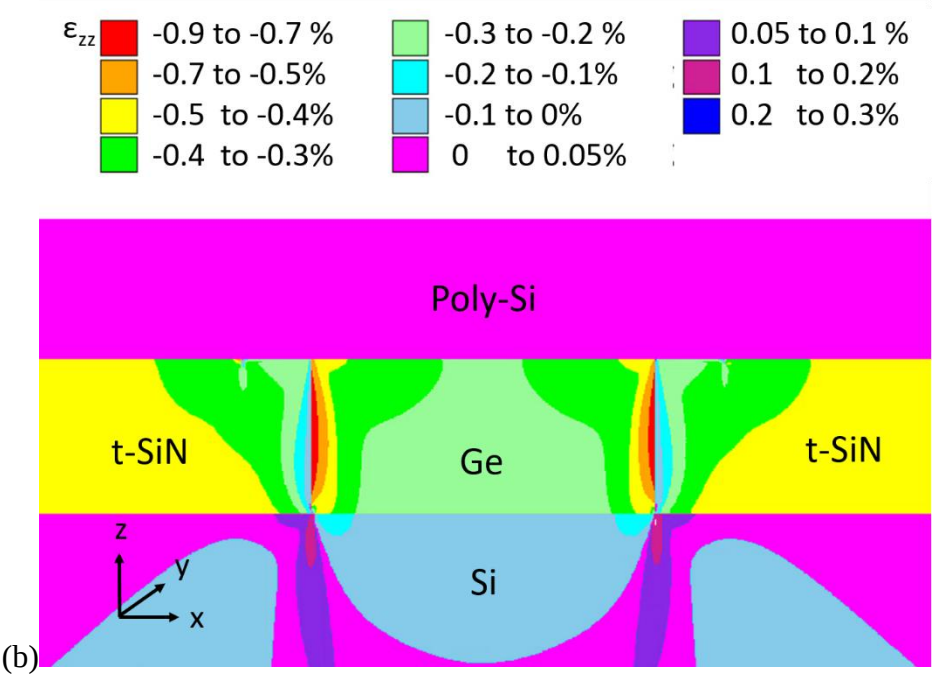

(b)

Figure 4-9 2D Strain map on the cross section: (a) ε_{eb} (b) ε_{zz} of structure 2 with side stressors only（cavity width = 1 μm, thickness = 0.2 μm, cladding thickness = 0.18 μm).

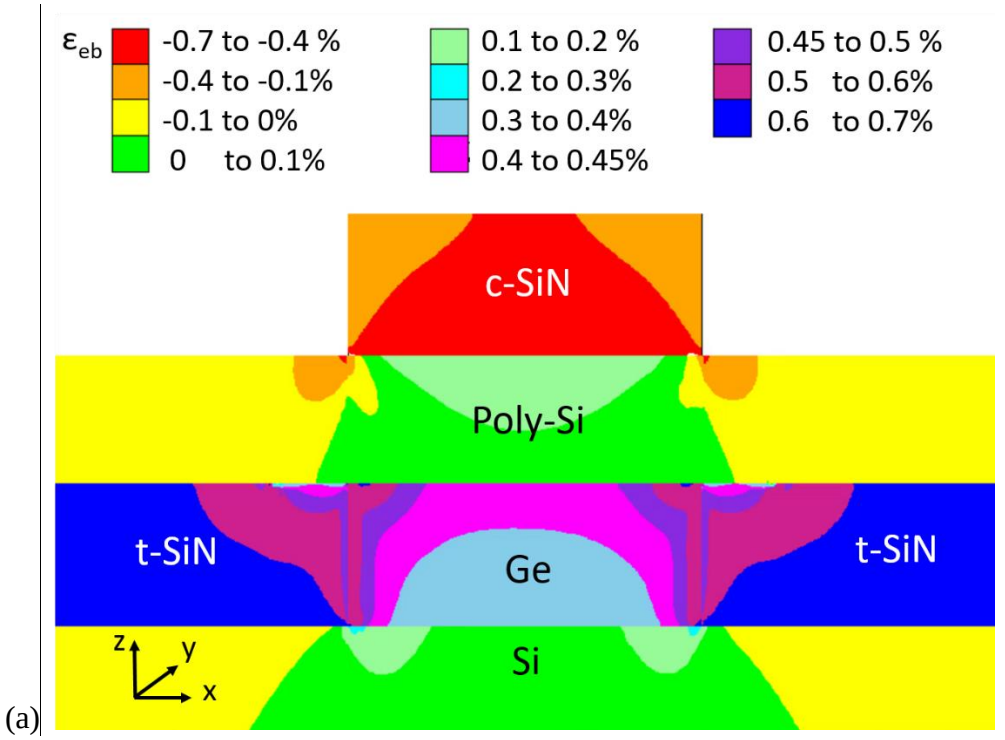

(a)

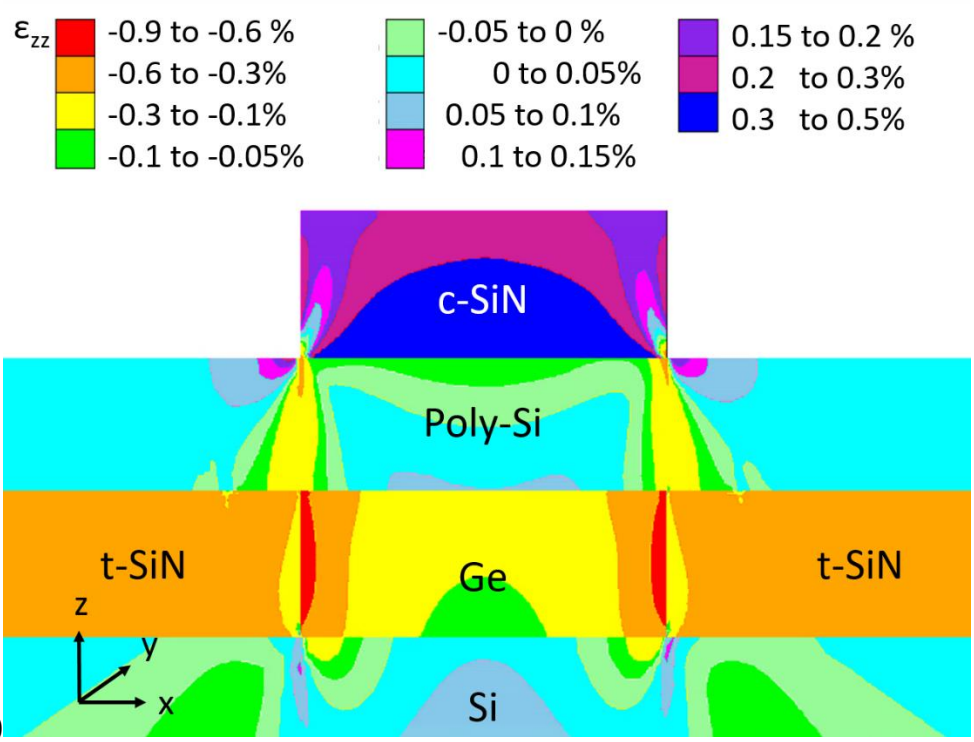

(b)

Figure 4-10 2D Strain map on the cross section: (a) ε_{eb} (b) ε_{zz} of structure 3 with side and top stressors (cavity width = 1 µm, thickness = 0.2 µm, cladding thickness = 0.18 µm).

Significant ε_{eb} were introduced by the stressors as shown in the strain map. The average value in the centre line was used to represent the strain field for simplification. With only side stressors, 0.36% average ε_{eb} was introduced including the 0.25% strain caused by the thermal expansion mismatch. The value was increased to 0.39% by adding a top stressor and we can see from the strain map that the ε_{eb} in the upper part of Ge is greatly increased. This strain enhancement is not optimized due to the non-optimized Ge width and thickness as the stress introduction strongly depends on the sizes of cavity and stressors, and their relative positions.

The three average strain (ε_{xx}, ε_{yy}, and ε_{zz}) in the centre line were loaded into LASTIP^{TM}. Due to the limited capability of LASTIP^{TM} in introducing strain, some transformation is needed. In LASTIP^{TM}, A biaxial assumption ($\varepsilon_{xx} = \varepsilon_{yy} = \varepsilon_b, \varepsilon_{zz} = -\frac{2C_{12}\varepsilon_{xx}}{C_{11}}$) is used as the strain model, and only biaxial strain ε_b is used as an input. However, from the strain simulation results, the strain gained from SiN stressors does not meet biaxial assumption. In order to incorporate non-biaxial strain into LASTIP^{TM}, the effective deformation potential a_{eff} and b_{eff} discussed below were used.

Under the biaxial assumption, the hydrostatic term in Eq. (4-5) becomes:

$$\delta E_{hy} = -a(\varepsilon_{xx} + \varepsilon_{yy} + \varepsilon_{zz}) = -a\left(2 - \frac{2C_{12}}{C_{11}}\right)\varepsilon_b \tag{4-17}$$

We use $\beta=\varepsilon_{zz}/\varepsilon_{eb}$ to express ε_{zz} in terms of effective biaxial strain ε_{eb}. Then the hydrostatic term becomes:

$$\delta E_{hy} = -a(\varepsilon_{xx} + \varepsilon_{yy} + \varepsilon_{zz}) = -a(2+\beta)\varepsilon_{eb} = -a_{eff}\left(2 - \frac{2C_{12}}{C_{11}}\right)\varepsilon_{eb} \tag{4-18}$$

$$a_{eff} = \frac{a(2+\beta)}{\left(2 - \frac{2C_{12}}{C_{11}}\right)} \tag{4-19}$$

If we use a_{eff} instead, the hydrostatic term is in the same form with the biaxial assumption. A similar approach was applied to uniaxial components:

$$\delta E_{sh} = -b\left(\varepsilon_{xx} + \varepsilon_{yy} - 2\varepsilon_{zz}\right) = -b(2 - 2\beta)\varepsilon_{eb} = -b_{eff}\left(2 + \frac{4C_{12}}{C_{11}}\right)\varepsilon_{eb} \quad (4\text{-}20)$$

$$b_{eff} = \frac{b(1-\beta)}{\left(1 + \frac{2C_{12}}{C_{11}}\right)} \quad (4\text{-}21)$$

After implementing the strain data into LASTIP^{TM} using the method above, laser simulation of three structures were performed. The L-I curve of three structures are shown in Figure 4-11. Compared to Structure 1, by adding the side stressors, about 523 mA reduction in I_{th} and 1.05% increase in η_{wp} were obtained. The increased strain greatly improves the performance of laser. And in Structure 3, by adding the top and side stressors together, about 761 mA reduction in I_{th} and 12.9% increase in η_{wp} were obtained (Figure 4-11 and Table 4-2). The significant performance improvement introduced by the top stressors is because that top stressor not only introduces higher strain, but also decreases the optical loss caused by the metal contact as discussed previously.

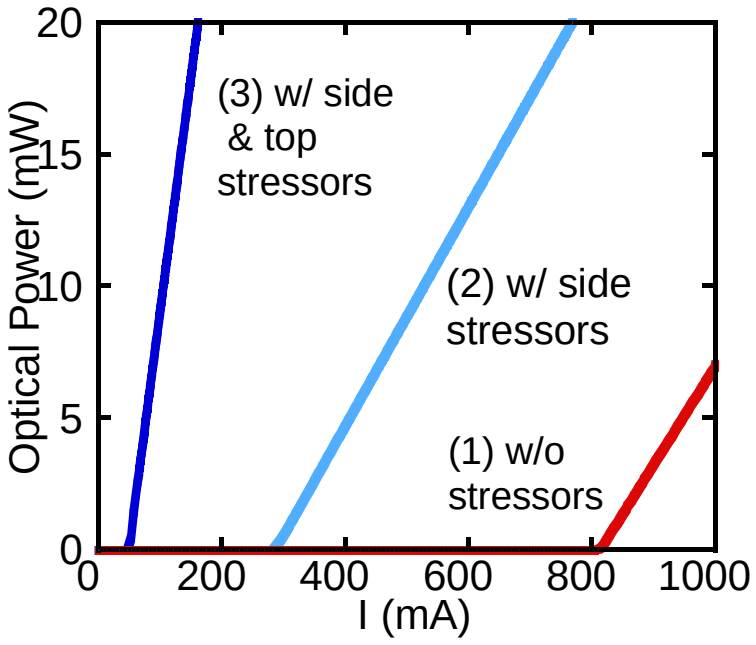

Figure 4-11 L-I curve comparison for the three structures before the structure optimizations.

Table 4-2 Laser performances of the three structures in Figure 4-11.

Structure	1	2	3
ε_{eb}	0.25%	0.36%	0.39%
I_{th} (mA)	810	287	49
Slope efficiency η_d	6.33%	7.20%	31.94%
η_{wp}	2.07%	3.12%	16.03%

4.7 Limitations of our modeling

Although our models can fit the experimental data quite well, it still has some uncertainties and limitations. The parameters that influence the results most are the effective mass, defect limited carrier lifetime, Auger coefficients, FCA coefficients, and strain. The uncertainties of these parameters lie in four aspects: 1) the not-well-studied Ge parameters, 2) modeling simplification and limitation of the simulation tool, 3) limited experimental data, and 4) the lack of research of the delta valley in Ge band structure.

Firstly, Ge is not a well-studied optical material, and many model parameters do not have widely agreed values or even ranges. The Auger coefficients discussed in Section 3.4.3 are a typical example. Under high doping and carrier injection, the values of Auger coefficients of Ge are one order smaller than that of lightly-doped Ge [30]. The FCA loss discussed in Section 3.3 is also one order smaller than predicted by the traditional Drude model [52]. For the defect limited carrier lifetime, it highly depends on the fabrication method, and no experimental results are available. As a result, there is a large uncertainty associated with the value of $\tau_{p,n}$. The parameters we used mostly come from the research of Kimerling's group as they pioneered the research of Ge optical properties, and provided a complete set of theoretical studies and experimental data on Ge lasers.

Secondly, several simplifications were used in our modeling. Due to the limitation of LASTIP^{TM}, only one strain value can be assigned to Ge. As a result, we used the average strain in the centre

line of Ge cavity and assumed that the strain in the Ge cavity is constant in the Ge cavity. From the strain field in Figure 4-9 and Figure 4-10, we can observe that most part of the cavity shares similar strain values with the central line and only the edges of the Ge cavity have a large value. Since the heterogeneity of strain only happens on the edges of the Ge cavity and light concentrates in the centre of the cavity, the strain in the centre is more important. Therefore, using the average strain in the centre line is reasonable.

Another simplification is to use the effective mass of gamma conduction band, m_{Γ}^{*}, as a fitting parameter to capture the Si-Ge interdiffusion since LASTIP^{TM} is not able to load a real Ge concentration profile. Details were discussed in Section 4.3. In the structure optimization in Chapter 5, we assumed that m_{Γ}^{*} does not change with the geometry. In reality, more complicated processes are involved. For example, the method used in the work of Kimerling's group to fabricate highly doped Ge is a low temperature/high temperature (LT/HT) epitaxial growth with delta doping. It commonly has three major steps. The first step is the initial Ge seeding layer growth at low temperature (300 – 400 °C). This layer is 50 - 100 nm thick and is highly defected due to the large lattice mismatch between Ge and Si that needs to be relaxed in this layer. The second step is a high-temperature growth (600 – 850 °C) of Ge, which is of higher Ge film quality and faster growth rate. Therefore, we can see that if the Ge cavity is thicker, a bigger percentage will be grown by the HT step and the interdiffusion effect is weaker since the most interdiffusion region is the bottom Ge region (the seeding layer region). The third step is delta doping and followed by a high temperature (~ 700 °C) and long time (~ 60 mins) drive-in annealing at which most of the interdiffusion happens. Multilayers of dopants were grown on top of active Ge layer and then a drive-in annealing is required for the dopants to diffuse into Ge cavity. A thicker cavity requires longer drive-in time for the dopants to diffuse over the whole cavity, and as a result, the

interdiffusion becomes more serious. Therefore, the interdiffusion region might account for the similar percentage in the Ge thickness and a constant m_{Γ}^{*} is reasonable. The impact of interdiffusion on laser performance is an important topic for future studies since I_{th} is rather sensitive to the m_{Γ}^{*}. However, all of these interdiffusion processes are difficult to model at this point due to the limited experimental data. The only experimental data is at a thickness around 0.2 μm.

Another uncertainty lies in the delta valley of Ge, which is the second indirect valley in the conduction band that located only 50 meV above the Γ valley. Under high injection condition, the delta valley might consume carriers and result in a higher threshold current. However, the research about the impact of delta valley on laser performance is very limited, and the band shift in the presence of strain is not well studied. In our modeling, we were not able to take the delta valley into account since LASTIP™ can only handle two conduction band valleys.

Even with these simplifications, our modeling is more realistic and physical than previous studies. Some theoretical works, like the study of Liu et al. [32] only studied the material parameters such as gain and loss. These works are important but too primitive to predict the performance of Ge lasers. The works in [25, 76] used simple rate equation models with lots of simplifications to calculate threshold current and slope efficiency. Such models were oversimplified and ignored lots of 2D features such as the carrier distribution, current leakage, light distribution, etc. Only the optical loss of Ge was considered, with the parasitic optical absorption in the metal contact ignored, which turned out to be an influencing factor as indicated in our modeling in Section 5. Although one 2D work was done in [84], it was based on an unrealistic structure that was difficult to fabricate, and the modeling was not calibrated with experimental data. Compared to these studies, our modeling is a great improvement.

Chapter 5: Structure and Strain Optimizations

To take the full advantage from the stressors and further improve the device performance, we optimized the Ge cavity and the cladding geometry. We optimized W, d_{Ge}, and d_{poly}, which stand for the Ge cavity width, thickness, and the polysilicon cladding layer thickness respectively. The Ge cavity length was set to be unchanged at 270 μm. Based on Xiyue Li et al.'s study [26], geometry can greatly improve the efficiency. With the presence of SiN stressors, changing geometry also changes the strain field in the cavity and as a result influence the laser performance. Due to the limitations discussed in Section 4.7, in our optimization, we assume that the only geometry dependent material parameter is the strain.

In our optimization process, the goal is not to find the "true" optimal point, but rather to show that Ge lasers can be improved significantly. The reasons for that are twofold. 1) Ge is not a well-studied optical material, and many simplifications are assumed in our modeling as discussed in Section 4.7. Therefore, it is still too early to find the "true" optimum at this point. 2) Optimizing one variable at a time is more doable, as the rate equations are well established, and one can check the correctness of the results conveniently.

We changed one parameter at a time and kept others constant. Optimizations were performed on three structures, and we will use structure 2 as a detailed example to illustrate the optimization process. Several parameters are used for the characterization of laser performance. These parameters include: Slope efficiency η_d, internal efficiency η_i, extraction efficiency η_{ext}, Threshold current I_{th}, max wall-plug efficiency η_{wp}, confinement factor, internal loss, etc. For lasers, small I_{th} and large η_{wp} are both desired, but they may not be met at the same time. We chose maximum wall-plug efficiency η_{wp} as the most important optimization criteria because it represents the energy conversion efficiency of the device.

5.1 Optimizations of structure 1 without stressors

For Structure 1, without the stressors, the I_{th} and η_{wp}' s dependence on W, d_{Ge}, and d_{poly} are shown in Figure 5-1 and Figure 5-2. Details will be discussed in Section 5.2. d_{poly} had the largest impact and was first optimized as in Figure 5-1. I_{th} decreases from 810 to 57 mA and η_{wp} increases from 2.07% to 20.8% when d_{poly} changes from 0.2 to over 0.8. We chose d_{poly} = 0.8 μm as the optimized d_{poly}. For the W dependence, I_{th} increases linearly with W, but η_{wp} does not change much with W (Figure 5-2 (a)). Therefore, we chose W = 0.5 μm as the optimized W for less I_{th}. For the d_{Ge} dependence, the increase of η_{wp} resulted from the better optical confinement cannot compete with the increase of I_{th}. As a result, the η_{wp} only increase from 18.5% to 23.5% and then decrease (Figure 5-2 (b)). We chose the peak point d_{Ge} =0.5 μm as the optimization point for d_{Ge} dependence. The highest efficiency reached is 23.5% with d_{poly} = 0.8 μm, W = 0.5 μm， d_{Ge} = 0.5 μm, and I_{th} = 63 mA.

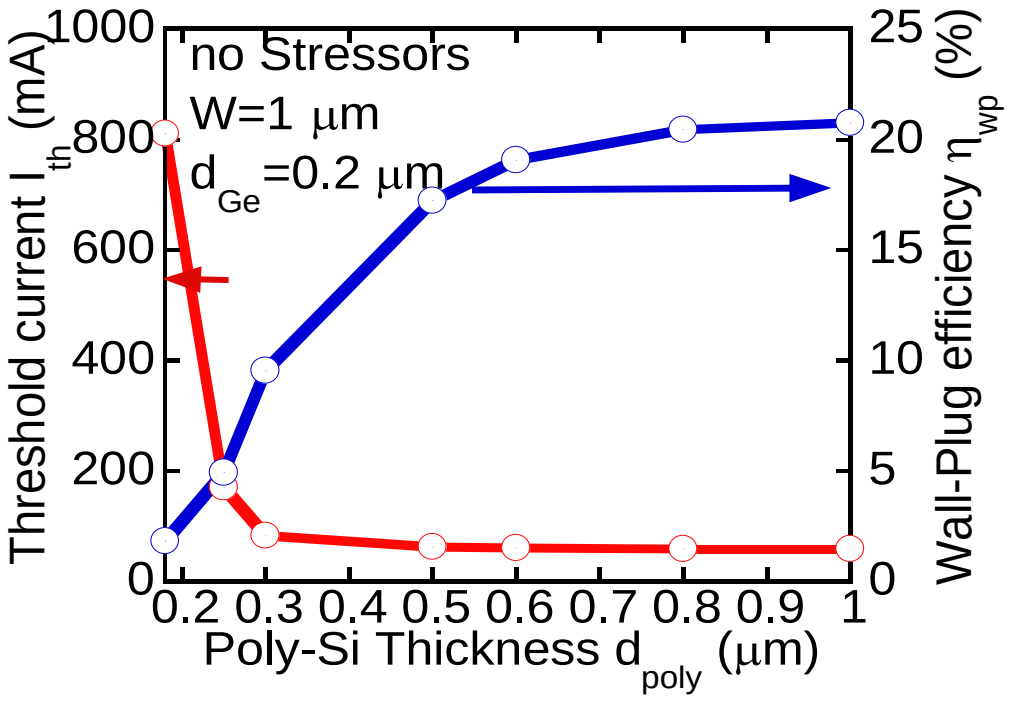

Figure 5-1 I_{th} and η_{wp} of Structure 1, d_{poly} dependence.

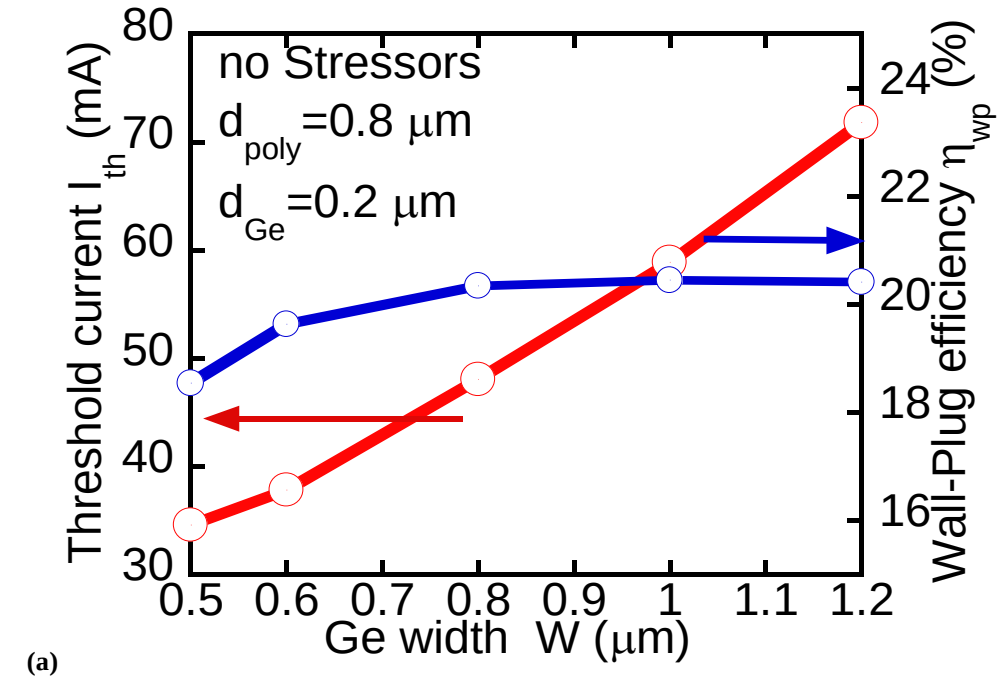

(a)

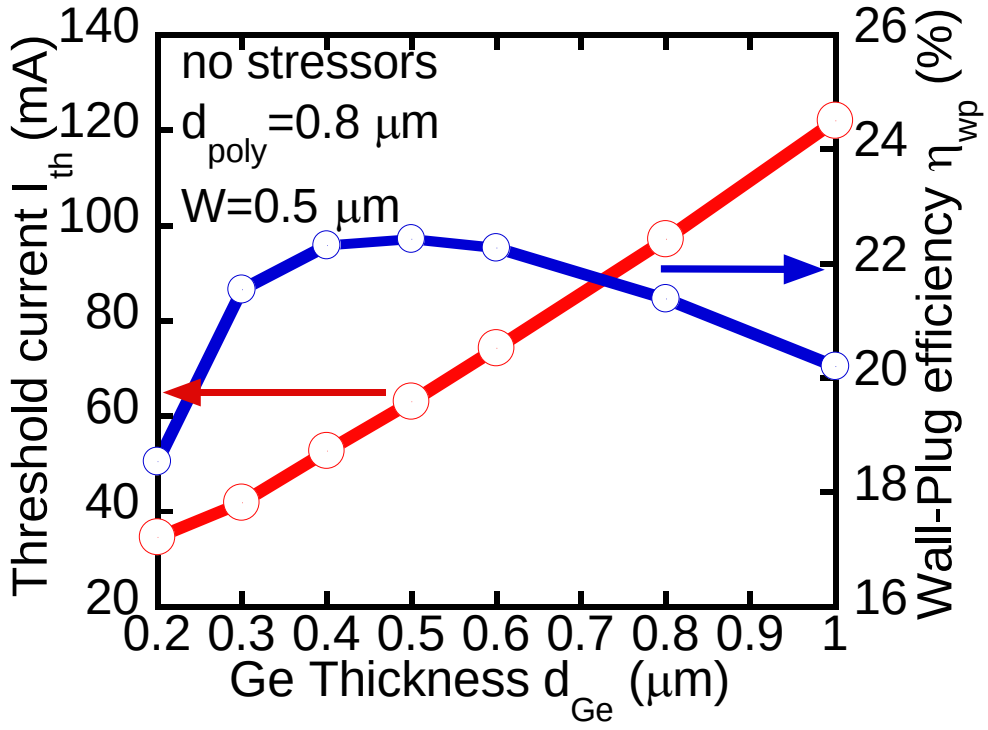

(b)

Figure 5-2 I_{th} and η_{wp} of Structure 1 (a) width dependence; (b) d_{Ge} dependence.

5.2 Optimizations of structure 2 with side stressors only

5.2.1 Polysilicon thickness (d_{poly}) optimization

The results of polysilicon thickness dependence are shown in Figure 5-3. The polysilicon thickness d_{poly} has the most dominant effect in the geometry optimization. As d_{poly} increased, we observed a dramatic increase in η_{wp} and a decrease in I_{th} (Figure 5-3 (b)). This is because that the light absorption caused by the metal contact is greatly reduced. Since the difference in refractive index between germanium and polysilicon is small, the vertical optical confinement is poor. Therefore, when the polysilicon coating is thin, a considerable proportion of light will easily enter the metal contact area, resulting in serious light absorption. As the top metal contact moved further away from the Ge cavity with the increase in d_{poly}, the occurrence of light leakage is reduced, and the internal loss $<\alpha_i>$ caused by the metal contact can be significantly reduced.

As a result, η_{ext} and thus η_d increase monotonically and reach a plateau at thick d_{poly} (Figure 5-3 (a)). I_{th} decreases as d_{poly} increases since less carrier density is needed to compensate for the loss. As a consequence, η_{wp} increases to 21.3% and plateaus after d_{poly} = 0.8 μm and I_{th} decreases to 54 mA (Figure 5-3 (b)). We chose 0.8 μm as the optimization point since η_{wp} plateaued after that point.

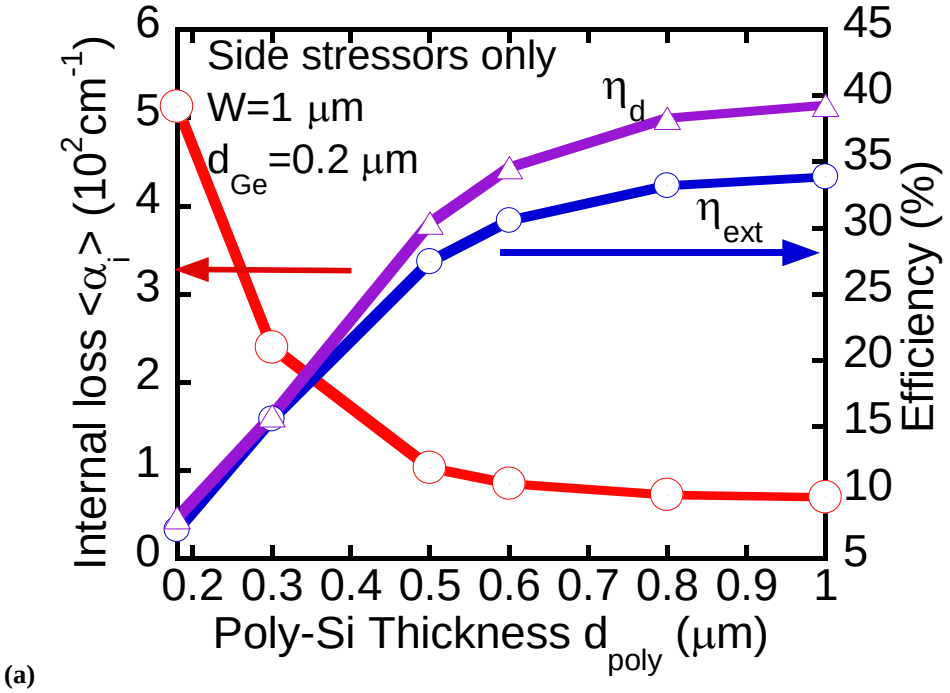

(a)

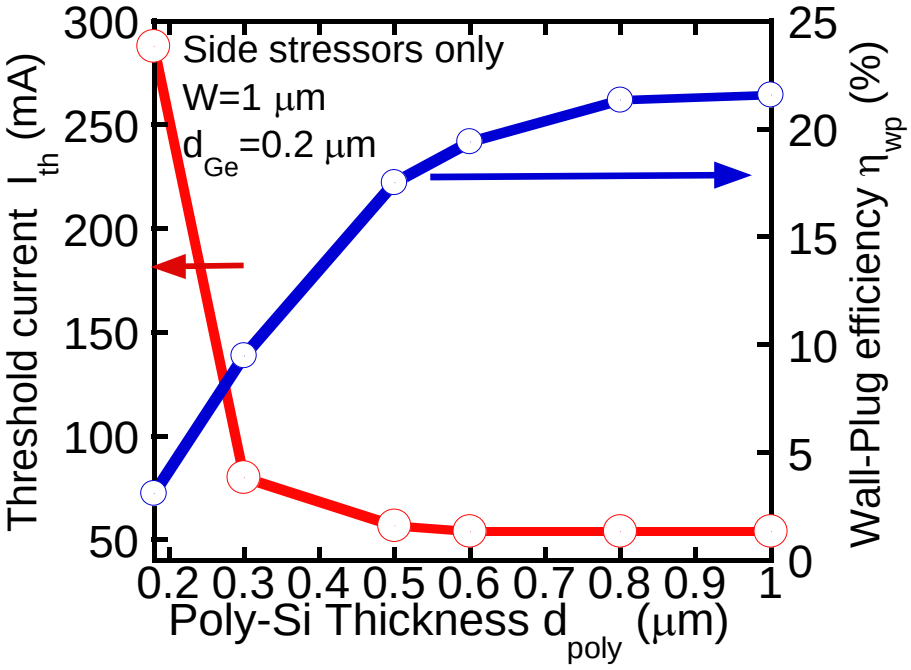

(b)

Figure 5-3 Polysilicon thickness d_{poly} dependence (W =1 μm, d_{Ge} = 0.2 μm) of (a) $\langle\alpha_i\rangle$ and η_{ext} ,η_d (b) I_{th} and η_{wp}.

5.2.2 Ge Width (W) optimizations

The cavity width (W) dependence is shown in Figure 5-4 and Figure 5-5 . η_{wp} only increases slightly and I_{th} increases linearly with W.

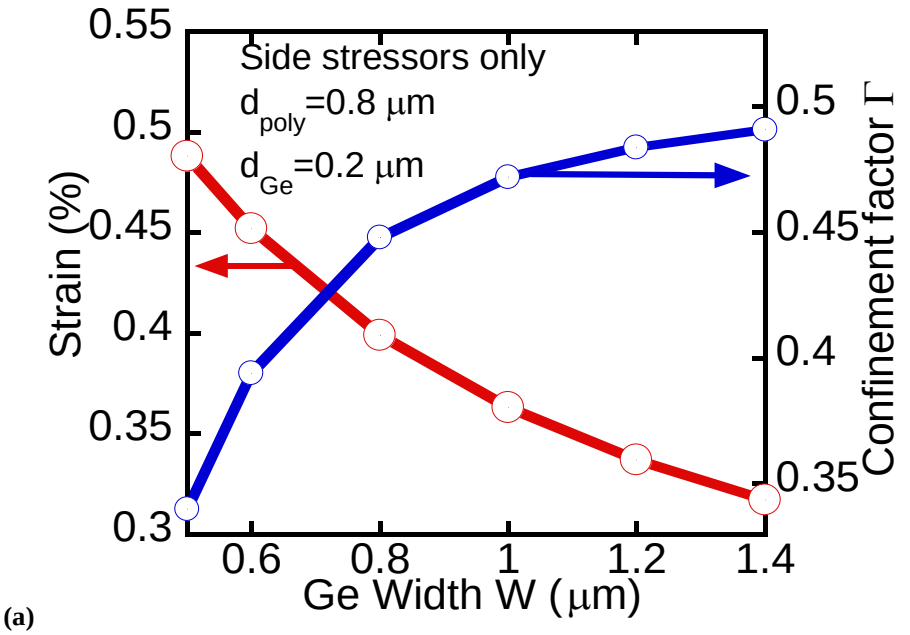

(a)

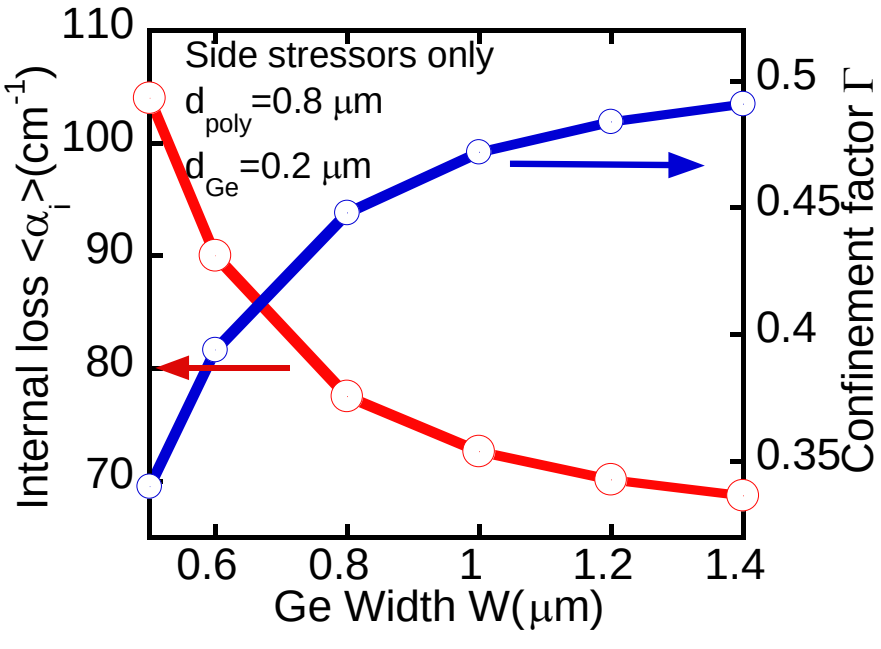

(b)

Figure 5-4 Ge width W dependence (d_{poly} =0.8 μm, d_{Ge} = 0.2 μm) of (a) strain ε_{eb} and Γ (b) $<\alpha_i>$ and Γ.

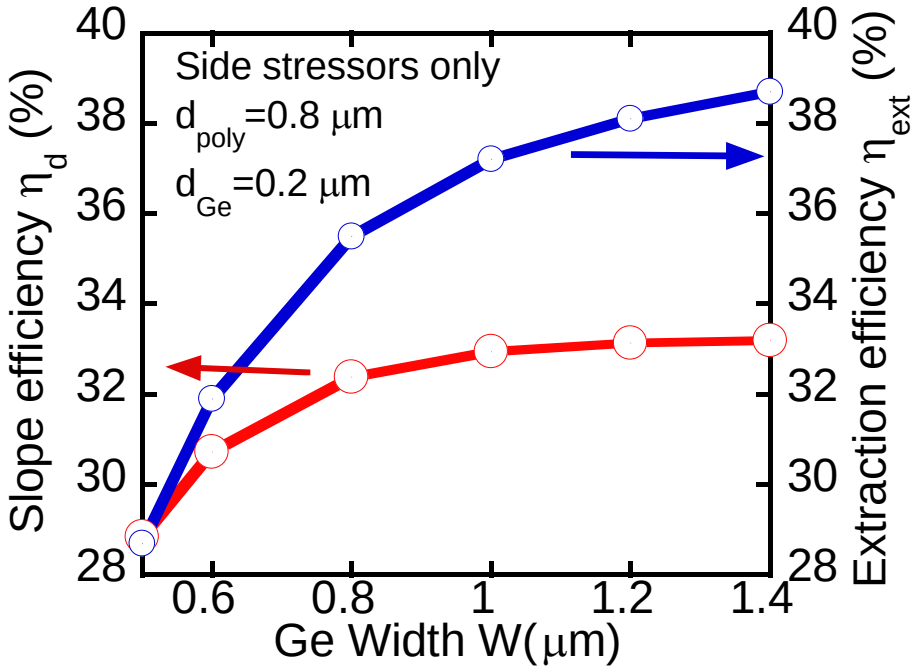

(a)

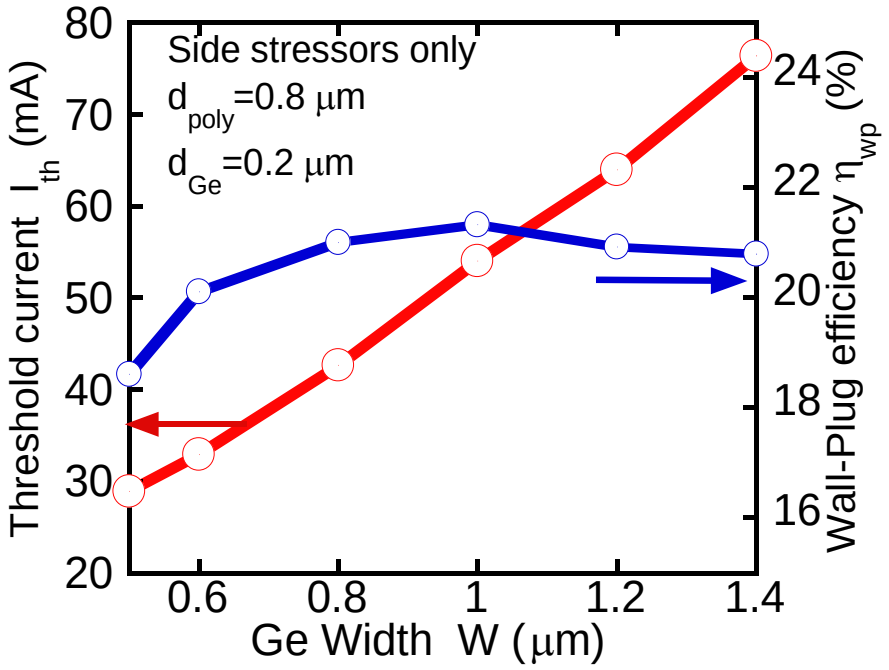

(b)

Figure 5-5 Ge width W dependence (d_{poly} =0.8 μm, d_{Ge} = 0.2 μm) of (a) η_d and η_{ext} (b) I_{th} and η_{wp}.

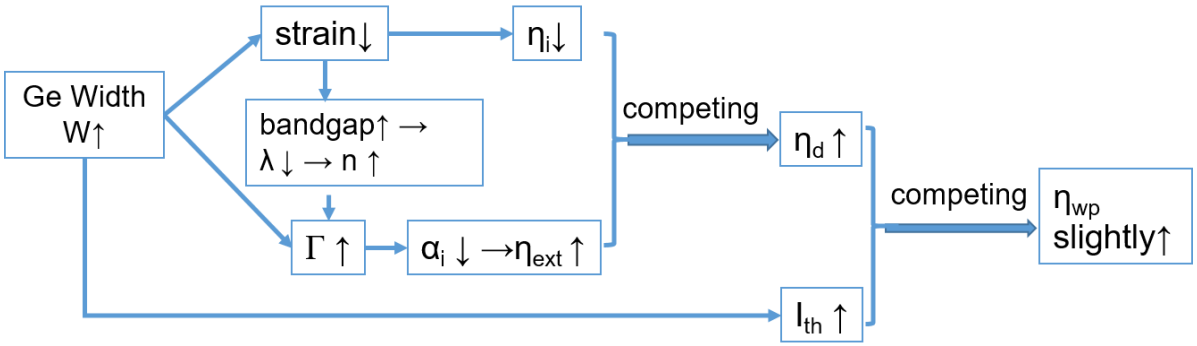

Figure 5-6 Impacts of Ge width (W) on other parameters.

The cavity width W and thickness d_{Ge} dependence come from three different effects: 1) strain introduction, 2) optical confinement factor Γ and 3) active region volume. The relationship between different parameters is shown in Figure 5-6. The tensile strain decreases with the increase of W because side stressors move away from the centre (Figure 5-4 (a)). The separation between the direct and indirect band gap increases accordingly, which results in a reduction in η_i. The decrease in strain raises the band gap, causing the lasing wavelength to become smaller. The reduced lasing wavelength causes a slight increase in the refractive index and thus increases Γ. As the cavity becomes wider, the lateral confinement becomes better, which also increases Γ (Figure 5-4 (a)). The FCA loss of polysilicon is greater than Ge. Therefore, a bigger Γ means less light travels in the lossy polysilicon region, which results in the decrease of $<\alpha_i>$ (Figure 5-4 (b)) and the increase of η_{ext} and thus the growth of η_d (Figure 5-5 (a)). I_{th} is a combination effect of n_{th}, η_i, and geometry as indicated in Eq. (3-7), but mostly dominated by geometry since I_{th} increases almost linearly with W in Figure 5-5 (b). The wider the W is, the larger current is needed to compensate the carrier loss resulted mainly from R_{srh} and R_{Aug}.

The increase of η_d would increase η_{wp} whereas increased I_{th} would decrease η_{wp}. Because of this competing effect, η_{wp} only increases slightly with W, as shown in Figure 5-5 (b). Further simulations show that choosing the maximum η_{wp} point where W = 1 μm does not promise better

performance in d dependence since a narrower waveguide is desired for side stressors. On the contrary, a wider cavity increases I_{th} greatly. Therefore, we chose W = 0.5 μm as the optimization point, where η_{wp} = 18.61% now but promotes the potential for higher efficiency. We choose W = 0.5 μm as the minimum value for optimization because when W is too small, optical confinement in the horizontal direction becomes poor, which is not suitable for the laser and causes convergence problems in the simulation.

5.2.3 Ge thickness d_{Ge} optimization

The cavity thickness (d_{Ge}) dependence is shown in Figure 5-7 to Figure 4-10. η_{wp} increases a lot and I_{th} increases monotonously with d_{Ge}.

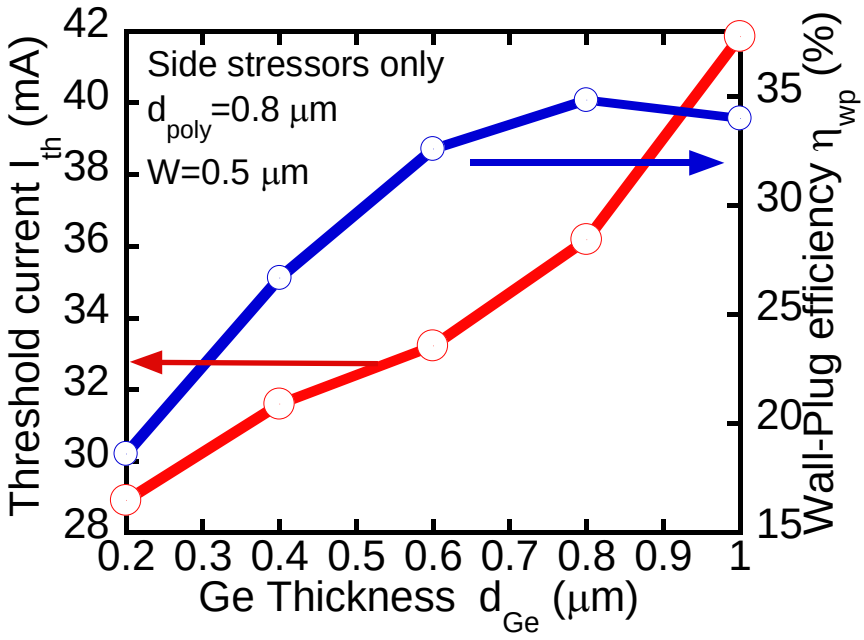

Figure 5-7 Ge thickness d_{Ge} dependence (W =0.5 μm, d_{poly} = 0.8 μm) of I_{th} and η_{wp}.

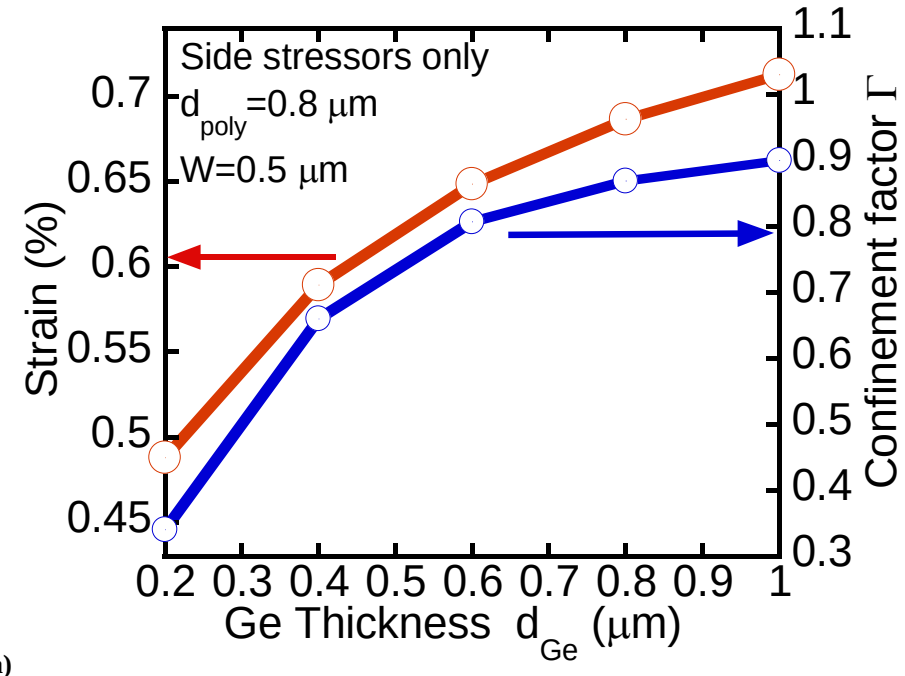

(a)

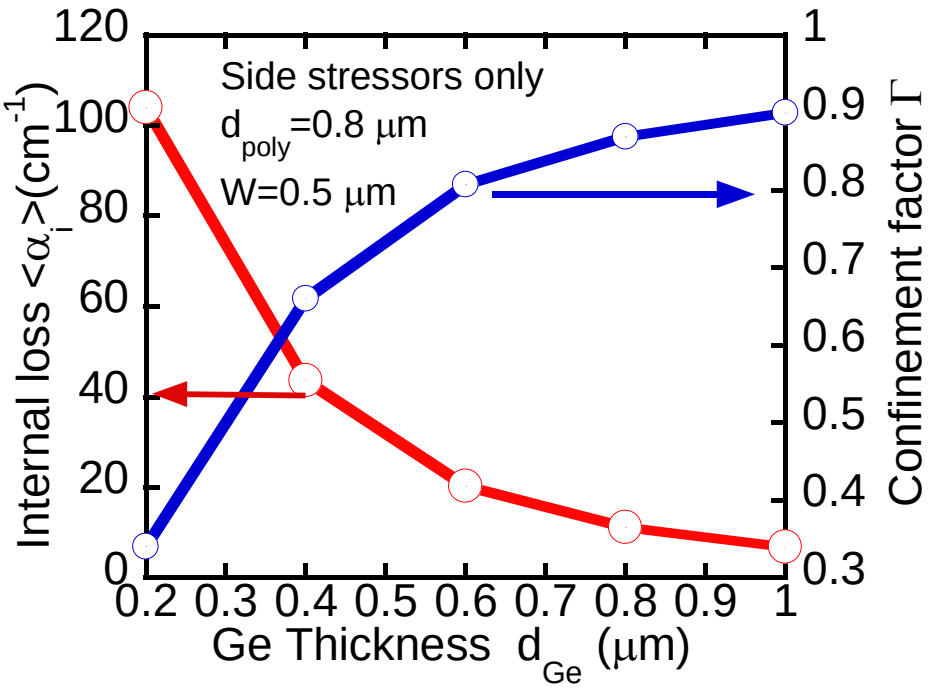

(b)

Figure 5-8 Ge thickness d_{Ge} dependence (W =0.5 μm, d_{poly} = 0.8 μm) of (a) Strain ε_{eb} and Γ (b) $<\alpha_i>$ and Γ.

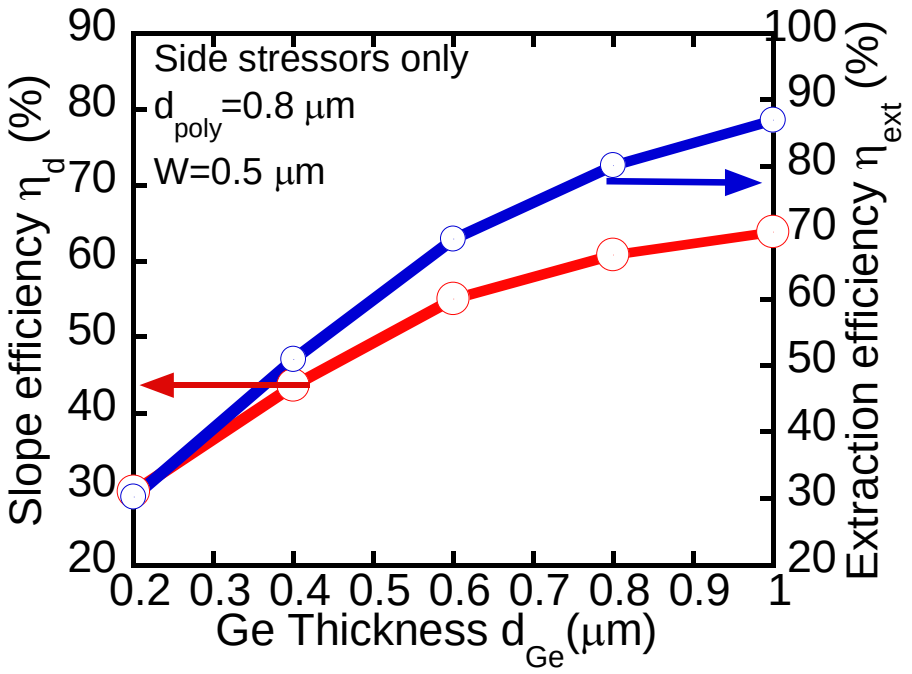

Figure 5-9 Ge thickness d_{Ge} dependence (W =0.5 μm, d_{poly} = 0.8 μm) of η_d and η_{ext}.

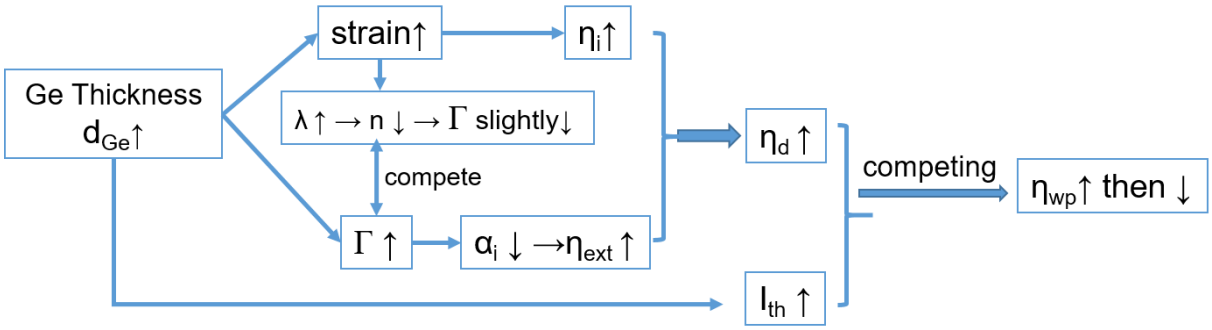

Figure 5-10 Impacts of Ge thickness d_{Ge} on other parameters.

The dependence of d_{Ge} is similar as W's dependence, which is shown in Figure 5-10. Strain ε_{eb} increases with d_{Ge} because more stressors react on the Ge cavity (Figure 5-8 (a)). The increase in the strain also caused a slight decrease in Γ as discussed before. Γ increases with d_{Ge} since thicker cavity promote better vertical confinement (Figure 5-8 (a)). The Γ shrinkage due to the change of lasing wavelength is only a minor effect for Γ. The increase in Γ causes the $<\alpha_i>$ to shrink (Figure 5-8 (b)) and thus increases the η_{ext} (Figure 5-9). As a result, η_d increases a lot since η_i and η_{ext} are of the same trend (Figure 5-9). Same as the W dependence, I_{th} increases almost linearly

with d_{Ge} (Figure 5-7). As the competing effect of I_{th} and η_d, η_{wp} peaks at 34.8% and then decreases (Figure 5-7). We chose d_{Ge} = 0.8 μm as the optimization point.

5.2.4 Strain's Impact

If we make the stress in SiN stressors to be 0, the only difference between the structures with and without the stress of stressors is the strain inside the Ge cavity. As a result, by comparing the same structure in d_{Ge} dependence with and without the stress of stressors, we can see how strain influences the laser performance. For the structure with the stress of stressors, the strain inside Ge cavity increases monotonously with the increase in d_{Ge} as shown in Figure 5-11(a) while the strain keeps unchanged at 0.25% in the structure without the stress of stressors. The increased strain decreases the difference between n gamma (direct) and L (indirect) conduction band (not shown here), decreases the band gap and increases the separation between lh and hh band (Figure 5-11(b)). These changes in the band make the direct recombination easier, and as a result, increase the material gain (Figure 5-12(a)). With tensile strain engineering and high doping, a material gain over 2000 cm^{-1} can be achieved, which is quite close to the typical material gain value of III-V materials around 5000 cm^{-1} at lasing condition. In Figure 5-12 (a), we can observe that as the strain increase, the peaks of the gain have a red shift because of the shrinkage of the band gap. As the strain increase, a second peak, which results from the split of lh and hh valence band occurs. The increase in gain decreases the carrier density needed for lasing and thus reduce I_{th} (Figure 5-12(b)). I_{th} decreases to about one-third with the stress of stressors, compared to that of the one without the stress of stressors. The increased lasing wavelength (Figure 5-11 (a)) decreases Γ by the changed real index n and decreases η_{ext} as discussed before (Figure 5-13 (a)). The η_d increases while η_{ext}

decreases by the decreased Γ, which shows that the η_i increases with the strain for the same geometry (Figure 5-13 (b)).

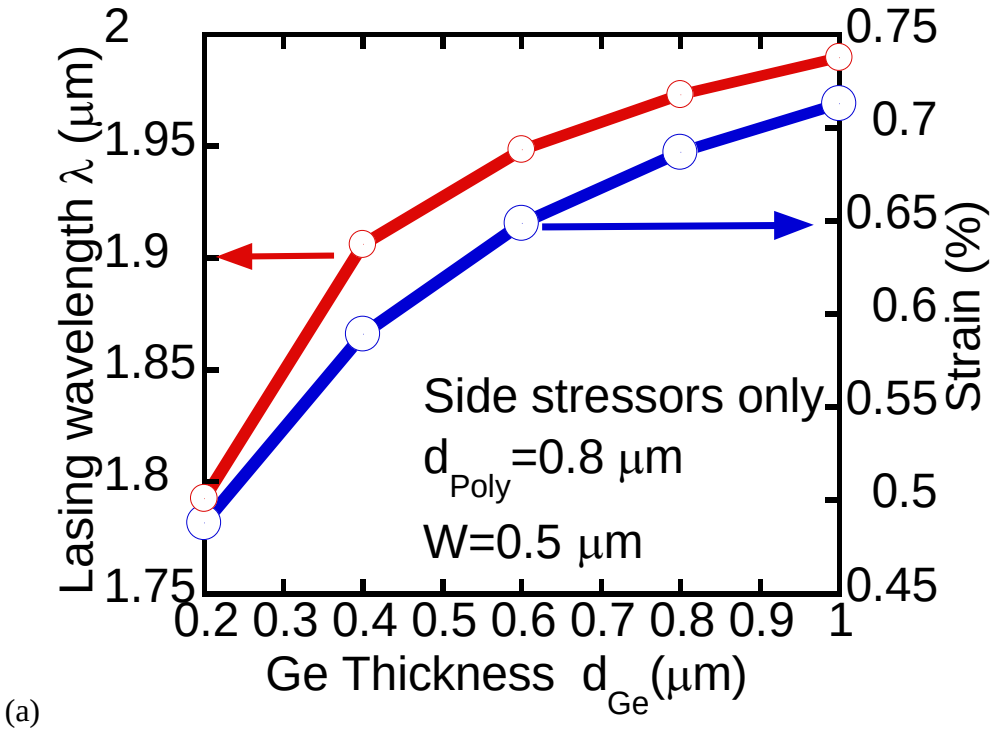

(a)

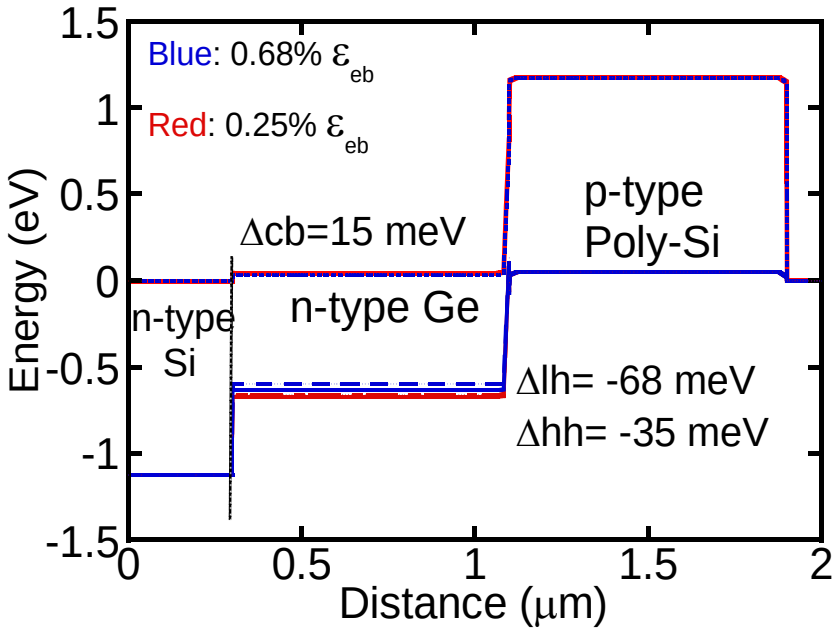

(b)

Figure 5-11 (a) Strain ε_{eb} and λ with different d_{Ge} (W=0.5μm, d_{poly} = 0.8μm): (b) direct band alignment under different strain at thermal equilibrium (V=0, d_{Ge}=0.8 μm).

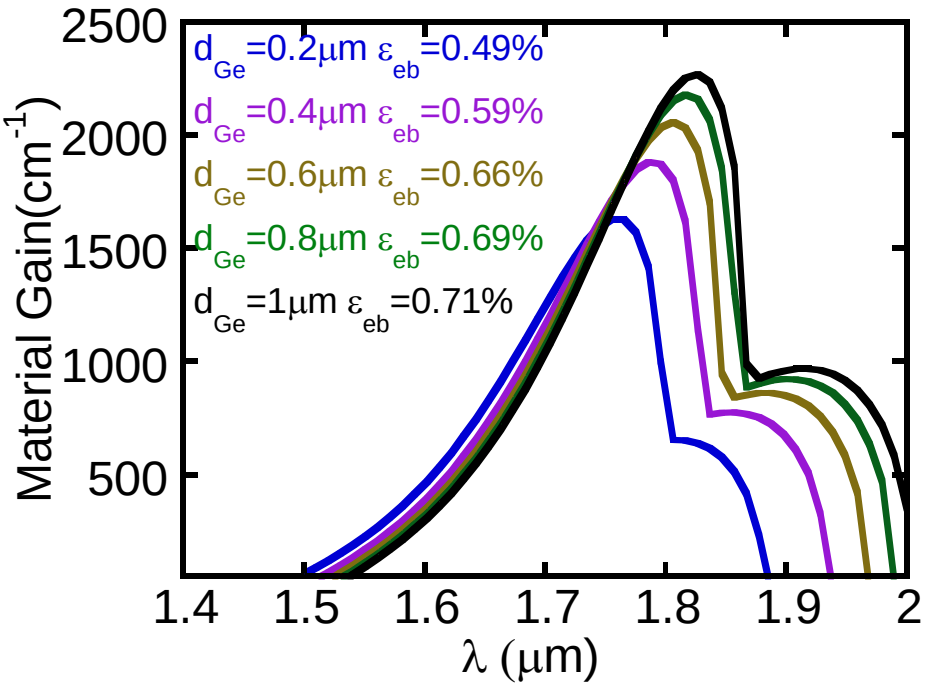

(a)

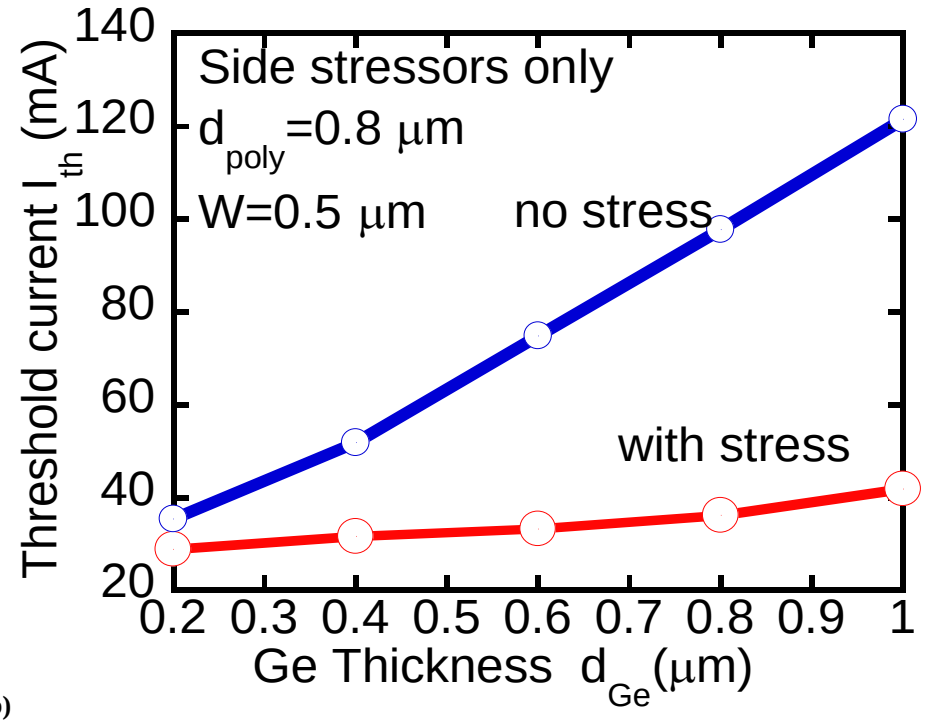

(b)

Figure 5-12 Strain impact with different d_{Ge} (W=0.5μm, d_{poly} = 0.8μm): (a) material gain at different strain with carrier concentration n=p=4×10^{19}cm^{-3}, (b) I_{th}, and (f) η_d.

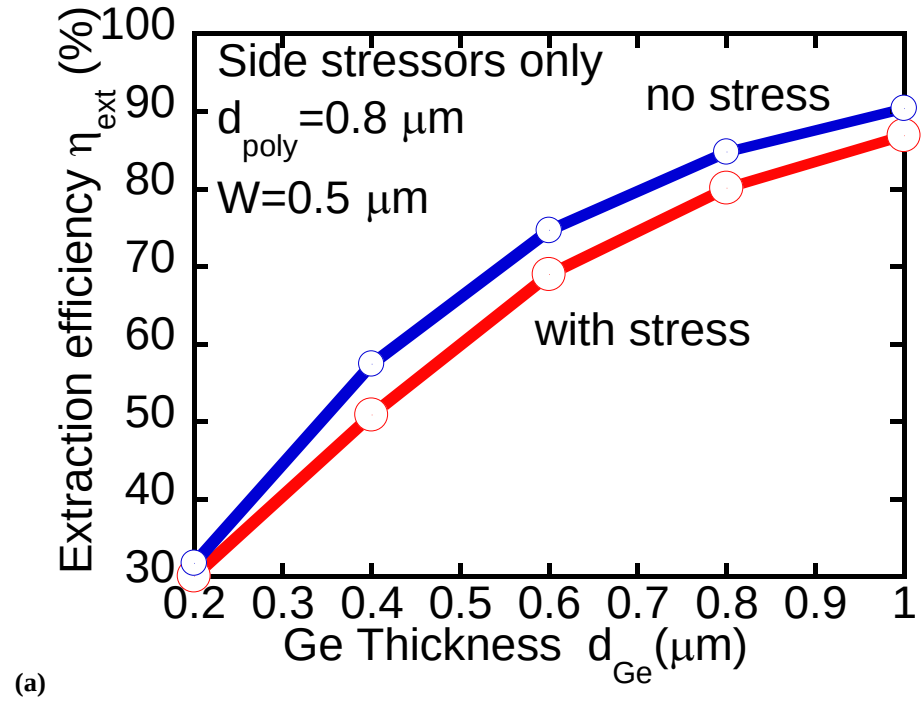

(a)

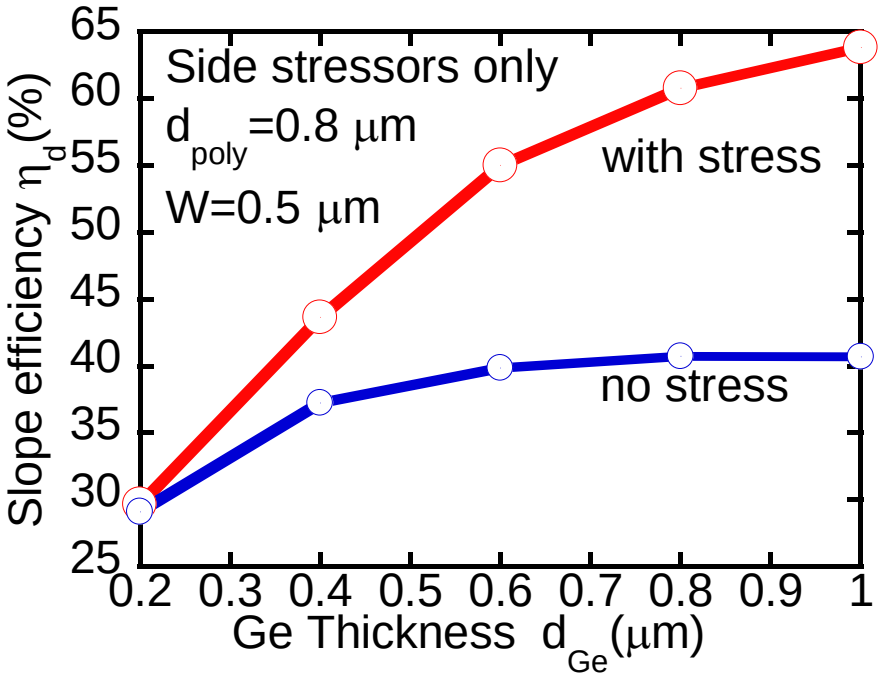

(b)

Figure 5-13 Strain impact with different d_{Ge} (W=0.5μm, d_{poly} = 0.8μm): (a) η_{ext} (b) η_d.

5.3 Optimizations of structure 3 with top and side stressors

A large W and small d_{Ge} are desired for the strain introduction from the top stressor, which is undesired for the side stressors. Therefore, W and d_{Ge} are optimized together to obtain a high η_{wp}. W = 0.5 μm is not the optimized width in Figure 5-14 (a), but by comparing a few different W values, W = 0.5 μm has the potential to produce a higher η_{wp}. d_{Ge} = 1 μm is the optimization point of d_{Ge} dependence for W = 0.5 μm. For such structures, the strain introduction from side stressors is more prominent than the top stressor. The strain introduction from top stressor is not obvious because top stressor can only introduce strain on the top of the Ge cavity whereas side stressors can introduce strain in the whole cavity by decreasing the cavity width.

d_{poly} has similar but weaker impact compared to structure 2. Due to the presence of the top stressor, the top metal contact loss is greatly reduced for Structure 3 before increasing d_{poly}. However, the increasing d_{poly} would further increase η_{wp} and decrease I_{th}, which shows that top stressor can only diminish the optical loss caused by metal to a certain extent. Increasing d_{poly} is a more efficient way to reduce the optical loss caused by the metal.

The final optimization is: d_{poly} = 0.4 μm, W = 0.5 μm, d_{Ge} = 1 μm, with η_{wp} peaks at 25.4% and an I_{th} of 44 mA.

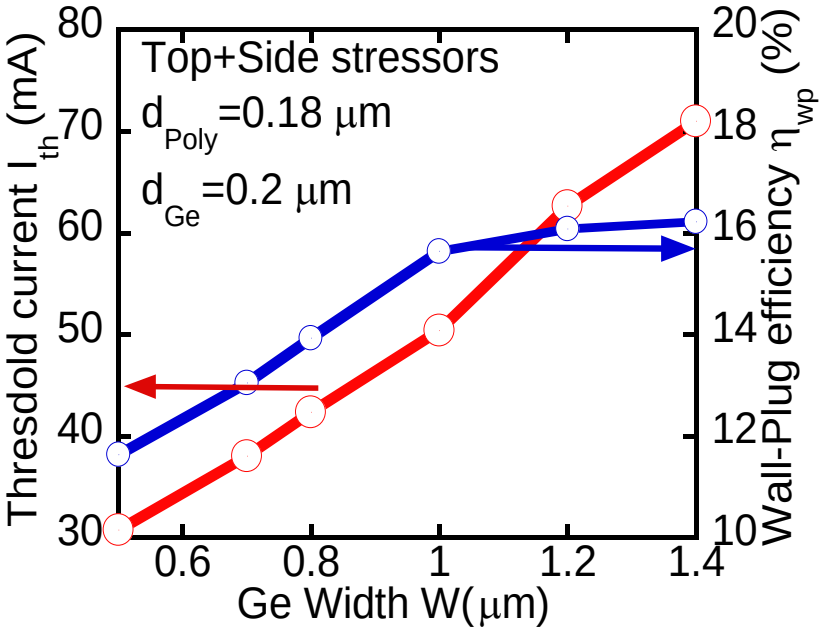

(a)

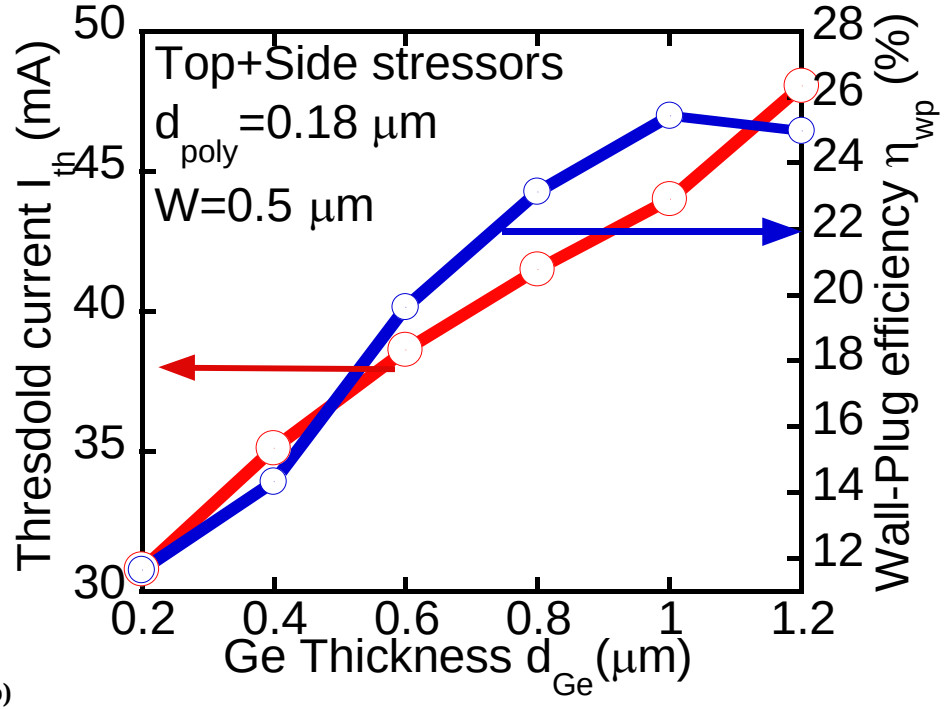

(b)

Figure 5-14 I_{th} and η_{wp} of Structure 3 (a) width dependence (b) d_{Ge} dependence.

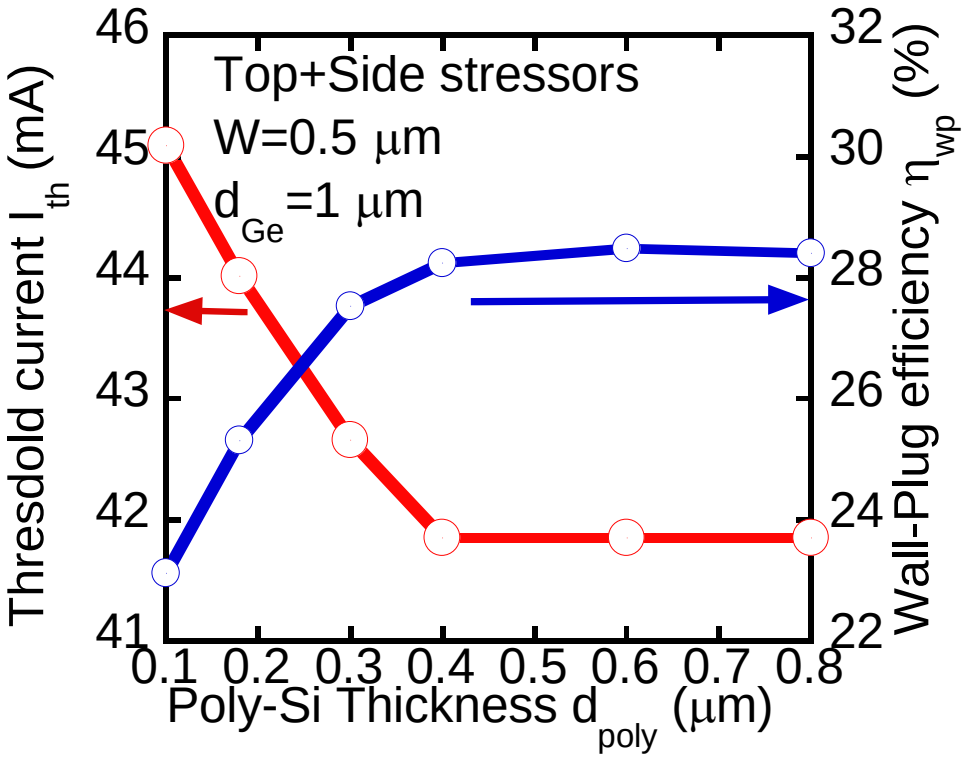

Figure 5-15 I_{th} and η_{wp} of Structure 3, d_{poly} dependence.

5.4 Comparisons of the structures

The comparisons of the three structures after optimization are shown in Figure 5-16 and Table 5-1. We can observe that changing geometry could significantly increase η_{wp} and decrease I_{th}. Adding stressors can further improve these two parameters. By using side stressors only, the highest η_{wp} rose to 34.8%, but adding top stressor does not provide greater η_{wp}. This is mainly because that the top stressor increases the series resistance significantly. From the current density in Figure 5-17 and Figure 5-18, we can see that the top SiN stressor prevents the current from directly flowing through the cavity. Structure 1 and 2 have a series resistance around 0.4 Ω, but it is around 0.9 Ω for Structure 3, which means Structure 3 requires higher voltage and thus higher electric power. Plus, the strain introduced by top stressor is marginal compared to side stressors as discussed in Section 5.3. As a result, Structure 3 does not produce a higher η_{wp} than

Structure 2. Therefore, considering both η_{wp} and I_{th}, Structure 2, with side stressors only, is recommended.

For cavity length dependence, we observe a linear relationship between I_{th} and length L as in Eq. (3-7). As a result, the η_{wp} increases as the L decreases because of the decline in I_{th}. A smaller cavity is desired to have low I_{th} and η_{wp} but might be limited by experimental problems like poor heat dissipation.

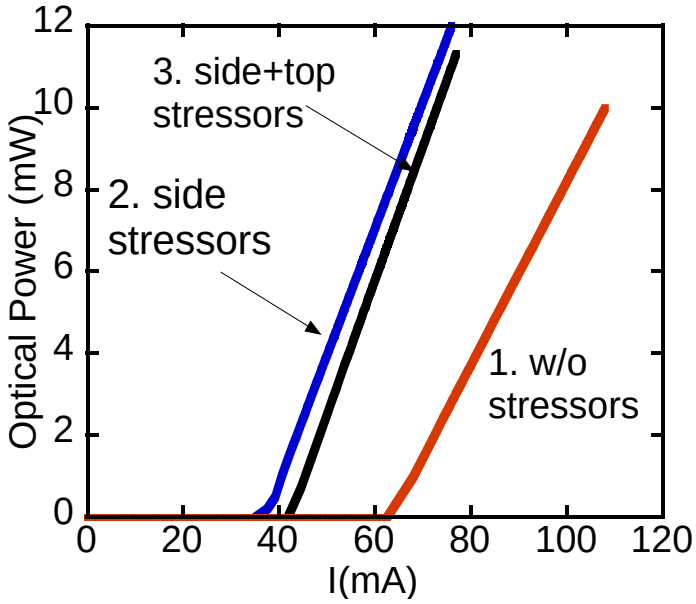

Figure 5-16 L-I curve for three structures after optimization.

Table 5-1 Laser performance of the 3 structures in Figure 5-16 after structure optimizations.

Structure	1	2	3
ε_{eb} (%)	0.25	0.713	0.714
I_{th} (mA)	63	36	42
J_{th} (kA/cm^2)	47	27	31
η_d (%)	38.6	60.8	61.9
highest η_{wp} (%)	23.5	34.8	28.3
Current required for highest η_{wp}(mA)	494	270	210
Output power at highest η_{wp} (mW)	100	72	55

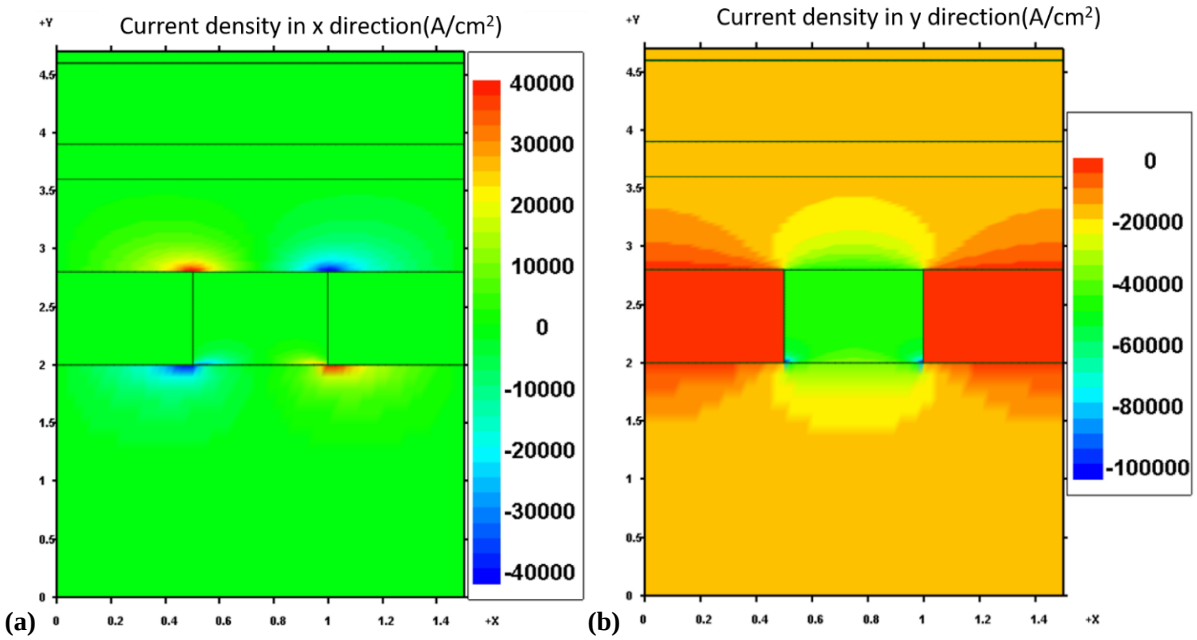

Figure 5-17 Current density field of structure 2 (a) in x direcdtion; (b) in y direction at 60 mA inject level.

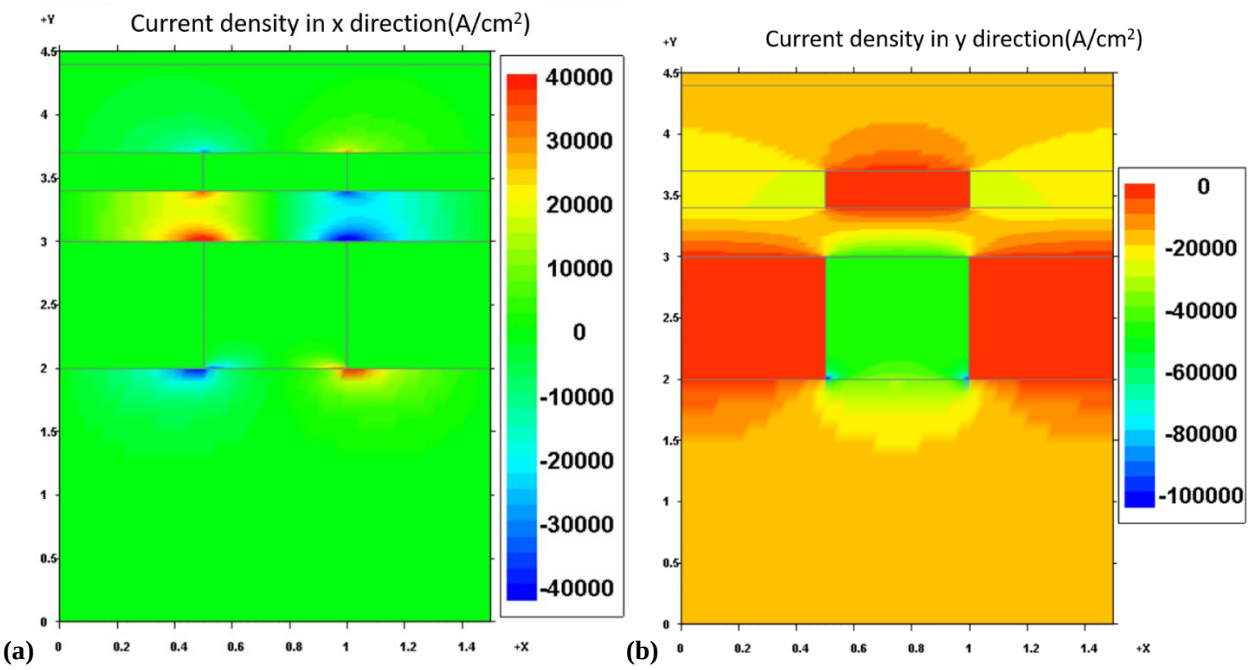

Figure 5-18 Current density field of structure 3 (a) in x direcdtion; (b) in y direction at 60 mA inject level.

5.5 Effect of defect-limited minority carrier lifetime on the performance

For the study above, the defect-limited minority carrier lifetime $\tau_{p,n}$ is set as 1 ns for conservative prediction. From Figure 5-19, we can see that by increasing the $\tau_{p,n}$, which means improving the material quality, the performance of laser improves greatly. When we have a better material quality, the carrier loss due to the SRH recombination is reduced, and as a result, the I_{th} decreases and η_{wp} increases. When the $\tau_{p,n}$ increase beyond 10ns, the reduction of SRH recombination rate has reached its limit and Auger recombination becomes the dominant carrier loss mechanism. Therefore, the decrease of I_{th} and the increase of η_{wp} reach their limit.

Technically, it is feasible to obtain Ge layers with better quality and longer carrier lifetime by approaches like Ge growth on a GOI (Germanium On Insulator) substrate [77] or direct wafer bonding and chemical mechanical polishing (CMP) [78]. Carrier lifetimes of 5.3 and 3.12 ns have been achieved respectively by the above approaches [77, 78] and a 10 ns $\tau_{p,n}$ is not too far away. Figure 5-20 shows the performance of the 3 structures with $\tau_{p,n} = 10\ ns$. I_{th} decreases about 5-10 times and η_{wp} increases by 10% when $\tau_{p,n}$ increases from 1 ns to 10 ns. .

Therefore, if a better material quality, along with the geometry and stress engineering, Ge laser performance will not be too far off from III-V laser performance in the range of I_{th} <50 mA and η_{wp} about 10-60%.

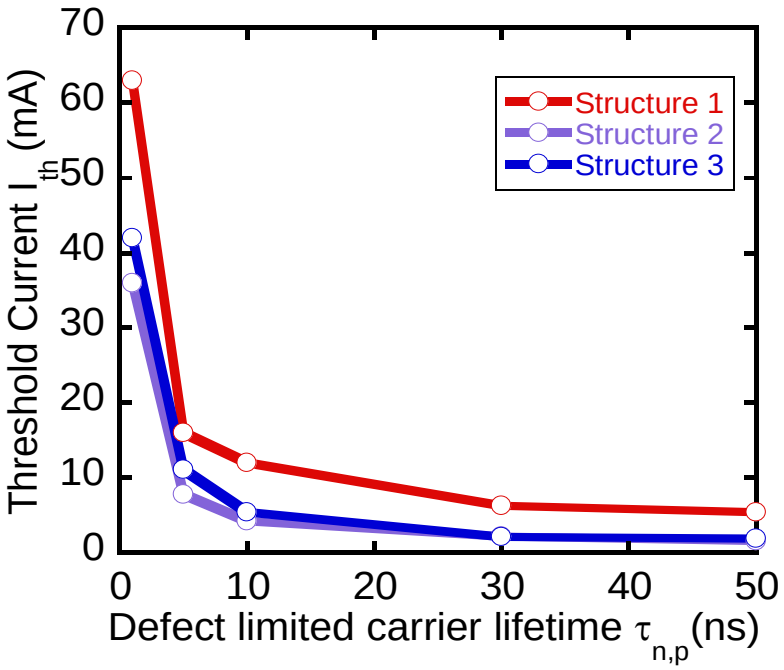

(a)

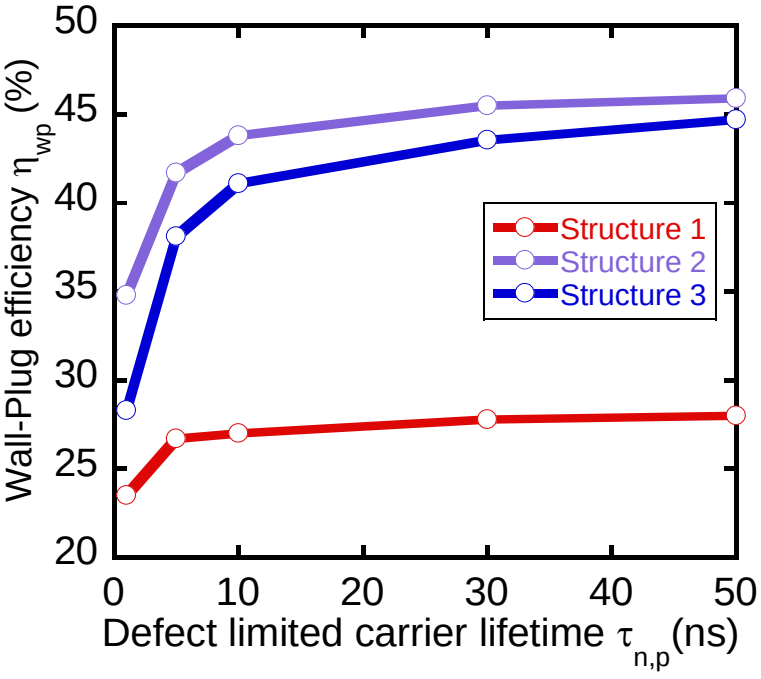

(b)

Figure 5-19 Defect limited carrier lifetime dependence of I_{th} and η_{wp}.

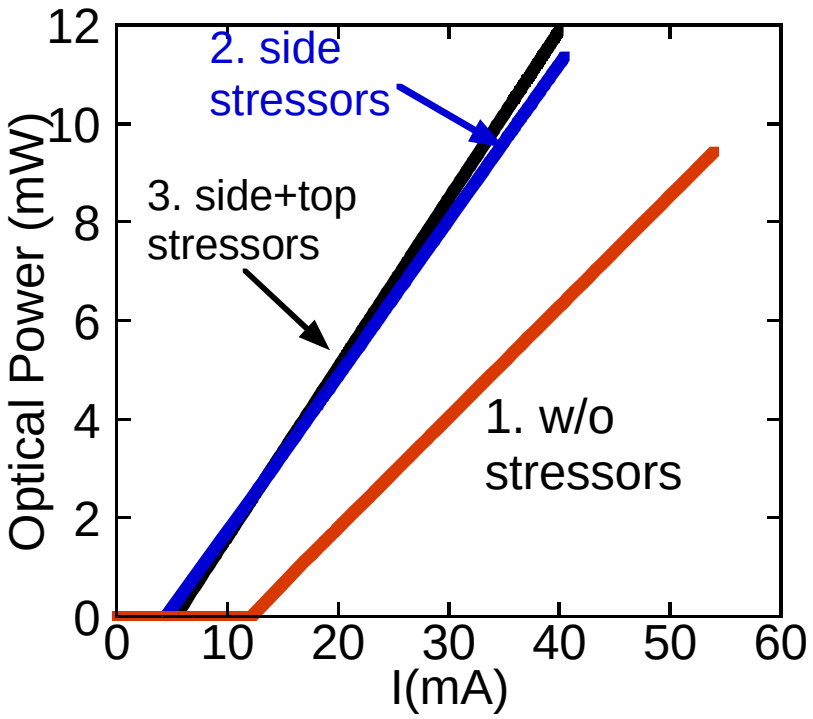

Figure 5-20 . L-I curve for three structures with $\tau_{p,n}$ = 10 ns.

Table 5-2 Laser performance of the three structures in Figure 5-20.

Structure	1	2	3
ε_{eb} (%)	0.25	0.713	0.714
I_{th} (mA)	12	4	5
J_{th} (kA/cm^2)	8.8	3.0	3.7
η_d (%)	38.7	62.3	64.8
highest achievable η_{wp} (%)	27.0	43.8	41.1
Current required for highest η_{wp} (mA)	167	81	55
Output power at highest η_{wp} (mW)	35	24	17

Chapter 6: Thesis Summary and Suggestions for Future Work

As an indispensable part in the optical interconnects, it cannot be denied that a silicon-compatible laser is the holy grail in the silicon photonics. Ge is the most compatible material with Si processing and has great potentials in the silicon-based electronics-photonic integrated circuits. Compared to III-V lasers on Si substrates, Ge-on-Si lasers can be processed in Si fabs with a much lower cost and much short development time to mass production. A major problem with Ge lasers is that the performance of initially demonstrated lasers were quite poor, and available stress engineering methods are not suitable for laser structure designs.

In this work, two novel Ge laser structures with SiN stressors were proposed, modeled and optimized. SiN stressors were shown to be effective in reducing I_{th} and improving η_{wp}. Side stressors turned out to be a more efficient way to increase η_{wp} than using the top and side stressors together. With the side stressors and geometry optimizations, a η_{wp} of 34.8% and an I_{th} of 36 mA (J_{th} of 27 kA/cm^2) can be achieved with a defect limited carrier lifetime ($\tau_{p,n}$) of 1 ns. With $\tau_{p,n} = 10\ ns$, an I_{th} of 4 mA (J_{th} of 3 kA/cm^2) and a η_{wp} of 43.8% can be achieved. These are tremendous improvements from the case without any stressors. These results give strong support to the Ge-on-Si laser technology and provide an effective way to improve the Ge laser performance.

However, to realize Ge lasers with reasonable performance, a lot more research efforts are needed both in crystal growth, processing, device design/fabrication and fundamental studies of Ge as an optical material. With a high tensile strain, Ge lasers can be used as infra-red lasers. Beyond making Ge lasers, for on-chip optical interconnects, many other aspects have to be addressed as well such as a photodiode suitable for receiving the wavelength from the Ge lasers and the integration scheme of optical devices and electronic devices on a wafer level.

Theoretically, a Ge photodiode with a higher tensile strain level has a smaller bandgap than a Ge laser with a lower tensile strain level and can serve as the desired photodetector. Again, stress engineering is the key.

Beyond Ge lasers, Ge can be used as an intermediate layer between InAs/GaAs lasers and Si to reduce crystal defects and thus lasing threshold. How to make Ge as a thin and effective transition layer between III-V lasers and Si, although it is not about Ge as a gain medium, is of great technical interests.

Nevertheless, the topic of integrating optical functions on Si-based ICs will keep being a very attractive and active research area, and we are looking forward to seeing more progress and breakthroughs in this field and in applications to our everyday life.

Bibliography

[1]. G.E. Moore, "Cramming more components onto integrated circuits". *Proceedings of the IEEE*. 86(1): p. 82-85. 1998

[2]. V. Moroz. "Transition from planar MOSFETs to FinFETs and its impact on design and variability". in *Proceedings of the Berkley Seminar*. 2011.

[3]. Y. Huo, et al., "Strained Ge and GeSn band engineering for Si photonic integrated circuits". 2010: Stanford University.

[4]. S.I. Association, "Semiconductor Industry Association (SIA) Roadmap". 1997

[5]. X. Sun, "Ge-on-Si light-emitting materials and devices for silicon photonics", Massachusetts Institute of Technology. 2009

[6]. M. Paniccia, M. Morse, and M. Salib, "Integrated photonics", in *Silicon Photonics*. 2004, Springer. p. 51-88.

[7]. D. Huang, et al., "Optical interconnects: out of the box forever?". *IEEE Journal of Selected Topics in Quantum Electronics*. 9(2): p. 614-623. 2003

[8]. M. Charbonneau-Lefort, et al. "Active optical cables for consumer applications". in *Optical Interconnects Conference, 2014 IEEE*. 2014. IEEE.

[9]. "http://tik.services/blog/". Online; accessed 2-June-2017

[10]. Z. Zhou, B. Yin, and J. Michel, "On-chip light sources for silicon photonics". *Light: Science & Applications*. 4(11): p. e358. 2015

[11]. Y. Cai, "Materials science and design for germanium monolithic light source on silicon", Massachusetts Institute of Technology. 2014

[12]. M.E. Groenert, et al., "Monolithic integration of room-temperature cw GaAs/AlGaAs lasers on Si substrates via relaxed graded GeSi buffer layers". *Journal of Applied Physics*. 93(1): p. 362-367. 2003

[13]. H. Rong, et al., "An all-silicon Raman laser". *Nature*. 433(7023): p. 292-294. 2005

[14]. N. Koshida and H. Koyama, "Visible electroluminescence from porous silicon". *Applied Physics Letters*. 60(3): p. 347-349. 1992

[15]. L. Pavesi, et al., "Optical gain in silicon nanocrystals". *Nature*. 408(6811): p. 440-444. 2000

[16]. A. Kenyon, "Erbium in silicon". *Semiconductor Science and Technology*. 20(12): p. R65. 2005

[17]. G. Franzò, et al., "Sensitizing properties of amorphous Si clusters on the 1.54-μm luminescence of Er in Si-rich SiO 2". *Applied Physics Letters*. 82(22): p. 3871-3873. 2003

[18]. S. Yerci, R. Li, and L. Dal Negro, "Electroluminescence from Er-doped Si-rich silicon nitride light emitting diodes". *Applied Physics Letters*. 97(8): p. 081109. 2010

[19]. M. Miritello, et al., "Efficient luminescence and energy transfer in erbium silicate thin films". *Advanced Materials*. 19(12): p. 1582-1588. 2007

[20]. H. Kataria, et al., "Simple epitaxial lateral overgrowth process as a strategy for photonic integration on silicon". *IEEE Journal Of Selected Topics In Quantum Electronics*. 20(4): p. 380-386. 2014

[21]. S. Chen, et al., "Electrically pumped continuous-wave III–V quantum dot lasers on silicon". *Nature Photonics*. 2016

[22]. J. Liu, et al., "Ge-on-Si laser operating at room temperature". *Optics letters*. 35(5): p. 679-681. 2010

[23]. R.E. Camacho-Aguilera, et al., "An electrically pumped germanium laser". *Optics express*. 20(10): p. 11316-11320. 2012
[24]. R. Koerner, et al., "Electrically pumped lasing from Ge Fabry-Perot resonators on Si". *Optics express*. 23(11): p. 14815-14822. 2015
[25]. B. Dutt, et al., "Roadmap to an efficient germanium-on-silicon laser: strain vs. n-type doping". *IEEE Photonics Journal*. 4(5): p. 2002-2009. 2012
[26]. X. Li, et al., "Design considerations of biaxially tensile-strained germanium-on-silicon lasers". *Semiconductor Science and Technology*. 31(6): p. 065015. 2016
[27]. A.K. Okyay, et al. "Ge on Si by novel heteroepitaxy for high efficiency near infrared photodetection". in *Lasers and Electro-Optics, 2006 and 2006 Quantum Electronics and Laser Science Conference. CLEO/QELS 2006. Conference on*. 2006. IEEE.
[28]. J.E. Roth, et al., "Optical modulator on silicon employing germanium quantum wells". *Optics Express*. 15(9): p. 5851-5859. 2007
[29]. D. Nam, "Strained Germanium Technology for On-chip Optical Interconnects", STANFORD UNIVERSITY. 2013
[30]. R.E. Camacho-Aguilera, "Ge-on-Si laser for silicon photonics", Citeseer. 2013
[31]. M.V. Fischetti and S.E. Laux, "Band structure, deformation potentials, and carrier mobility in strained Si, Ge, and SiGe alloys". *Journal of Applied Physics*. 80(4): p. 2234-2252. 1996
[32]. J. Liu, et al., "Tensile-strained, n-type Ge as a gain medium for monolithic laser integration on Si". *Optics Express*. 15(18): p. 11272-11277. 2007
[33]. J. Kouvetakis, J. Menendez, and A. Chizmeshya, "Tin-based group IV semiconductors: New platforms for opto-and microelectronics on silicon". *Annu. Rev. Mater. Res.* 36: p. 497-554. 2006
[34]. S. Wirths, et al., "Lasing in direct-bandgap GeSn alloy grown on Si". *Nature photonics*. 9(2): p. 88-92. 2015
[35]. M. Grydlik, Hackl, Florian, Groiss, Heiko, Glaser, Martin, Halilovic, Alma, Fromherz, Thomas, Jantsch, Wolfgang, Schäffler, Friedrich, Brehm, Moritz, "Lasing from Glassy Ge Quantum Dots in Crystalline Si". *ACS Photonics*. 3(2): p. pp 298–303. 2016/02/17
[36]. L. Ding, et al., "Dependences of photoluminescence from P-implanted epitaxial Ge". *Optics express*. 20(8): p. 8228-8239. 2012
[37]. M. Oehme, J. Werner, and E. Kasper, "Molecular beam epitaxy of highly antimony doped germanium on silicon". *Journal of Crystal Growth*. 310(21): p. 4531-4534. 2008
[38]. R.E. Camacho-Aguilera, et al., "High active carrier concentration in n-type, thin film Ge using delta-doping". *Optical Materials Express*. 2(11): p. 1462-1469. 2012
[39]. J. Liu, et al., "Silicidation-induced band gap shrinkage in Ge epitaxial films on Si". *Applied Physics Letters*. 84(5): p. 660-662. 2004
[40]. S. Pidin, et al. "A novel strain enhanced CMOS architecture using selectively deposited high tensile and high compressive silicon nitride films". in *Electron Devices Meeting, 2004. IEDM Technical Digest. IEEE International*. 2004. IEEE.
[41]. G. Capellini, et al., "Tensile Ge microstructures for lasing fabricated by means of a silicon complementary metal-oxide-semiconductor process". *Optics express*. 22(1): p. 399-410. 2014
[42]. J.R. Jain, et al., "A micromachining-based technology for enhancing germanium light emission via tensile strain". *Nature Photonics*. 6(6): p. 398-405. 2012
[43]. M. Süess, et al., "Analysis of enhanced light emission from highly strained germanium microbridges". *Nature Photonics*. 7(6): p. 466-472. 2013

[44]. D.S. Sukhdeo, et al., "Direct bandgap germanium-on-silicon inferred from 5.7%⟨ 100⟩ uniaxial tensile strain [Invited]". *Photonics Research*. 2(3): p. A8-A13. 2014
[45]. Y. Cai, et al., "Analysis of threshold current behavior for bulk and quantum-well germanium laser structures". *IEEE Journal of Selected Topics in Quantum Electronics*. 19(4): p. 1901009-1901009. 2013
[46]. A. Yariv and P. Yeh, "Photonics: optical electronics in modern communications". Vol. 6. 2007: oxford university press New York.
[47]. S.L. Chuang, "Physics of photonic devices". Vol. 80. 2012: John Wiley & Sons.
[48]. L.A. Coldren, S.W. Corzine, and M.L. Mashanovitch, "Diode lasers and photonic integrated circuits". Vol. 218. 2012: John Wiley & Sons.
[49]. J. Piprek, "Semiconductor optoelectronic devices: introduction to physics and simulation". 2013: Academic press.
[50]. R. Camacho-Aguilera. "Monolithically integrated Ge CMOS laser". in *SPIE OPTO*. 2014. International Society for Optics and Photonics.
[51]. Y. Peter and M. Cardona, "Fundamentals of semiconductors: physics and materials properties". 2010: Springer Science & Business Media.
[52]. J. Liu. "Monolithically integrated Ge-on-Si active photonics". in *Photonics*. 2014. Multidisciplinary Digital Publishing Institute.
[53]. C.-Y. Tsai, et al., "Theoretical model for intravalley and intervalley free-carrier absorption in semiconductor lasers: Beyond the classical Drude model". *IEEE journal of quantum electronics*. 34(3): p. 552-559. 1998
[54]. W. Spitzer and J. Whelan, "Infrared absorption and electron effective mass in n-type gallium arsenide". *Physical Review*. 114(1): p. 59. 1959
[55]. A.-A. Kanoun and S. Goumri-Said. "Characterization of DGFET properties from multiscale modeling: Effects of oxide thickness and temperature". in *Dielectric Materials for Photovoltaic Systems (NAWDMPV), 2014 North African Workshop on*. 2014. IEEE.
[56]. S.M. Sze and K.K. Ng, "Physics of semiconductor devices". 2006: John wiley & sons.
[57]. "Crosslight Device Simulation Software-General Manual". *Available online at web page http://www. crosslight. ca*. 2015
[58]. W. Lochmann, "Phonon-assisted auger recombination in indirect gap semiconductors". *physica status solidi (a)*. 45(2): p. 423-432. 1978
[59]. I. Karpova, V. Perel, and S. Syrovegin, "Auger recombination in heavily doped germanium". *Soviet Physics Semiconductors-Ussr*. 23(5): p. 518-521. 1989
[60]. D. Steiauf, E. Kioupakis, and C.G. Van De Walle, "Auger recombination in GaAs from first principles". *Acs Photonics*. 1(8): p. 643-646. 2014
[61]. C. Haas, "Infrared absorption in heavily doped n-type germanium". *Physical Review*. 125(6): p. 1965. 1962
[62]. M. Oehme, et al., "Direct bandgap narrowing in Ge LED's on Si substrates". *Optics express*. 21(2): p. 2206-2211. 2013
[63]. S. Jain and D. Roulston, "A simple expression for band gap narrowing (BGN) in heavily doped Si, Ge, GaAs and GexSi1− x strained layers". *Solid-State Electronics*. 34(5): p. 453-465. 1991
[64]. R. Camacho-Aguilera, et al., "Direct band gap narrowing in highly doped Ge". *Applied Physics Letters*. 102(15): p. 152106. 2013
[65]. R. Sun, "Advanced materials, process, and designs for silicon photonic integration", Massachusetts Institute of Technology. 2009

[66]. X. Sun, et al., "Direct gap photoluminescence of n-type tensile-strained Ge-on-Si". *Applied Physics Letters*. 95(1): p. 011911. 2009
[67]. J. Liu, et al., "Deformation potential constants of biaxially tensile stressed Ge epitaxial films on Si (100)". *Physical Review B*. 70(15): p. 155309. 2004
[68]. W.W. Chow, "Model for direct-transition gain in a Ge-on-Si laser". *Applied Physics Letters*. 100(19): p. 191113. 2012
[69]. D.J. Paul, "Si/SiGe heterostructures: from material and physics to devices and circuits". *Semiconductor Science and Technology*. 19(10): p. R75. 2004
[70]. K. Brunner, "Si/ge nanostructures". *Reports on Progress in Physics*. 65(1): p. 27. 2001
[71]. D. Nam, et al., "Electroluminescence from strained germanium membranes and implications for an efficient Si-compatible laser". *Applied Physics Letters*. 100(13): p. 131112. 2012
[72]. Y.-H. Kuo, et al., "Strong quantum-confined Stark effect in germanium quantum-well structures on silicon". *Nature*. 437(7063): p. 1334-1336. 2005
[73]. F. Cai, et al., "Enhanced Si–Ge interdiffusion in high phosphorus-doped germanium on silicon". *Semiconductor Science and Technology*. 30(10): p. 105008. 2015
[74]. F. Cai, "Study of Si-Ge interdiffusion with highly n-type doping", University of British Columbia. 2016
[75]. M.I. Azawe, "Temperature dependence of wall-plug efficiency of high power laser diodes". *International Journal of Physical Sciences*. 8(10): p. 362-370. 2013
[76]. D.S. Sukhdeo, et al., "Impact of minority carrier lifetime on the performance of strained germanium light sources". *Optics Communications*. 364: p. 233-237. 2016
[77]. R. Geiger, et al., "Excess carrier lifetimes in Ge layers on Si". *Applied Physics Letters*. 104(6): p. 062106. 2014
[78]. D. Nam, et al., "Observation of improved minority carrier lifetimes in high-quality Ge-on-insulator using time-resolved photoluminescence". *Optics letters*. 39(21): p. 6205-6208. 2014
[79]. R. Newman and W. Tyler, "Effect of impurities on free-hole infrared absorption in p-type germanium". *Physical Review*. 105(3): p. 885. 1957
[80]. D. Schroder, R.N. Thomas, and J.C. Swartz, "Free carrier absorption in silicon". *IEEE Journal of solid-state circuits*. 13(1): p. 180-187. 1978
[81]. O. Ogah, "Free-carrier effects in polycrystalline silicon-on-insulator photonic devices", in Rochester Institute of Technology. 2010
[82]. K. Luke, et al., "Broadband mid-infrared frequency comb generation in a Si 3 N 4 microresonator". *Optics letters*. 40(21): p. 4823-4826. 2015
[83]. L. Buchaillot, et al., "Silicon nitride thin films Young's modulus determination by an optical non destructive method". *Japanese journal of applied physics*. 36(6B): p. L794. 1997
[84]. D. Peschka, et al., "Robustness analysis of a device concept for edge-emitting lasers based on strained germanium". *Optical and Quantum Electronics*. 48(2): p. 1-7. 2016